THE HONG KONG
POLYTECHNIC UNIVERSITY
香港理工大學
Pao Yue-kong Library
包玉剛圖書館

Copyright Undertaking

This thesis is protected by copyright, with all rights reserved.

By reading and using the thesis, the reader understands and agrees to the following terms:

1. The reader will abide by the rules and legal ordinances governing copyright regarding the use of the thesis.
2. The reader will use the thesis for the purpose of research or private study only and not for distribution or further reproduction or any other purpose.
3. The reader agrees to indemnify and hold the University harmless from and against any loss, damage, cost, liability or expenses arising from copyright infringement or unauthorized usage.

If you have reasons to believe that any materials in this thesis are deemed not suitable to be distributed in this form, or a copyright owner having difficulty with the material being included in our database, please contact lbsys@polyu.edu.hk providing details. The Library will look into your claim and consider taking remedial action upon receipt of the written requests.

Pao Yue-kong Library, The Hong Kong Polytechnic University, Hung Hom, Kowloon, Hong Kong

http://www.lib.polyu.edu.hk

The Hong Kong Polytechnic University
Department of Applied Physics

Synthesis and characterization of wide bandgap cubic ZnO

Lau Chun Hei

A thesis submitted in partial fulfillment of the requirements for the Degree of Master of Philosophy

July 2007

Pao Yue-kong Library
PolyU · Hong Kong

CERTIFICATE OF ORIGINALITY

I hereby declare that this thesis is my own work and that, to the best of my knowledge and belief, it reproduces no material previously published or written nor material which has been accepted for the award of any other degree or diploma, except where due acknowledgement has been made in the text

_____(Signed)

_____Lau Chun Hei_____(Name of student)

Abstract

Crystalline magnesium zinc oxide (MZO) thin films of about 300 nm to 500 nm thick were fabricated on MgO (0 0 1) and LAO (0 0 1) substrates by pulsed laser deposition method. The MZO ablation target has a nominal composition of $Mg_{0.5}Zn_{0.5}O$. It has been revealed that the Zn content in the deposited films is substantially less than that of the target and it varies according to the growth conditions. X-ray diffraction and transmission electron microscopic studies show that a single cubic phase MZO (c-MZO) is obtained in films grown on these two types of substrates at deposition temperatures between 300˚C and 600˚C. The x-ray 360˚ phi-scan results suggest excellent epitaxial relation between the films and the substrates. The phenomenon of 45˚ in-plane twisted growth of c-MZO film on LAO is observed. This is attributed to the result of maximized lattice matching. Films grown on MgO substrates, however, show the typical cube-on-cube epitaxy. Indium doped c-MZO films exhibit n-type semiconduction. The electrical conduction in these films is attributed to the free electrons generation via the indium (In) dopant, and therefore is highly sensitive to the indium content. Epitaxial c-MZO films with resistivity of 5.5×10^{-2} Ωcm were obtained when doped with more than 20 at. % of indium.

All indium doped c-MZO (c-MZO:In) films have an optical transmittance of over 80 % for the whole visible spectrum. It has been revealed that the c-MZO band gap energy is roughly equal to 4eV and can be tuned by simply changing the indium concentration. Therefore these epitaxial films can be used as variable UV filters and transparent conducting oxide (TCO) for various optoelectronics applications.

In the present study we have also fabricated all-oxides p-n junctions. They are formed by depositing n-type indium doped c-MZO and p-type LiNiO (LNO) films in succession on the lattice matched substrates. Both the c-MZO:In and LNO have similar cubic structures and can be grown epitaxially on MgO or LAO substrates. I-V rectifying characteristics at room temperature were evaluated. Excellent rectifying properties have been demonstrated. Temperature dependence studies suggested non-ideal p-n junction characteristics. Both the c-MZO and LNO are optically transparent, and we have therefore produced a transparent all-oxide cubic p-n junction, which is believed to be very useful for future oxide electronics and spintronics.

For device applications, the potential of integrating these p-n junctions onto Si substrates are of prime importance. In the present work we have grown indium doped c-MZO on silicon with TiN buffer layer. The TiN layer, apart from assisting the epitaxial growth of the oxide heterostructures, also serves as a high conduction electrical lead for the p-n junction. Excellent current rectifying characteristics have been demonstrated. Our results thus provide strong experimental support for developing a workable all-oxide integrated p-n junction.

ACKNOWLEDGEMENTS

I would like to give my kindest thankfulness to a number of people who help me a lot during the past two years. First of all, I am indebted to my supervisor, Dr. K. H. Wong for his guidance and supervision throughout the years. His opinion is always beneficial to me at the time I am confused in the research and the experimental results are not that promising. I also wish to thank Dr. K. H. Pang and Dr. C. W. Tai for their valuable advices on TEM characterization. Thanks must go to Mr. M. N. Yeung, Mr. C. S. Lo, Mr. K. S. Wong and Ms. Y. Yeung for their assistance of the experimental measurements. I thank my colleagues, K. C. Chan, W. L. Sin, L. Zhuang, C. Y. Lam, M. H. Wong and W. F. Cheng, for their helpful suggestions, which are enormously invaluable to my research progress as well as my life in general.

Finally, my family members give their unreserved support during my graduate studies. I would like to express my utmost gratitude to them.

LIST OF CONTENTS

Abstract i

ACKNOWLEDGEMENTS iii

LIST OF FIGURES viii

LIST OF TABLES xii

Chapter 1 1

Introduction 1

1.1 Backgrounds of oxide thin films 1
1.2 Zinc oxide 2
1.3 Literature review 6
1.4 Thesis outline 9

Chapter 2 11

Pulsed Laser Deposition 11

2.1 Introduction 11
2.2 Thin film growth modes 13
2.3 Epitaxial growth 15
2.4 Deposition conditions 17
2.4.1 Substrate temperature 17
2.4.2 Background gases 18
2.4.3 Laser fluence 18
2.5 PLD Setup 19
2.6 Advantages and disadvantages of PLD 21

Chapter 3 23

Characterization methods 23

3.1 Introduction 23
3.2 Structural measurements 24
3.2.1 X-ray diffractometry (XRD) 24
3.2.2 Transmission electron microscopy (TEM) 28
3.3 Surface morphology 31
3.3.1 Atomic force microscopy (AFM) 31
3.3.2 Scanning electron microscopy (SEM) 32
3.4 electrical measurements 34
3.4.1 Temperature dependent resistivity 34
3.4.2 Current against voltage measurement 35
3.4.3 Hall measurement 35
3.5 Optical measurement 38
3.5.1 Transmittance measurement 38
3.6 Composition analysis 40
3.6.1 SEM energy dispersive x-ray (EDX) 40
3.6.2 X-ray Photoelectron Spectroscopy (XPS) 40

Chapter 4 42

Fabrication and characterization of In-doped c-MZO thin films on LAO and MgO substrates 42

4.1 Introduction 42
4.2 Fabrication and characterization of In doped- c-MZO target 44
4.2.1 Fabrication of In doped- c-MZO targets 44
4.2.2 Structural characterization of In-doped c-MZO targets 44
4.2.3 Composition analysis of In-doped c-MZO targets 46
4.2.4 Deposition of In doped c-MZO thin films on MgO and LAO substrates 47
4.2.5 Composition variation of In-doped c-MZO thin films 52
4.3 Characterization of In-doped c-MZO thin films against doping concentration 54
4.3.1 Phase characterizations 54
4.3.2 Surface morphologies 56
4.3.3 Electrical characterizations 59
4.3.4 Optical characterizations 65

4.4 Phase characterization of In-doped c-MZO thin films against substrate temperatures 69
4.4.1 Phase characterization 69
4.4.2 Surface morphologies 73
4.4.3 Electrical characterizations 74
4.4.4 Optical characterizations 75
4.5 Optimal deposition condition of c-MZO:In thin films 78

Chapter 5 79

Fabrication and characterization of indium doped c-MZO/LNO p-n heterojunction on LAO and MgO substrates 79

5.1 Introduction of all oxide p-n junction 79
5.1.1 The working mechanism of all-oxide p-n junction 80
5.2 Structural measurements of c-MZO:In/LNO p-n heterojunction 84
5.2.1 Structural characterization of LNO target 84
5.2.2 Deposition of LNO thin films on MgO substrate 85
5.2.3 Structural characterization of LNO thin films 86
5.2.4 Structural characterization of c-MZO:In/LNO bi-layer structure 88
5.3 Electrical measurement of c-MZO:In/LNO p-n heterojunction 94
5.3.1 Current-voltage characteristic 94
5.3.2 Temperature dependence current-voltage characteristic 100
5.4 Optical measurements of c-MZO:In/LNO p-n heterojunction 108

Chapter 6 110

Fabrication and characterization of c-MZO:In/LNO on TiN buffered Si substrate 110

6.1 Introduction of TiN thin film 110
6.2 Deposition of TiN on Si substrate 112
6.2.1 TiN target analysis 112

6.2.2 Deposition of TiN, c-MZO:In and LNO layers..... 113
6.3 Structural measurements of c-MZO:In/LNO on TiN buffered Si substrate.... 115
6.3.1. Structural characterization of TiN on Si 115
6.3.2 Structural characterization of c-MZO:In/LNO on TiN buffered Si substrate 116
6.4 Electrical measurements of c-MZO:In/LNO on TiN buffered Si substrate 120
6.4.1 Current-voltage characteristic 120
6.4.2 Comparison of c-MZO:In/LNO junction on MgO and Si substrates... 121

Chapter 7..... 126

Conclusion 126

References..... 131

LIST OF FIGURES

Figure1.1 The hexagonal structure of ZnO 3
Figure 1.2 The rocksalt structure of MgO 4
Figure 1.3 The phase diagram of MgZnO system (from Bendersky et al[1-8]). 5
Figure 1.4 The band gap energy of MgZnO system against Mg content (from Yang et. al. [1-9]). 5
Figure 1.5 The composition of MgZnO thin film by using $Mg_{0.4}Zn_{0.6}O$ target against substrate temperature (from Yang et. al. [1-9]). 8
Figure 2.1 Schematic diagram of the PLD ablation 12
Figure 2.2 Schematic diagram of three growth modes: (a) Volmer-Weber (b) Frank-van der Merwe and (c) Stranski-Krastinov. 14
Figure 2.3 Schematic diagram of PLD setup 20
Figure 3.1 Schematic diagram of Bragg's reflection 26
Figure 3.2 Schematic diagram of omega scan. 27
Figure 3.3 Schematic diagram of 360˚ phi-scan. 28
Figure 3.4 The electron diffraction pattern of (a) single crystal and (b) polycrystalline material 30
Figure 3.5 Schematic diagram of atomic force microscopy (AFM) setup 31
Figure 3.6 Schematic diagram of resistivity measurement 35
Figure 3.7 Schematic diagram of Hall Effect measurement 37
Figure 4.1 XRD powder diffraction of $Mg_{0.5}Zn_{0.5}O$ target 45
Figure 4.2 XRD powder diffraction of c-MZO targets with different indium content ... 45
Figure 4.3 XRD θ-2θ scan of c-MZO film on LAO (0 0 1) substrate 49
Figure 4.4 XRD 360˚ phi-scans of c-MZO film on LAO (0 0 1) substrate 49
Figure 4.5 XRD θ-2θ scan of 4 at. % c-MZO:In thin film on MgO (0 0 1) substrate 50
Figure 4.6 XRD 360˚ phi-scans of c-MZO thin film on MgO (0 0 1) substrate 50
Figure 4.7 SEM cross section image of c-MZO:In on MgO (0 0 1)substrate 51
Figure 4.8 TEM electron diffraction pattern of c-MZO:In thin film (point a) on (b) MgO (0 0 1) substrate (point b) 51
Figure 4.9 The relative compositions of 18 at. % c-MZO:In film deposited at 300˚C ... 53
Figure 4.10 XRD θ-2θ scans of c-MZO thin films against indium content. 55
Figure 4.11 Lattice constants of c-MZO thin films against indium content. 55
Figure 4.12 XRD ω scans of c-MZO (0 0 2) diffraction plane with different indium

content 56
Figure 4.13 SEM images of (a) pure c-MZO, (b)4, (c)8, (d)16, (e)18 at. % indium doped c-MZO thin film surface. 58
Figure 4.14 AFM image of 18 at % c-MZO:In thin film. 59
Figure 4.15 The comparison of $R \propto T^{-1/8}$ equation and the experimental result. 63
Figure 4.16 The Ln-plot of resistance against (a) $T^{-1/2}$, (b)$T^{-1/4}$, (c)$T^{-1/6}$, (d)$T^{-1/8}$ 63
Figure 4.17. The Ln-plot of conductivity against 1/Temperature. 64
Figure 4.18 Resistivity of c-MZO aginst indium content 64
Figure 4.19 Carrier concentration of c-MZO against indium content 65
Figure 4.20 Transmittance profiles of c-MZO against indium content 67
Figure 4.21 The plots of $(\alpha h\nu)^2$ against photon energy with different indium content ... 67
Figure 4.22 The refractive index of c-MZO:In by prism-coupling technique. 68
Figure 4.23 XRD θ-2θ scans of 16 at.% c-MZO:In against substrate temperature 71
Figure 4.24 Lattice constants of 16 at % c-MZO:In against substrate temperature 71
Figure 4.25 XRD ω scan of 16 at % c-MZO:In (0 0 2) diffraction plane against substrate temperature 72
Figure 4.26 XRD θ-2θ scans of pure c-MZO against substrate temperature 72
Figure 4.27 XRD ω scan of pure c-MZO (0 0 2) diffraction plane against substrate temperature 73
Figure 4.28 The SEM images of 18 at. % c-MZO:In at substrate temperatures (a)300˚C, (b)500˚C, (c)600˚C, (d)700˚C. 74
Figure 4.29 Resistivity of 16 at. % c-MZO:In films against substrate temperature. 75
Figure 4.30 Transmittance profiles of 16 at. % c-MZO:In film against substrate temperature 77
Figure 4.31 The plot of $(\alpha h\nu)^2$ against photon energy of 16 at. % c-MZO:In film with different substrate temperature 77
Figure 5.1 Energy band diagrams of a p-n junction (a) before, (b) after merging the n-type and p-type regions and (c) in thermal equilibrium 82
Figure 5.2 Energy band diagrams of a p-n junction under (a) forward biased and (b) reversed biased. 83
Figure 5.3 XRD powder diffraction of LNO target 85
Figure 5.4 XRD θ-2θ scan of LNO thin film on MgO (0 0 1) substrate. 86
Figure 5.5 XRD ω scan of LNO (0 0 2) diffraction plane on MgO (0 0 1) substrate 87
Figure 5.6 XRD 360˚ phi-scans of LNO on MgO (0 0 1) substrate 87
Figure 5.7 The schematic structure of c-MZO:In/LNO heterojunction on LAO/MgO

substrate. 90
Figure 5.8 XRD θ-2θ scan of c-MZO:In/LNO heterojunction on LAO (0 0 1) substrate 90
Figure 5.9 XRD ω scans of c-MZO:In/LNO (0 0 2) diffraction planes heterojunction on LAO (0 0 1) substrate 91
Figure 5.10 XRD 360˚ phi-scans of c-MZO:In/LNO heterojunction on LAO (0 0 1) substrate 91
Figure 5.11 XRD θ-2θ scan of c-MZO:In/LNO heterojunction on MgO (0 0 1) substrate 92
Figure 5.12 XRD ω scans of c-MZO:In/LNO (0 0 2) diffraction planes heterojunction on MgO (0 0 1) substrate 92
Figure 5.13 360˚ phi-scans of c-MZO:In/LNO heterojunction on MgO (0 0 1) substrate 93
Figure 5.14 Ohmic contacts of (a) Pt on c-MZO:In, (b) Pt on LNO and (c) Au on c-MZO:In 95
Figure 5.15 The rectifying profiles of c-MZO:In/LNO heterojunction on MgO (0 0 1) substrate 96
Figure 5.16 The rectifying profiles of c-MZO:In/LNO heterojunction with 16 and 18 at. % indium (same scale) 97
Figure 5.17 The rectifying profiles of c-MZO:In/LNO heterojunction with 16 and 18 at. % indium (not in scale) 97
Figure 5.18 The ratios of forward to backward current of c-MZO:In/LNO heterojunction with 16 and 18 at. % indium 98
Figure 5.19 The rectifying profiles of c-MZO:In/LNO heterojunctions with different deposition conditions 99
Figure 5.20 The rectifying profiles of 18 at. % c-MZO:In/LNO heterojunction under different measuring temperature. 103
Figure 5.21 The rectifying profiles of 18 at. % c-MZO:In/LNO heterojunction series resistance elimination under different measuring temperature. 104
Figure 5.22 The turn-on voltages of 18 at. % c-MZO:In/LNO heterojunction under different measuring temperature. 104
Figure 5.23 The ln plot of rectifying profiles of 18 at. % c-MZO:In/LNO heterojunction under different measuring temperatures and Si non-ideal I-V curve (from Bart Van Zeghbroeck [5-20]). 105
Figure 5.24 Current-Voltage characteristics of a c-MZO:In/LNO p-n junction under

forward bias.....106
Figure 5.25 The slopes of the Ln(I) against voltage at different non-ideal characteristic. 107
Figure 5.26 Transmittance profiles of the c-MZO:In/LNO heterojunction with different deposition condition of LNO. 109
Figure 6.1 XRD powder diffraction of TiN target. 112
Figure 6.2 The schematic structure of c-MZO:In/LNO heterojunction on TiN buffered Si, the arrows are the flow of the electrons. 114
Figure 6.3 XRD θ-2θ scan of TiN on Si (0 0 1) substrate.....115
Figure 6.4 XRD ω scan of TiN (0 0 2) on Si (0 0 1) substrate 116
Figure 6.5 XRD θ-2θ scan of c-MZO:In/LNO heterojunction on TiN buffered Si (0 0 1) substrate. 117
Figure 6.6 XRD ω scans of c-MZO:In/LNO (0 0 2) diffraction planes heterojunction on TiN buffered Si.....118
Figure 6.7 XRD 360˚ phi-scans of c-MZO:In/LNO heterojunction on TiN buffered Si. 119
Figure 6.8 The rectifying profile of c-MZO:In/LNO heterojunction on TiN buffered Si 121
Figure 6.9 Comparison of c-MZO:In/LNO heterojunction on TiN buffered Si and MgO substrates (same scale) 123
Figure 6.10 Comparison of c-MZO:In/LNO heterojunction on TiN buffered Si and MgO substrates (not in scale).....123
Figure 6.11 Comparison of c-MZO:In/LNO heterojunction on TiN buffered Si and MgO substrates without series resistance. 124
Figure 6.12 The ratios of forward to backward current of c-MZO:In/LNO heterojunction on TiN buffered Si and MgO substrates 125

LIST OF TABLES

Table 4.1 The composition variation of the c-MZO targets 46
Table 4.2 Composition variation of c-MZO:In from sintered target to deposited film... 53
Table 5.1 The values of the ideality factors at different regions against sample temperature..... 107

Chapter 1

Introduction

1.1 Backgrounds of oxide thin films

Oxides have a wide range of properties such as ferromagnetism [1-1], superconduction [1-2], wide band-gap semiconduction [1-3], and high k dielectric [1-4] etc. They are therefore the preferred choice of materials for fabricating future advanced electronic devices with new functionalities. Their potential applications in solar cell, light emitting diode (LED), blue light laser, flash memory, spintronics, etc. have been predicted. In micro and optoelectronic devices, oxide thin films of sub-micrometer thick are being used. Large amount of effort in recent years has been devoted to synthesizing and characterizing of oxide ceramics thin film. The results achieved so far are both valuable and encouraging. Indeed, all-oxide p-n junctions with good diode characteristics have been demonstrated in the recent years.

1.2 Zinc oxide

Zinc oxide (ZnO) is a well-known wide band gap semi-conducting ceramics that shows good optical transparency. It has a stable wurtzite (hexagonal) structure as shown in Fig. 1.1. The lattice constants of the a-axis and c-axis are 3.242Å and 5.176 Å respectively. It is a very stable material even at high temperature close to its melting point of 1975˚C. Indeed such high melting temperature and stability make ZnO a suitable material for high temperature processing and device fabrication. In addition to having a direct band gap energy of around 3.27 eV [1-5] at room temperature, ZnO is an attractive UV photonic material due to its unusually high excitonic energy of about 60meV [1-5] as compared with only 28 meV for GaN. Such large excitonic energy can greatly improve the efficiency of ZnO based photonic devices operated at room temperature.

Intrinsic ZnO has n-type conduction, which originates from oxygen vacancies in the crystalline structure. By appropriate impurity ions doping, the electrical conductivity of ZnO can be increased dramatically [1-6]. This improvement of conductivity can thus lead to a good transparent conducting oxide (TCO). In fact there has been a wide range of applications of ZnO thin films in industries already. Devices such as ultra-violet (UV) detector, solar cells, blue light emitting diode (LED), diode laser, transparent electrode etc. have all been reported [1-5]. More recently, magnetic metal ions doped in ZnO based materials, such as (Mn, Zn)O, have shown to be good dilute magnetic semiconductors (DMS). They could be excellent material systems for future spintronics [1-7].

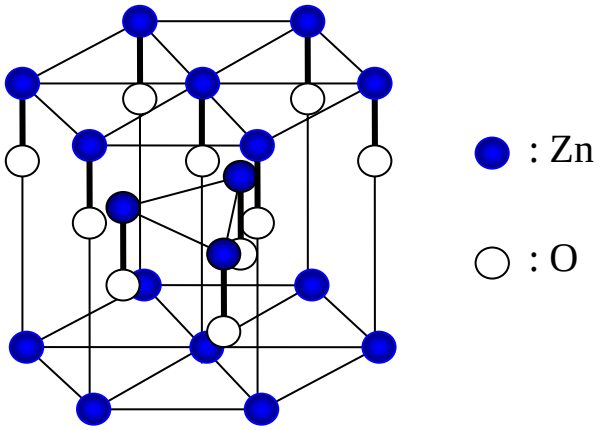

Figure1.1 The hexagonal structure of ZnO

ZnO has a stable wurtzite structure at equilibrium condition. It changes to cubic phase under high pressure of ~100kbar. By alloying ZnO with lattice matched cubic monoxides and depositing it on structurally compatible cubic substrates, we believe this high pressure phase ZnO can be trapped and stabilized in thin film form even under normal ambient. Magnesium oxide (MgO) possesses a rocksalt structure (Fig. 1.2). When it is introduced in ZnO at an amount up to 33 at.%, according to the phase diagram of MZO system (Fig. 1.3), ZnO starts to dissolve in the MgO matrix. Under such circumstances, mixed phases of cubic MgZnO (c-MZO) and hexagonal (h-MZO) coexist [1-8]. Fig. 1.4 shows the band gap energy and phase transformation of MZO as a function of composition. For wurtzite structures the band gap energy gradually increases from 3.3eV of pure ZnO to a maximum value of 4.3eV of h-MZO. The band gap energy of c-MZO is about 5.4~7.8eV corresponding to a Mg concentration from 62 to 100 at.% [1-9]. The band gap relationship in $Mg_xZn_{1-x}O$ alloy for x varying from 0 to 0.82 can be concluded as the followings [1-10].

$Eg\ (Mg_xZn_{1-x}O) = 3.32 + 2.00x$ (For hexagonal-phase, $0 \leq x \leq 0.33$),

$Eg\ (Mg_xZn_{1-x}O) = 3.02 + 4.03x$ (For cubic-phase, $0.45 \leq x \leq 0.82$)

Mg^{2+}(0.78 Å) has an ionic radius similar to that of Zn^{2+}(0.83 Å). Rocksalt structured MgO has a lattice constant of 4.2Å. This is very close to that of cubic ZnO of 4.28 Å. Apart from the dopant effect, depositing MZO thin films on cubic MgO (0 0 1) and $LaAlO_3$ (LAO) substrates can also help to stabilize the c-MZO phase because of the epitaxial growth due to good lattice matching.

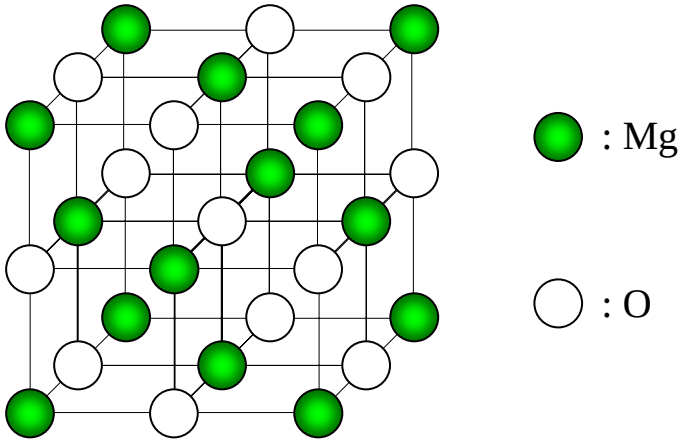

Figure 1.2 The rocksalt structure of MgO

If MZO is to be developed into useful photonic materials, c-MZO phase provides many advantages. Firstly, if cleaved along the parallel set of crystal planes, c-MZO allows easy formation of a natural optical resonator for laser. This is in fact a conventional technique used in fabricating red and IR diode lasers based on cubic GaAs. In hexagonal structured semi-conducting material laser, such as GaN, chemical or mechanical etching is needed to form the required laser resonator. For this reason the production yield is low and the process is expensive [1-11], [1-12]. Secondly, the lattice constant of c-MZO is around 4.2 Å, which is structurally compatible to many oxides, such as perovskites and transition metal monoxides. This increases the chance of growing epitaxial ZnO thin films on other oxides. Thirdly, the anisotropic properties of

hexagonal ZnO can be reduced. Anisotropic mechanical and piezoelectric properties of ZnO may not often be advantageous according to the purpose of the applications.

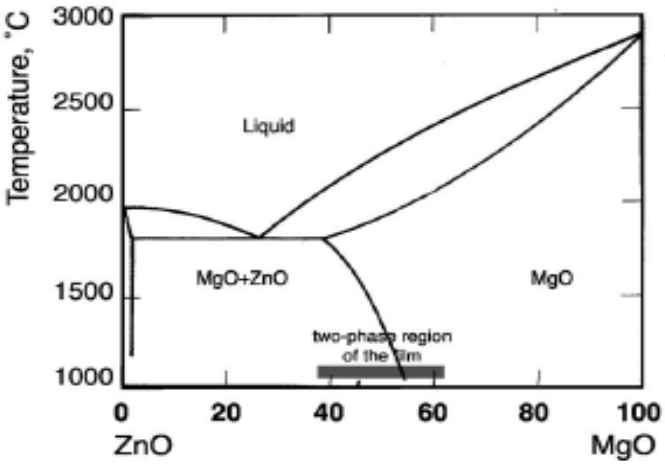

Figure 1.3 The phase diagram of MgZnO system (from Bendersky et al[1-8]).

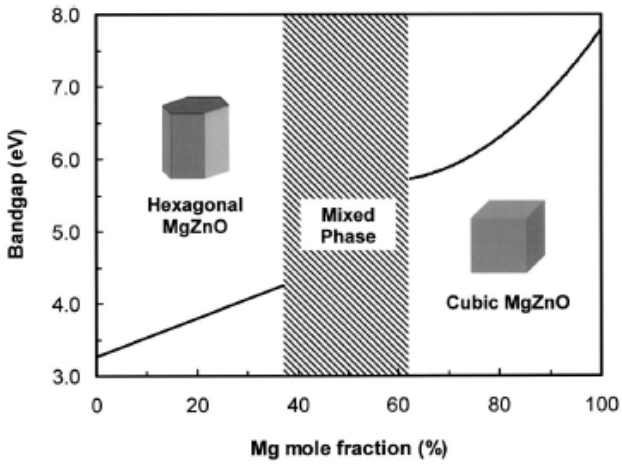

Figure 1.4 The band gap energy of MgZnO system against Mg content (from Yang et. al. [1-9]).

1.3 Literature review

ZnO thin film of hexagonal (wurtzite) structure was first fabricated by CO_2 laser ablation of ZnO powder target in 1983 [Sankur and Cheung, 1983[1-13]]. Highly oriented (0002) crystalline films with smooth surface and good optical transparency were obtained. Apart from PLD technique, other film deposition methods, such as chemical vapor deposition (CVD) [1-14], magnetron sputtering [1-15], sol-gel [1-16], plasma-assisted molecular beam epitaxy [1-17] etc., for growing ZnO thin films have also been reported. The versatile properties of ZnO with various dopants have been demonstrated. These include piezoelectricity at room temperature for surface acoustic wave devices [Sankur and Cheung, 1983], ferroelectricity with lithium doping [1-18], dilute magnetic semiconductor (DMS) with transition-metal doping, ferromagnetism [1-1] and high dielectric constant thin films [1-19], and transparent conducting ZnO doped with group III elements [1-6]. The wide range of potential applications has made the fabrication and characterization of ZnO a popular topic of research for many years.

In the pursuit of growing ZnO thin films, A. Ohtomo et al. proposed to prepare $Mg_xZn_{1-x}O$ alloy films by PLD in 1998 [1-20]. They found that single phase of hexagonal MgZnO existed with Mg content up to 33 at. %. The band gap energy as well as the photoluminescence peak changes from 3.3eV to 3.87eV with increasing Mg doping. When the Mg content is raised to beyond 33 at.%, MgO impurity phase segregated from the wurtzite structure. In 2001, cubic phase magnesium zinc oxide (c-MZO) was first demonstrated by J. Narayan et al. $Zn_{0.18}Mg_{0.82}O$ was successfully fabricated on TiN buffered Si by pulsed laser deposition [1-21]. The structural and

optical properties were studied. The lattice constant of c-MZO was found to be about 4.23Å. The TiN (lattice constant = 4.24 Å and can be heteroepitaxially grown on Si via domain matching) buffer layer helped to reduce the lattice mismatch between c-MZO and Si (lattice constant = 5.43 Å). The band gap energy of c-MZO was determined by the concentration of the Mg. Optical transmittance over 80% was observed for all their c-MZO films. The excitonic binding energy decreased to approximately 50meV for Mg content at 17 at. % and increased to 58meV when the content was up to 29 at. % [1-10]

In hexagonal intrinsic ZnO, the electrical resistivity varies from $10^{-3}\Omega$cm to several Ωcm depending on the oxygen content and crystallinity [1-22]. On the other hand, the electrical conduction of n-type ZnO can be substantially increased when doped with group III elements (e.g. Al, Ga, In etc.[1-23]). A resistivity of $10^{-4}\Omega$cm can be easily obtained with only a few at.% of dopant. Also p-type ZnO has been demonstrated by group V element (e.g. N, P etc. [1-24], [1-25], and [1-26]) doping. Up to date transparent conducting films of ZnO have been well studied and ZnO based p-n diode junctions have been exploited.

In the present research, we aim to fabricate c-MZO thin films with high ZnO content of above 40 at. %. Their structural and optical behaviors such as crystalline phase control, band gap engineering via doping, and temperature-dependence band gap energy [1-27], [1-28], [1-29], [1-19], and [1-30] are examined. Furthermore, the electrical property of c-MZO is being investigated. This is the first report on electrical conducting characteristics of c-MZO with high ZnO content.

The relationship between the substrate temperature and the composition of the films was investigated by S. Choopun in 2001[1-28] and W. Yang in 2003[1-9]. Their results revealed the loss of Zn content under high deposition temperature and low pressure (Fig. 1.5) is substantial. This phenomenon is primarily due to the fact that the vapor pressure of ZnO and Zn is much larger than MgO and Mg. Therefore, at such deposition condition, zinc preferentially desorbs and evaporates from the film surface, increasing the Mg/Zn ratio as a consequence. Interestingly, this feature can also be used to control the band gap energy of the film as it is Mg/Zn ratio dependent.

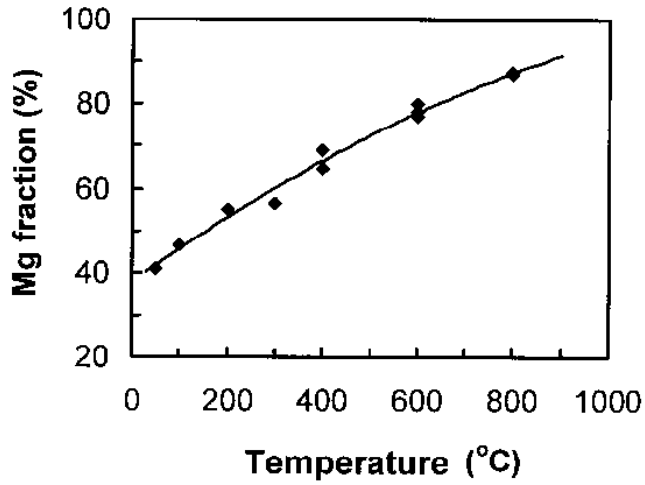

Figure 1.5 The composition of MgZnO thin film by using $Mg_{0.4}Zn_{0.6}O$ target against substrate temperature (from Yang et. al. [1-9]).

1.4 Thesis outline

This thesis discusses the experimental studies of the fabrication and properties of the c-MZO thin films fabricated by pulsed laser deposition. The objectives of the research are: (1) to obtain optimal condition of depositing indium doped n-type c-MZO. This includes the investigation of the structural, electrical and optical properties of the as-grown c-MZO:In thin films as functions of the substrate temperature and the concentration of dopant, (2) to fabricate all-oxide p-n junction with n-type conducting c-MZO. The properties of such a diode junction are evaluated and their potential applications are discussed.

In Chapter 2, the preparation of the c-MZO ablation targets via standard solid state reaction from their constituent oxides is explained. The fundamental processes and experimental setup of the PLD technique are described. How the substrate temperature, base pressure and laser fluent affect the quality of the film are evaluated. The advantages and disadvantages of PLD for growing epitaxial complex oxide thin films are also presented.

Chapter 3 introduces the thin film characterization techniques used in this research. Equipment such as x-ray diffractometer (XRD) and transmission electron microscope (TEM) for structural measurements, atomic force microscope (AFM) and scanning electron microscope (SEM) for surface morphology characterization are described. The measurements of current-voltage characteristics of the p-n junctions are presented. We have also established that the c-MZO films and heterostructures have very good optical

transparency by transmittance spectroscopic studies.

The fabrication and characterization of In doped c-MZO thin films are reported in Chapter 4. The relationships between the properties of the films and the substrate temperature are evaluated. The effects of dopant content are also discussed. The optimal deposition condition for c-MZO:In films is identified and reported.

In chapter 5, we describe the fabrication of all-oxide p-n junctions of In doped c-MZO/LNO on MgO and LAO. The measurements of the diode current-voltage characteristic are presented. The temperature dependent properties of these junction diodes are examined. At the end of this chapter we also report the optical properties of the c-MZO:In/LNO heterostructures. Our results clearly confirm that the c-MZO:In/LNO fabricated in this work is a good optical transparent all-oxide p-n junction.

We further describe the integration of In doped c-MZO/LNO p-n junction on TiN buffered Si substrates in Chapter 6. The advantages of fabricating p-n junction on Si substrates are explained. We also compare the characteristics between p-n junctions grown on MgO and on Si substrates. Finally we have demonstrated the possibility of fabricating integrated all-oxide p-n junctions.

Conclusion of the present investigation and major findings are given in the last chapter. We have summarized our current achievement of PLD of In doped c-MZO thin films and suggested future studies related to possible applications of the c-MZO.

Chapter 2

Pulsed Laser Deposition

2.1 Introduction

Techniques of fabricating thin films can be categorized into three different classes: (1) physical methods, (2) chemical methods, and (3) hybrid (i.e. physical-chemical) methods. [John L.Vossen et al., 1978[2-1]]. Pulsed laser deposition is one kind of physical vapor deposition processes that provides a convenient way to grow virtually all kinds of materials thin films, irrespective of whether it is oxides, metals, polymers, or even biological materials [Robert Eason 2006[2-2]].

Pulsed laser deposition (PLD) has been used for preparing thin films since the early 1960s [Robert Eason 2006[2-2]]. However, it became a popular film growth technique only after the success of in-situ deposition of epitaxial high-temperature superconducting films in the late 1980s [2-3]. As it turned out, PLD provides researchers a rapid and easy route into advanced thin film research and application venues. The principle of PLD is relatively simple. A high energy UV laser pulse of about several nano-seconds duration generated from, typically, an excimer laser is focused by UV lens. The converging light penetrates through fused silica window of a vacuum chamber and focuses onto the ablation target. The on-target laser pulsed energy density is typically of a few J cm^{-2} for efficient ablation of ceramic targets. The photon

energy absorbed by the target surface rapidly converts to heat energy and super-heat up the target surface layer up to several thousands degrees Celsius. This exceedingly high thermal heating congruently melts and indiscriminatingly vaporizes the target surface materials. The small amounts of materials that emanate from the surface of the target form fast forward moving luminous plasma. The plasma contains the mixture of energetic species including atoms, molecules, electrons, ions, clusters, micro-sized solid particulates, and molten globules [2-4]. These ablated species rapidly expand and deposit on the substrate surface. The process is shown schematically in sequence in Fig. 2.1[2-2].

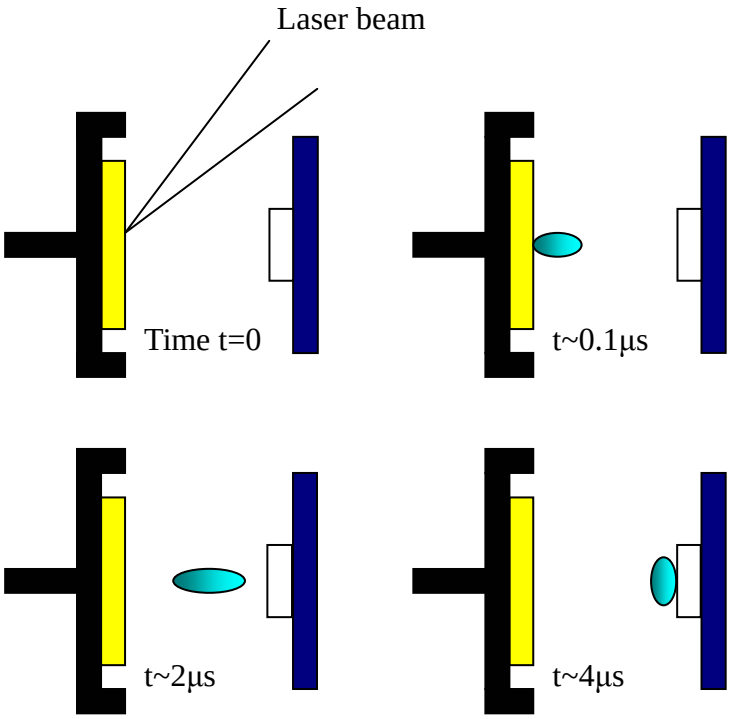

Figure 2.1 Schematic diagram of the PLD ablation

2.2 Thin film growth modes

Conventionally, the theories of thin film nucleation and growth can be classified into three categories for simplicity: (i) three-dimensional island growth (Volmer-Weber), (ii) two-dimensional full-monolayer growth (Frank-van der Merwe), and (iii) two-dimensional growth of full monolayer followed by nucleation and growth of three-dimensional islands (Stranski-Krastinov) (see in Fig. 2.2).

Three-dimensional island growth involves the nucleation of the condensates into small cluster directly on the substrate surface. When the ablated material erupts from the target and is collected by the substrate, the adatoms nucleate to form islands on the substrate surface. The existing islands grow with the forthcoming atoms until a continuous film appears. This growth mode always happens if the bonding between the adatoms is stronger than that between the adatoms and substrate, such as metal films on insulating or contaminated substrate. Clusters below the critical size dissolve and break apart whereas those larger than the critical size stabilize and grow in accordance with the heterogeneous three-dimensional nucleation theory.

Two-dimensional full-monolayer growth exists when the bonding strength between the atoms and the substrate is greater than that among adatoms themselves. The atoms tend to slide across the substrate surface instead of forming the nucleation islands. The mobility of adatoms along the film surface is very high. Therefore, continuous film grows layer by layer. This growth mode is always found in homoepitaxial growth like metal-metal or semiconductor-semiconductor deposition.

The last growth mode is a mixed mode of the first two. At the early stage of film growth, the layer formation is primarily the two-dimensional full-monolayer growth as the bonding of the adatoms and the substrate dominated. After several monolayers, however, the interaction of the ablating atoms and the substrate becomes weak. The adatoms are now preferred to grow with a three-dimensional island growth mode. Although the origin of the transition from two-dimensional to three-dimensional growth is not completely understood, the combined growth can be found in metal-metal and metal-semiconductor system.

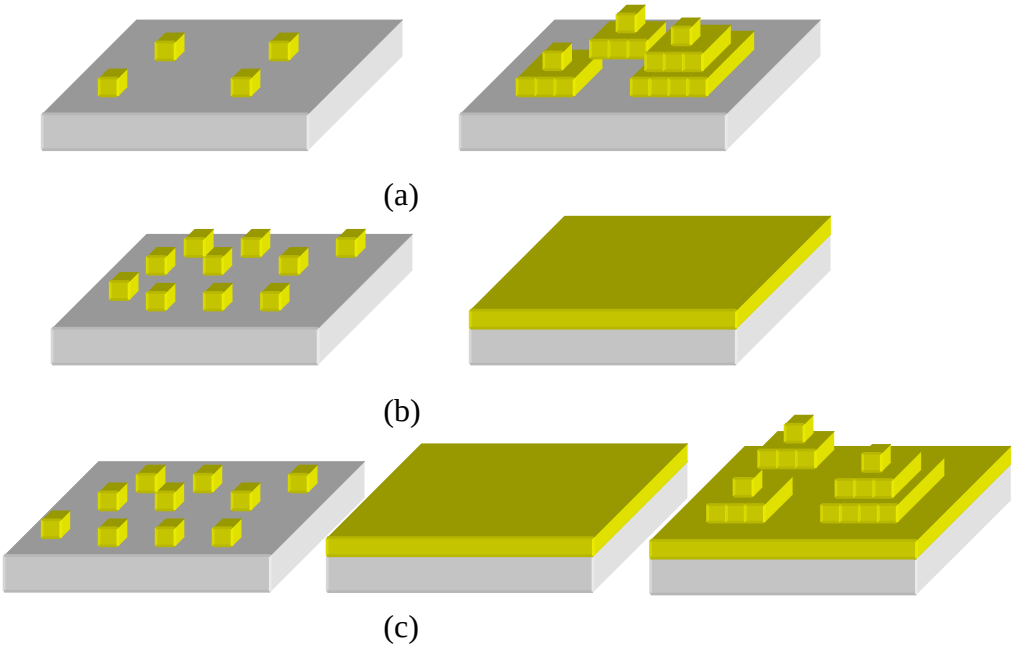

Figure 2.2 Schematic diagram of three growth modes: (a) Volmer-Weber (b) Frank-van der Merwe and (c) Stranski-Krastinov.

2.3 Epitaxial growth

When the film is grown with preferred orientation that aligned with the crystal structure of the substrate, it is called “epitaxy”. In Greek, the term “epi” means “above” and “taxis” means “in ordered manner”. A film is called epitaxial growth when its crystallographic order is being significantly influenced by that of the substrate as a result of some degree of matching and energy minimization between the two along the interface [2-5]. If the substrate has the same material composition as the film, the relationship is called homoepitaxy. If the two compositions are different, the growth is referred to as heteroepitaxy. In PLD, there are several factors that decisively influence the successfulness of epitaxial growth.

First of all, the substrate should have a preferred crystalline orientation which acts as a template for the thin film growth. For example, when the film is fabricated on a glass substrate, as the glass has an amorphous structure without any crystal orientation, there is no guided orientation for film deposition. Consequently, amorphous or polycrystalline layers with random grain orientation is obtained.

Apart from having similar crystal structure, the lattice constants of the film and the substrate should be as closely matched as possible. Lattice mismatch is a prim measurement of the dissimilarity between the film and the substrate. It is the ratio of the lattice constant difference of the film to that of the substrate. The lattice mismatch can be quantified as follow:

$$f = \frac{|a_s - a_f|}{a_s}$$

where a_s and a_f are the lattice constants of the substrate and the thin film respectively. In heteroepitaxy growth, a large lattice mismatch leads weak bonding at the interface. The induced strain is large. After several monolayers, the crystalline grains of the film will not grow along a unitary direction.

In PLD, when the film is deposited at room temperature, amorphous layer is always obtained with cracks, defects or dislocations. The existence of the defects often inhibits the epitaxial growth of thin film. Therefore, to fabricate polycrystalline thin film, the substrate should be kept at high temperature. At high temperature, the adatoms have sufficient thermal energy to be mobile enough to migrate freely to the suitable lattice site in order to attain the minimum potential energy.

The difference of thermal expansion of the interface layers may lead the failure of the epitaxial growth. The total strain in the film consists of intrinsic strain during growth, transformation strain, and strain induced by the mismatch from thermal expansion coefficient. Normally, the resultant stress is influenced by the thermal expansion, which can be described as

$$\sigma_{th} = \frac{E_f}{1-v_f}\varepsilon_{th} = \frac{E_f}{1-v_f}\int_{T_o}^{T}(\alpha_f - \alpha_s)dT$$

where E_f is the film Young's modulus, v_f is the Poisson ratio, α is the thermal expansion coefficient and T represents the temperature. Dislocation may appear when the thermal strain exceeds the elastic limit of the film.

2.4 Deposition conditions

In thin film growth, the deposition condition is crucial in governing the structural quality and the ultimate performance of the film. A more understanding of the effects of the fabrication parameters can always help. Parameters such as the substrate temperature, ambient vacuum condition and laser fluence need to be properly controlled in order to enhance our chance of obtaining good quality films.

2.4.1 Substrate temperature

Substrate temperature is very important in determining the film's microstructure and the surface morphology. It provides thermal energy for the adatoms to move around, causing excessive re-evaporation from the surface, and nucleation/crystallization in thin film growth. Moreover, when the mobility of the adatoms is high, continuous thin film is easily obtained on the substrate surface, giving a smooth surface with larger grain size.

Substrate temperature also preserves the stoichiometry in the deposited polycomponent films. As the speed of crystallization strongly depends on the substrate temperature, the temperature determines the heat loss of the condensate through the substrate. The higher the cooling rate of the condensate, the slower is crystallization speed. The mean adatom diffusion distance is very short, so only a few adatoms can form crystallites. At high substrate temperature, the cooling rate decreases and the condition exists for complete crystallization of all the adatoms. As a result the next vapor flux does not lead to re-evaporation of the previous deposited adatoms, which in this case are already included in the crystal structure [Douglas and Graham 1994][2-4].

2.4.2 Background gases

Laser ablation in some background gases causes composition and structural variation of the film. Under high laser energy, the irradiated surface of the solid state target changes to vapor phase and forms a luminous plasma plume. The ambient gases interact with the plasma, forming a different chemical composition on the substrate surface. A typical example is the formation of metal oxides from ablation of metal targets under ambient oxygen.

There are also some other drawbacks of PLD in the presence of background gases. One of them is the scattering problem. The high pressure increases the collision of all species. Consequently the plasma temperature rapidly decreases, causing the formation of particulates or unwanted reaction. Therefore, the film deposited under ambient gases always leads to rough surface containing certain amount of particulates. Another problem is the deposition yield and film uniformity. In a not so high ambient pressure (< 500 mTorr) the background gases prohibit the plasma to spread out laterally during their propagation from the target to the substrate. The thin film growth rate is higher than that at high vacuum condition, but the growth area is limited to a very smaller region (typical ~ 1 cm^2 in the forwarding direction). At higher ambient background gas pressure (> 500 mTorr), the ablated species are scattered and the film deposition rate diminishes.

2.4.3 Laser fluence

The on-target laser fluence (energy density) has the most significant effect on the particulate generation. The number of particulates increases with increasing fluence.

The average size of the particulate is large when the ablating energy density is high. Therefore, under high laser energy, particulates are always observed on the thin film. Thermal and kinetic energies of the plasma can significantly influence the crystalline growth of the film. At high laser fluence, the ablated particles carry high kinetic energy. When these energetic species are deposited, their kinetic energy is dissipated to the substrate. As a matter of facts, crystal growth is substantially enhanced at a relatively low substrate temperature

2.5 PLD Setup

Thin oxide films are fabricated by ablating the corresponding ceramic targets using KrF excimer laser of 248nm wavelength (Lambda Physik, COMPex 205). The experimental setup is shown schematically in Fig. 2.3. The experimental vacuum chamber is connected to the rotary-diffusion pump system, which can produce a base pressure of $2\sim7\times10^{-5}$ Torr depending the substrate temperature. The vacuum of the chamber is monitored by an ionization gauge (ULVAC 122A). The ablating target is mounted on a target holder, which is directly connected through a rotation axle to a d.c. motor. The “top-hat” spatial profiled pulsed laser is focused by the convex lens of 300mm focal length. The laser beam passes through the fused silica window of the vacuum chamber (transmittance is ~ 90%) and converges to a spot on the target surface. The incident angle of the beam is 45˚ relative to the normal of the target. The laser fluence is typically about 4 Jcm^{-2}. A bright plasma plume can be observed directly above the irradiated spot of the target. The substrate is placed at 4.5 cm away from the target.

To fabricated high quality crystalline films, the substrate has to be sustained at high temperature. Heating is provided by five halogen quartz lamps (50W output power per lamp) housed inside the substrate holder and thermally shielded in a cylindrical stainless steel case. The temperature is measured by a K type thermal couple (Nickel-Chromium, Nickel-Aluminum) embedded underneath the face plate of the substrate holder. The temperature can be controlled over the range between room temperature and 700˚C by a programmable regulator (PAC15-0321E). The substrate is adhered to the substrate holder surface by silver paste for good thermal contacts.

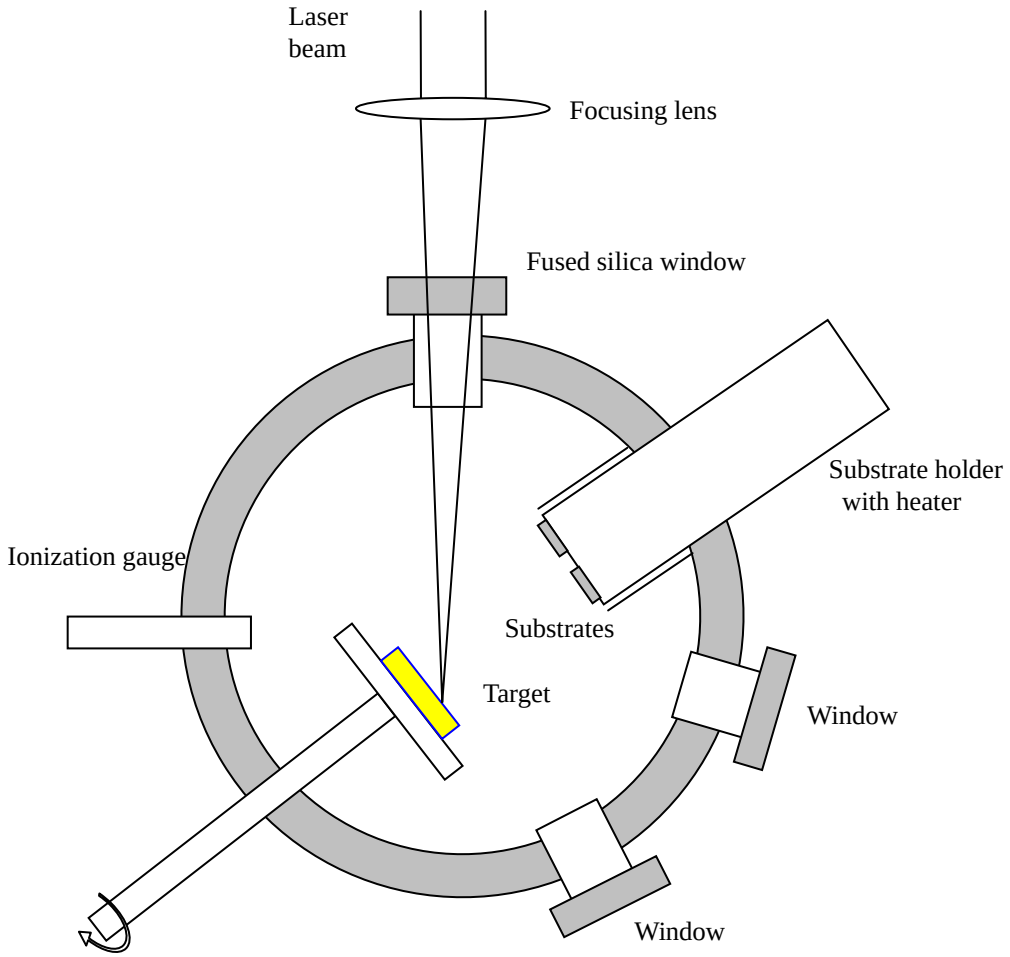

Figure 2.3 Schematic diagram of PLD setup

2.6 Advantages and disadvantages of PLD

There are many advantages associated with the PLD technique. They include the ability to retain the stoichiometry of a milticomponent target or spilt targets in the as-deposited thin films. For this reason it is relatively easy to fabricate films of different composition. Due to the high kinetic energy of the laser ablation generated species, the PLD films can be grown under low substrate temperature. This is advantageous to reduce chemical inter-diffusion at the interface. It also helps to lessen the thermal induced stress and re-evaporation of as-deposited materials from the film surface. It definitely helps in fabricating films of materials which have low melting temperature. Other factors such as flexibility, fast response, and ability to process under ambient gases [2-6], give PLD a special favorable position over other film growth techniques such as molecular beam epitaxy (MBE), metal organic chemical vapor deposition (MOCVD), magnetron sputtering, etc.

The requirement of the PLD, comparing with other systems like MOCVD or ion beam sputtering, is low. The setup includes primarily a laser source and an experimental vacuum chamber. Since the interaction between photons and target surface dictates the ablation, the reaction between the laser source and the background gas can be neglected. Therefore, different types of gas of desired ambient pressure can be used without much limitation. Today PLD remains a premier thin film growth technique for many researchers.

The most undesirable concern of PLD is the limited film size that it can produce. Therefore, it is not viable to deposit thin films by PLD for commercial purpose.

Unexpected particulates with size of several micro-meters often exist in PLD films too. These particulates can seriously affect the films' performance, rendering it impractical for commercial device production.

Chapter 3

Characterization methods

3.1 Introduction

In order to obtain a clear understanding and better control of the properties of the as-deposited films, it is necessary to characterize the films with various experimental techniques. One possible application of c-MZO is in optoelectronics. In this study we have, in addition to studying the structural quality of various c-MZO thin films, examined closely to their electrical and optical properties also.

In this chapter, we introduce different thin film characterization techniques. To begin with, the crystal structure and epitaxial relationship of the films and the substrates have been characterized using x-ray diffractometer (XRD) and transmission electron microscope (TEM). The cubic phase of MZO has to be identified and verified. The electrical measurements yield the values of the resistivity of the c-MZO:In thin films. The temperature dependant semiconducting property and the final p-n junctions rectifying characteristics are evaluated via standard two-point and four-point probe measurement. The optical properties and band gap energies of c-MZO:In as functions of composition are investigated by transmittance spectroscopy and X-ray photoelectron spectroscopy.

3.2 Structural measurements

3.2.1 X-ray diffractometry (XRD)

X-ray diffraction (XRD) has been one of the most widely used non-destructive techniques for materials characterization. This method reveals the microscopic structure of the material. For anisotropic material such as ferromagnetic oxide, the identification of the preferred crystal orientation should be considered essentially. XRD provides a simple but powerful technique for phase identification and crystalline characterization. A Philip X'pert x-ray diffractometer is used to characterized the deposited c-MZO:In thin films and targets. The X-ray source using Cu target provides a strong K_α radiation with wavelength of 1.54Å. The K_β emission at wavelength of 1.39Å is blocked off by a Ni filter. All thin films are characterized by the three scan modes of the XRD.

1) theta-2 theta mode

When a parallel x-ray beam incident onto a single crystal material, it is scattered from all the periodically arranged atoms and interface. If the scattered waves are in phase, they interface in a constructive way and strong diffracted beams in some specific directions are obtained. The direction of the diffracted wave depends on the wavelength of the x-ray and the nature of the crystalline sample. The relationship of the crystal geometry, incident wavefront and the angle of diffraction can be expressed by the Bragg's diffraction equation.

The diffraction of the x-ray by a crystal can be described as depicted Fig. 3.1. In a Bragg-Brenteno mode, the family of the crystal planes can "reflect" the x-ray from an

incident angle θ according to Bragg's equation. To establish the Bragg's reflection, the parallel wave has to be maintained throughout the diffraction process. Therefore, between two lattice planes, the minimum length of the two wavefronts should be an integer. That is, the path difference between two wavefronts is equal to wavelength λ of the x-ray

$$\text{i.e.} \quad BC + CD = \lambda$$

$$\text{and} \quad BC = CD = d\sin\theta$$

$$\therefore 2d\sin\theta = \lambda$$

where *d* is the interplanar spacing between the two lattice planes

In theta-2 theta scan, the position of the x-ray source is fixed. When the sample on the stage rotates through an angle θ, the detector scans over an angle 2θ correspondingly. If Bragg's reflection is satisfied at any angle, a strong diffraction signal is detected. Typically, the rotation range of the detector is from 0° to 170° for the completed detection range. Experimentally, the choice of the scan range depends on the crystal structure of the material being investigated [3-1].

For polycrystalline materials, such as the sintered PLD targets, the orientation of the diffraction crystal grains is at random. In this case, powder diffraction technique is used. A large spot size of x-ray beam is incident on the sample surface. The spot size is supposed to cover many grains of the sample. If one specific grain orientation obeys the Bragg's law, diffraction appears. As the grains of the sample are oriented in three dimensions, the diffraction signal of a particular set of planes gives a circular shape, referred as Debye cones. For preferred oriented growth crystalline films or epitaxial

films, only diffraction peaks from one family of planes is detected. However, for polycrystalline films, the randomly oriented grains allow diffraction peaks from different families of planes to be seen, perhaps with weaker intensities.

After the interplanar spacing is found, the lattice constant can be calculated based on the cubic phase of the material, which is

$$d_{hkl} = \frac{a}{\sqrt{h^2 + k^2 + l^2}}$$ where h, k, l are the Miller indices.

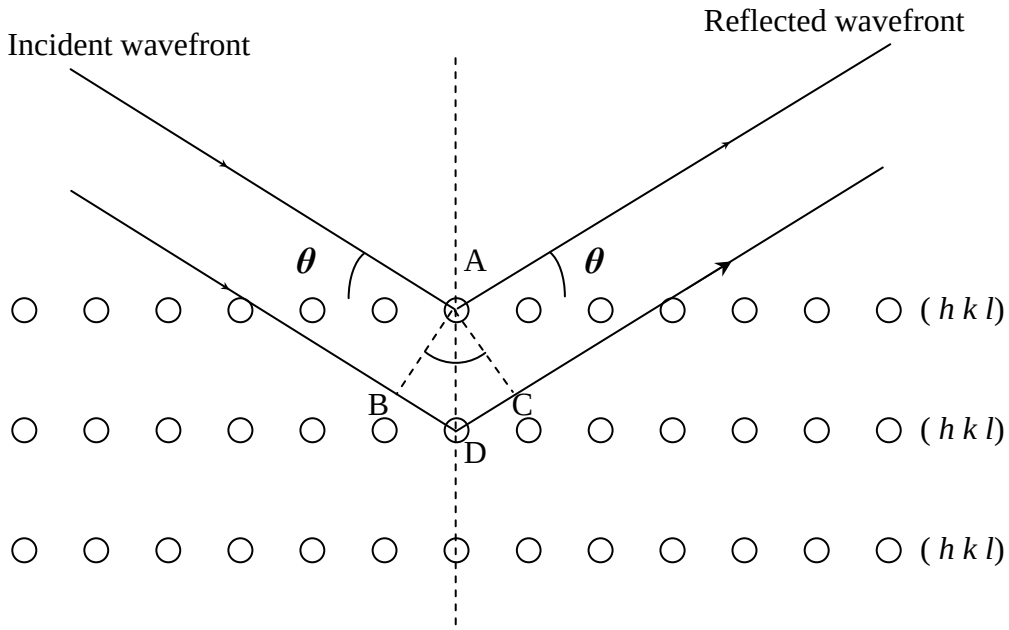

Figure 3.1 Schematic diagram of Bragg's reflection

2. Omega scan

Defects, dislocations, vacancies or lattice mismatch very often coexist in films fabricated by PLD. These undesirable features force individual grain orientation to deviate from perfect alignment with those of the substrates. The crystallinity of the films becomes poor. In omega scan mode shown in Fig. 3.2, the x-ray source and the detector are fixed at the Bragg's angle θ and 2θ respectively to obtain the maximum signal

intensity. Then we rotate (rocking) the sample for certain degrees parallel to the Bragg's reflection plane. A Gaussian profile is obtained. The full width half maximum (FWHM) is calculated from the curve. This value indicates quantitatively the grains alignment hence the crystallinity of the sample. The smaller the value, the better is the crystallinity. Typically, an epitaxial crystalline film is considered good if the value of FWHM is less than 1˚.

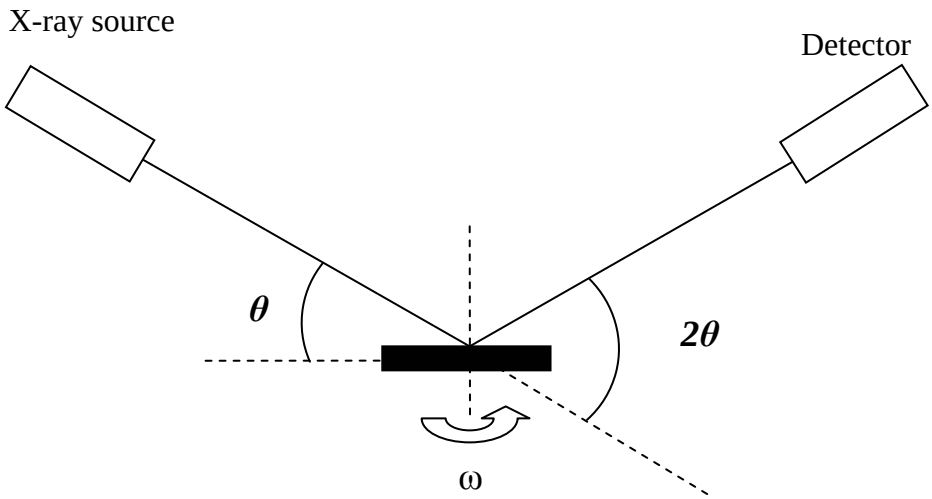

Figure 3.2 Schematic diagram of omega scan.

3. 360˚ φ-scan

When a film is grown on a substrate with the same crystal structure and similar lattice constant, the film is likely to have good in-plane alignment with the substrate. If this happens, it can be said that the film is epitaxially grown. Epitaxial growth is particularly important for the anisotropic material. The properties change with the growth direction, so it is necessary to grow the film with a preferred orientation.

Utilizing the 360˚ phi-scan of the XRD can examine the in-plane relationship between the film and the substrate. In Fig. 3.3, for cubic phase in-plane relation, when

we tilt the sample at 45˚, and rotate for 360˚ normal to the (0 0 1) plane of the film, Bragg's reflection of the (0 1 1) plane is satisfied four times during one completed cycle. For cubic structure, which is four-fold symmetric, there are four diffraction peaks in the 360˚ phi-scan profile. The separation between peaks is 90˚. For cube-on-cube epitaxy, the four peaks of the substrate should coincide with those four of the film at the same phi angles.

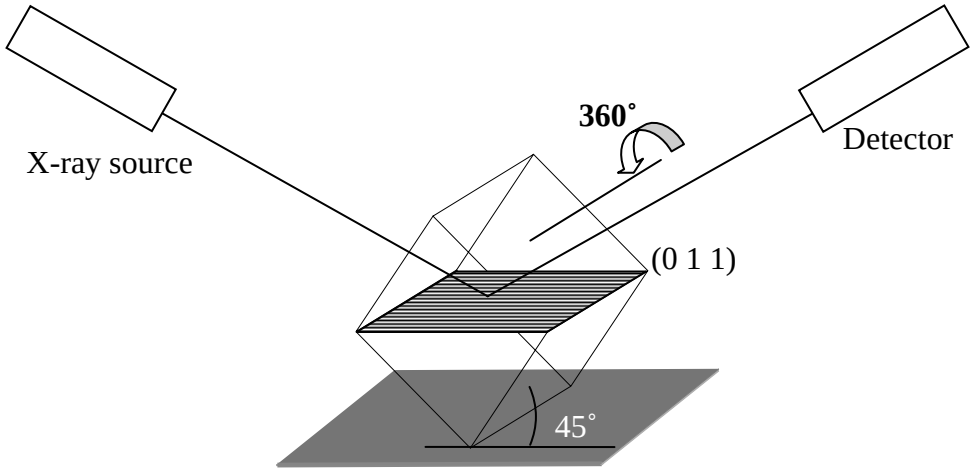

Figure 3.3 Schematic diagram of 360˚ phi-scan.

3.2.2 Transmission electron microscopy (TEM)

For optical microscopy, the resolution is limited by the wavelength of light. To view image of smaller scale, electron microscopy is employed. For thin film characterization, we often require image resolution down to nano scale. In this work a JOEL JEM-2010 Electron Scanning Microscope is used to study the microstructure and the epitaxial relation of the thin film and the substrate. TEM is a destructive technique in which sophisticated sample preparation is needed. The sample must be smooth and thin enough for the electron beam to transmit through. Thus, the sample is first mechanically polished to about 10μm thin. Then it is further etched by ion milling

before inserting into the TEM.

TEM mainly composes of an electron gun, objective lens and condenser lens. By applying an extra high tension, high speed electrons emit from the electron gun. De Broglie equation states that $\lambda = h/mv$, where λ is the wavelength, h is Planck's constant, m is the mass of the particle, and *v* is the velocity of the particle. Therefore, the higher the accelerating voltage, the smaller is the theoretical wavelength. Hence a better image resolution is achieved. Typically, the applied voltage of TEM can be up to 1MV. The corresponding wavelength is about 0.87pm, with the resolution of 0.1 nm [3-2].

The electron beam then travels through the electromagnetic lenses. TEM normally have two condenser lenses. The condenser-lens system is used to control the electron illumination on the specimen and on the viewing screen for functions such as viewing, focusing, and photography. After passing through the condenser lenses, the electron beam interacts with the specimen and enters the objective lens which is the first magnifying lens in the TEM, and the image is enlarged. Then the image is further magnified by other lenses and finally projected on the fluorescent screen.

Using the XRD scan results, the interplanar spacing associated with the lattice structure can be calculated according to Bragg's law. In TEM, the crystal structure can also be revealed from the diffraction pattern by the elastic scattering of the electron beam. Tuning the electron velocity to the x-ray wavelength range, for single crystal material, some discrete spots appear on the screen. In Fig. 3.4(a), each spot represents

one direction of plane. For the polycrystal with random orientation, some circular rings are recorded as one family of planes is aligned at all directions (Fig. 3.4(b)). For amorphous material, there is no well defined regular electron pattern on the screen.

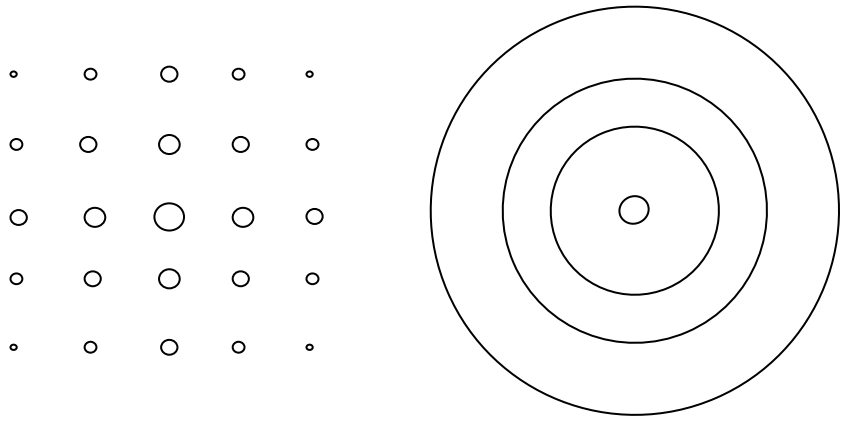

(a) (b)

Figure 3.4 The electron diffraction pattern of (a) single crystal and (b) polycrystalline material

3.3 Surface morphology

3.3.1 Atomic force microscopy (AFM)

The surface roughness of the film with sub-micron scale is examined by the Digital Instruments, Nanoscope IV atomic force microscopy. In Figure 3.5, the working principle of AFM is to utilize the intermolecular force between the tip and the sample surface. The tip places several nanometers above the surface. The coordinate of the tip is monitored by laser source connected to the photodiode. When the tip is scanning along the surface, the roughness causes the deflection of the cantilever, changes the reflection of the laser. The photodiode records the change of the spot and calculates the height of the material. In order to prevent direct contact of the tip and the sample that may damage the tip, there is a feedback circuit to maintain a constant separation between the tip and the surface by the PZT scanner.

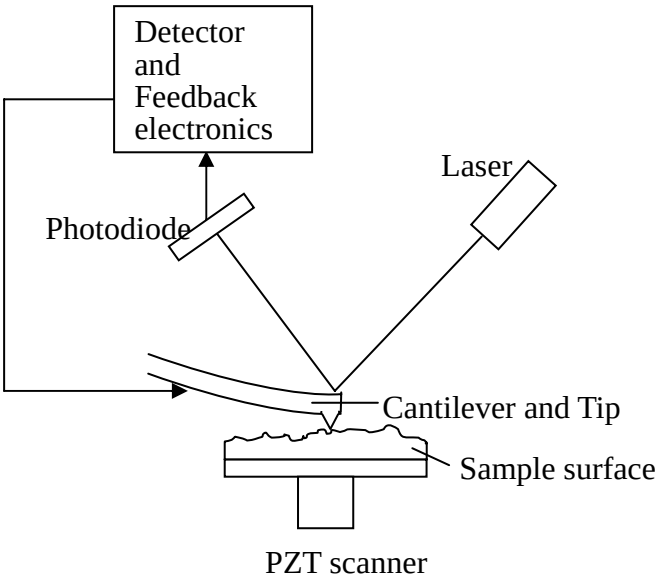

Figure 3.5 Schematic diagram of atomic force microscopy (AFM) setup

3.3.2 Scanning electron microscopy (SEM)

In surface morphology analysis, SEM is a very popular and useful technique because of the large depth of field. The image captured by SEM can give a more realistic picture as the depth profile is included. The higher magnification power than optical microscopy is another attractive feature for surface morphology studies. Therefore, SME is a commonly used technique even in biological and environmental material characterization. Field Emission Scanning Electron Microscope (FESEM) – JEOL JSM-633F and a Leica Stereoscan 4740 are used in the present project for examining the surface morphology of the PLD films.

The imaging process is obtained from detecting the secondary electrons. The electron beam is generated by applying several tenths of kilovolt to the source. The high kinetic energy electrons strike the sample, bombarding and knocking out the outermost electrons of the atoms. This is the secondary electrons. Secondary electrons come out from 1-10nm deep of the material surface. The electrons are detected by the Everhart-Thornley detector, a key component in the SEM. It converts the secondary electrons to light signal. The photons then enter the photomultiplier tube. The electrical signal is induced and amplified [3-2]. Finally, the SEM image is projected on a CRT monitor.

As electrons directly incident on the sample surface, the surface needs to be conductive. Otherwise, the specimen will accumulate large amount of electrons on its surface and generate a negative electric field. The field repels the incoming electrons, and causes erroneous distortion to the image. Therefore, a thin conductive layer such as

carbon or gold is coated on the surface to discharge and enhance the secondary emission. The metallic layer can also reduce the thermal damages.

3.4 electrical measurements

3.4.1 Temperature dependent resistivity

The resistivity of thin film is so important that proper evaluation is necessary. However, the cross-section of the film is small, it is impossible to attach parallel electrodes on the opposite side of the film. Instead, a parallel strip of electrode is deposited on the surface of the film which is shown in Fig. 3.6. Platinum (Pt) and gold (Au) are chosen as the electrode material because of its low resistivity and good ohmic contact. Pt is deposited by the PLD method, while Au is coated on film surface by sputtering. The resistance R is measured by a Keithley 6517A Electrometer. The sensitivity of the equipment is as high as pA. The resistivity, ρ of the film is calculated using the equation $\rho = R\frac{d \times W}{L}$, where d is the thickness, W is the width and L is the length of the film. They are indicated in the Figure 3.6. If the length of the film is sufficient long compared to the thickness, the measured resistivity of the film is reliable. This is the case for all our measurements.

The resistance of the film against temperature spanning from 20K to 380K is measured. The sample is mounted on the test stage of the cryostat running on close cycle liquid helium. Sample temperature down to 20K is possible. Then the electrometer measures the resistance of the film across the electrodes. The temperature is controlled by the Lake Shore 321 Autotuning Temperature Controller. The Labview software program monitors the electrometer and modulates the temperature controller.

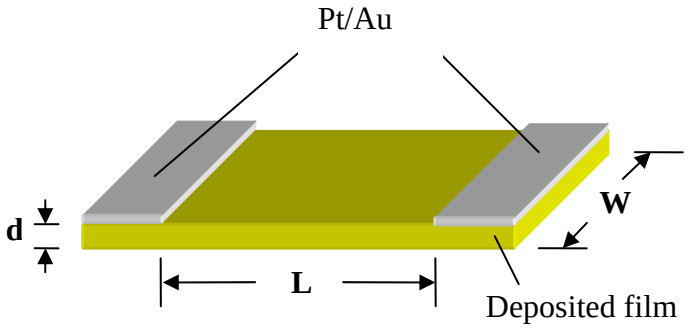

Figure 3.6 Schematic diagram of resistivity measurement

3.4.2 Current against voltage measurement

The Keithley 6517A Electrometer is also used to study the current-voltage characteristic for the all oxide p-n junction. Ohmic contacts are confirmed on each side of the junction. The electrometer applies the voltage from negative to positive value, and at the same time it measures the current across the junction. The duration of time measurement is 100ms for each interval. The equipment can detect the current signal from 20pA and 10mA. The operation of the electrometer and the temperature controller are monitored by the Labview software program. The I-V curve can be graphically displayed in real-time through the computer during the measurement.

3.4.3 Hall measurement

Biorad HL55WIN hall System is used to determine the carrier concentration of the n-type c-MZO:In doped thin films by the Hall Effect theory.

Hall Effect is based on the Lorentz force characteristic of a charged particle. When free carriers of the sample, such as electrons or holes, are experienced an electric field,

the electrostatic force will drift the carriers to move. At this time, a magnetic filed is applied perpendicular to the direction of the moving charge, schematically shown in Fig. 3.7. The particles are induced a force that make the trajectory of the carriers bend instead of horizontal. The direction of the Lorentz force can be deduced by the cross product of the velocity of the particle and the direction of the magnetic field

$$F = -q\vec{v} \times \vec{B}$$

The direction of the Lorentz force of electrons and holes are opposite. Lorentz force drives and accumulates the charged carriers to one side. When we measure the potential difference across the two edges of the sample, the hall voltage V_H is non-zero. The magnitude of the hall voltage is equal to

$$V_H = \frac{IB}{qnd}$$

where I is the current, B is magnetic field, q is electron charge, n is the carrier concentration and d is the thickness of the sample.

Therefore, when the sample is given a known current, magnetic field with measured thickness, the concentration of the carrier in the sample can be calculated by measuring the hall voltage. The n-type or p-type conduction can also be determined by the sign of the hall voltage.

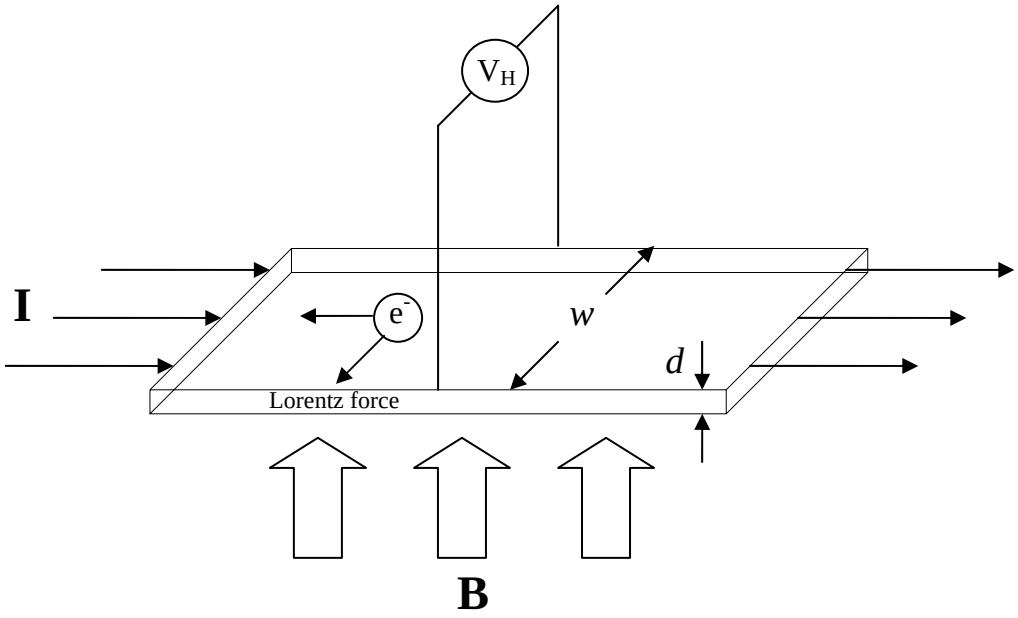

Figure 3.7 Schematic diagram of Hall Effect measurement

3.5 Optical measurement

3.5.1 Transmittance measurement

In semiconducting materials, the band gap energy E_g corresponds to the energy needed for electrons transit from the valence band to the conduction band, i.e. inducing free carriers. If E_g is larger than the energy of visible photons, no light will be absorbed by the material and the sample is said to be optically transparent. In k-space, when the transition from valence band to conduction band involves no change in k then the transition is called direct. If this is not the case, i.e. the transition associates with the phonon interaction, the transition is called indirect.

Transmittance of the films is measured by a Shimadzu UV-2550 UV-VIS Spectrophotometer. The spectrophotometer has light source spanning wavelengths from 190nm to 900nm. The transmittance is the ratio of transmitted intensity to the incident intensity.

$$T = \frac{I}{I_0}$$

where I and I_o are the intensities of the transmitted and incident waves respectively. From the transmittance spectrum, the absorption coefficient can be calculated from the relation

$$\alpha(\lambda) = \ln(1/T)/d$$

where $\alpha(\lambda)$ is the absorption coefficient at specific wavelength λ, T is the transmittance and d is the film thickness. After the absorption coefficient is converted, we estimate the direct and indirect band gap energy of the electron transitions. Plotting $(\alpha hv)^2$ and

$(\alpha hv)^{1/2}$ against photon energy, the extrapolation of the $(\alpha hv)^2$ and $(\alpha hv)^{1/2}$ against photon energy curve to $(\alpha hv)^2$ and $(\alpha hv)^{1/2}$ equal to zero are the direct and indirect transition energy bands respectively.

3.6 Composition analysis

3.6.1 SEM energy dispersive x-ray (EDX)

The element analysis from SEM EDX is based on the x-ray collection from the interaction of electron beam and sample. X-ray is produced from the inelastic scattering. When the electron beam has sufficient energy to knock off the inner core electron from the atom, secondary electron is produced while there is a vacancy in the inner orbital shell. The electron from the outer shell with higher potential energy fills the vacancy. The energy difference between two states is converted to x-ray. The energy of x-ray is related to the energy level of different shell, which is a finger print of the element. Thus, by evaluating the intensity and wavelength of x-ray, the concentration and the identity of element is revealed. In practice, the x-ray of $K_{\alpha 1}$, $K_{\beta 1}$, $L_{\alpha 1}$, $L_{\beta 1}$ and M_{α} are always measured based on the K, L, M shells of electrons.

3.6.2 X-ray Photoelectron Spectroscopy (XPS)

For surface analysis, Physical Electronics Phi5600 multi-technique system is used to determine the composition of the film.

It is essential to fully understand the material properties based on its chemical composition in order to design devices for the desired application purpose. For surface analysis, X-ray Photoelectron Spectroscopy (XPS) can serve this purpose by evaluating the binding energy of the material. The binding energy reveals the chemical state and the electronic state of the elements. The working principle is that the test sample is irradiated with monochromatic x-ray. The photon will ionize the atom and the electron

in the inner shell is emitted. The photoionized electrons are collected by the energy analyzer. Then the binding energy is known by the conservation of energy

$$h\nu = E_B + E_K$$

where $h\nu$ is the x-ray photon energy, E_B is the binding energy of the electron from a particular energy level, and E_K is the kinetic energy of the ejected photoelectron. From the equation, the photon energy of the x-ray is the sum of the binding energy and the kinetic energy of the electron. X-ray with MgK_α of photon energy 1253.6eV and AlK_α of photon energy 1486.6eV are usually used [3-3]. When the kinetic energy is calculated by the energy analyzer, the binding energy is known. The binding energy contains the information of the electron states of the element in the sample. Thus, the element identification and chemical information are obtained.

Films examined by the XPS can also be sputtered by the argon plasma layer-by-layer. Then the composition of the film can also be analyzed at the particular depth. Therefore, the composition against the depth profile is plotted. This technique is useful to evaluate oxide materials. The concentration of the oxide may vary at different distance from the surface. From the XPS spectrum, the peak of the binding energy shift means the electron configuration changed and the chemical state altered.

Chapter 4

Fabrication and characterization of In-doped c-MZO thin films on LAO and MgO substrates

4.1 Introduction

For decades, ZnO has been a favorite material for many researchers because of its interesting properties. With impurity dopants, ZnO can be used as piezoelectric or ferromagnetic material, transparent conducting oxide, photo luminescence semiconductor etc. The wide range of applications of ZnO penetrates into areas such as medicine, electronics, optoelectronics, pharmacy and communication [Robert Eason 2006][2-2]. One major focus of ZnO is the optoelectronic application utilizing the wide band gap energy (about 3.37eV direct band gap) and high excitonic binding energy (about 60meV). These advantages are expected to occur in the c-MZO system.

Intrinsic ZnO is a poor conducting material. It has been shown that with group III impurity doping (e.g. Al, Ga, In etc.), the electrical conduction can be substantially increased. Indium doped ZnO (wurtzite) gives good n-type conduction. Therefore, we choose indium as the doping impurity to improve the electrical conducting of c-MZO in our study.

The band gap energy of In_2O_3 is 3.7eV. This band gap value can be utilized to tune

the band gap energy of pure c-MZO which is between 5.4~7.8eV. The cubic structure of In_2O_3 (lattice constant of 10.1Å [4-1]) may be beneficial in synthesizing single phase c-MZO. The addition of Mg leads to the reduction of conductivity. It can be attributed to the impurity scattering [4-2]. In-doped c-MZO donates electrons by substituting In ion into the Zn site. This competes favorably against the increase of resistivity of Mg ion addition. In general, the conductivity is proportional to the concentration of indium.

In this chapter, we report the fabrication of c-MZO:In target, and epitaxial thin films deposited on MgO and LAO substrates by PLD. The main theme is to reveal the change of properties of c-MZO:In thin film against processing parameters such as substrate temperature and the doping concentration. We compare the structural, electrical and optical aspects of the as-prepared films in a few series of experiments. The microstructure and the surface morphology of c-MZO are characterized by the X-ray diffractometer (XRD), transmission electron microscopy (TEM), atomic force microscopy (AFM) and scanning electron microscopy (SEM). The electrometer and low temperature cryostat help measure the resistivity against temperature over the range of 20K - 380K. These measurements provide clear evidence of the semiconducting behavior of the c-MZO thin film. Transmittance test provides a strong support for good optical transparency of the film. The composition changes among the powder mixture, targets and thin films are revealed by SEM-EDX and X-ray photoelectron spectroscopy (XPS). Finally, we report the optimal PLD deposition condition for fabricating transparent conducting c-MZO:In thin films with epitaxial relationship.

4.2 Fabrication and characterization of In doped- c-MZO target

4.2.1 Fabrication of In doped- c-MZO targets

The targets of indium doped c-MZO were made by us in our own laboratory, so their compositions can be varied according to our requirement. They were prepared via conventional solid state reaction of constituent MgO (99.99%), ZnO (99+%) and In_2O_3 (99.999%) powders. The powders immersed in ethanol were first evenly mixed by ball milling for at least 6 hours. Then the mixture was dried in the oven and pressed into pellets. They were calcinated twice at 1100˚C for 10 hours in air. The final treated powder was pressed into a 2.5 cm circular disc of 0.5 cm thick by a 4 tones press at room temperature before it was sintered at 1350˚C for 10 hours in air. In order to fabricate the c-MZO thin films with different indium content, a series of c-MZO targets with 2, 4, 8 and 10 at. % of indium was made. Most targets used 1:1 atomic ratio of Mg to Zn.

4.2.2 Structural characterization of In-doped c-MZO targets

All targets were characterized by the x-ray powder diffractometer. Fig. 4.1 and Fig. 4.2 show the diffraction peaks of pure $Mg_{0.5}Zn_{0.5}O$ and c-MZO:In targets respectively. It can be seen that the diffraction peaks from both the hexagonal ZnO and cubic MgO phases are present. When indium is introduced in the system, some peaks are shifted and some unknown peaks exist. These peaks may come from the phases of In_2O_3, mix-phases of ZnInO and MgInO. In order to fabricate single phase of c-MZO thin film with preferred orientation, templates of MgO and LAO (0 0 1) substrate were used.

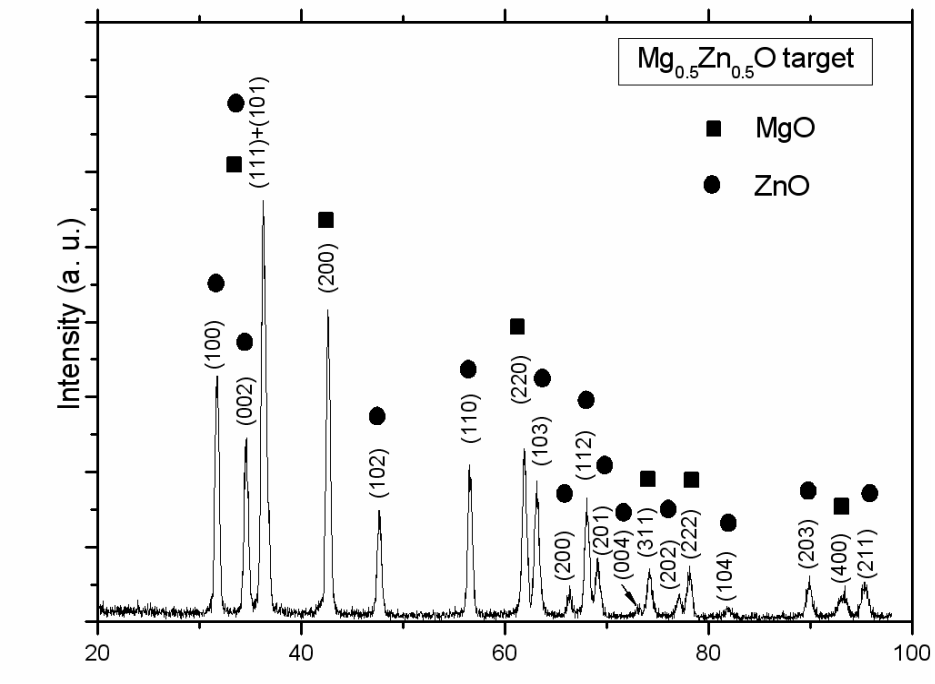

Figure 4.1 XRD powder diffraction of $Mg_{0.5}Zn_{0.5}O$ target

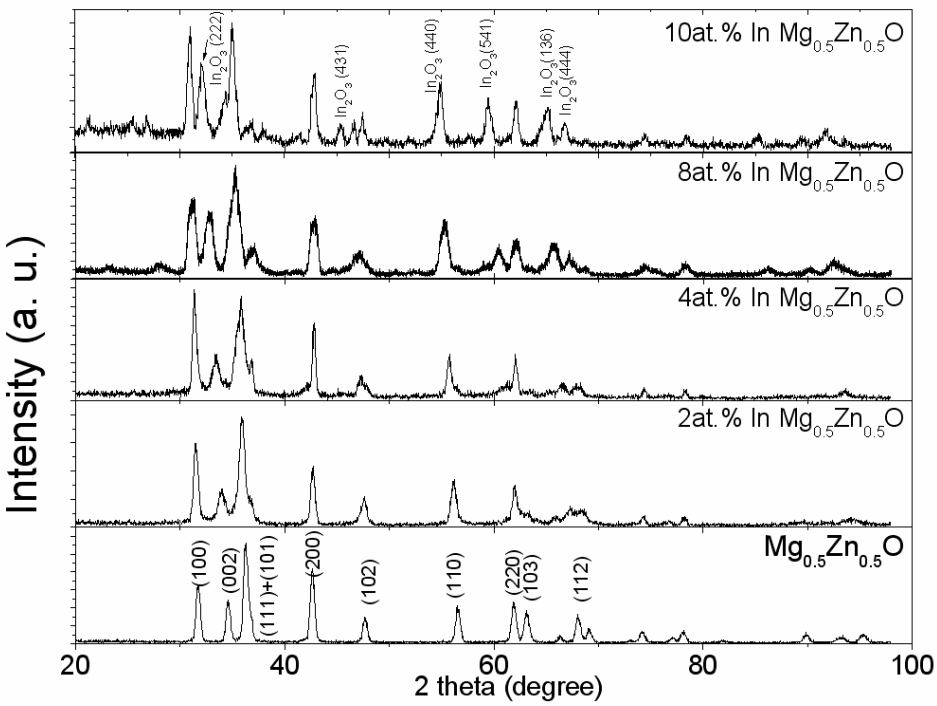

Figure 4.2 XRD powder diffraction of c-MZO targets with different indium content

4.2.3 Composition analysis of In-doped c-MZO targets

SEM-EDX reveals the composition changes of the c-MZO targets after a series of thermal treatments during preparation. The results are shown in table 4.1. In most of the cases, the concentration of In substantially increases while the chemical ratio of Mg to Zn is maintained. Even though the equipment has 5 % errors in itself, the changes appear real. The reason is still not known at present. For simplicity, we use sample 1 represent pure $Mg_{0.5}Zn_{0.5}O$ target; sample 2, 3, 4, 5 indicate the $Mg_{0.5}Zn_{0.5}O$ target with indium doping of 3.9 at. % , 8.2 at. %, 15.8 at. % and 17.7 at. %

Based on the variation between the pre-sintered target and the target after treatment, the nominal target name is corrected according to the SEM EDX result and stated in the last column of table 4.1. Moreover, for the films deposited from the nominal target are given the same index with the target.

Target	Mg atomic %	Zn atomic %	In atomic %	The nominal thin film deposited from the target
$Mg_{0.5}Zn_{0.5}O$	45.8	54.2	0	$Mg_{0.5}Zn_{0.5}O$
2 at. % In $Mg_{0.5}Zn_{0.5}O$	56	40.1	3.9	4 at. % In $Mg_{0.5}Zn_{0.5}O$
4 at. % In $Mg_{0.5}Zn_{0.5}O$	48.6	43.2	8.2	8 at. % In $Mg_{0.5}Zn_{0.5}O$
8 at. % In $Mg_{0.5}Zn_{0.5}O$	43.5	40.5	15.8	16 at. % In $Mg_{0.5}Zn_{0.5}O$
10 at. % In $Mg_{0.5}Zn_{0.5}O$	44.9	37.4	17.7	18 at. % In $Mg_{0.5}Zn_{0.5}O$

Table 4.1 The composition variation of the c-MZO targets

4.2.4 Deposition of In doped c-MZO thin films on MgO and LAO substrates

We deposited c-MZO:In thin films on MgO (0 0 1) and $LaAlO_3$ (LAO) (0 0 1) substrates by KrF 248nm wavelength excimer laser. The lattice constant of MgO and LAO substrates are 4.21 Å and 3.78 Å respectively. As mentioned in section 1.2, the c-MZO thin film has a lattice constant of 4.28Å. The lattice mismatches are therefore about 1.6% with MgO and 11.6 % with LAO. The substrate temperature is monitored by the thermal couple implanted inside the substrate holder. The base pressure of the experimental chamber is $2\sim7\times10^{-5}$ Torr. The substrates are normally placed at 4.5 cm away from the target with the laser fluence typically maintained at 4 J cm^{-2}. The repetition rate of the laser is fixed at 10Hz, with a deposition time of 30 minutes following 20 minutes post-deposition annealing.

The deposited thin films were characterized by XRD. Fig. 4.3 shows the XRD pattern of c-MZO grown on LAO substrate. For hexagonal ZnO, the diffraction peak of (0 0 0 2) should appear at 36.5˚. From the figure shown, the signal from hexagonal ZnO phase is absent. Instead, strong diffraction peaks of c-MZO (0 0 2) is observed at about 42.7˚. This indicates that the cubic phase of c-MZO exists with the lattice constant about 4.23Å. In the 360º phi-scans profile depicted in Fig. 4.4, the 4-fold symmetric diffraction peaks from the (0 2 2) family of planes reveal that the orientation of the film has twisted 45˚ in-plane relative to the substrate. This is attributed to the preferred domain matching between c-MZO and LAO. For the film grown on MgO substrate, the diffractions of pure c-MZO film with cube-on-cube growth are suspected. However, due to the closeness of the lattice constants of c-MZO and MgO, their diffraction peaks can not be resolved from the XRD profile. In order to demonstrate that c-MZO can be

successfully grown on MgO substrate epitaxially, the XRD profile of c-MZO:In deposited on MgO substrate is shown in Fig. 4.5. As the lattice constant of In_2O_3 is about 10.1Å, the substitution of indium enlarges the unit cell of c-MZO so that the Bragg's peaks of the film are shifted and can be resolved from the strong MgO substrate signal. In Fig. 4.6, the 360˚ phi-scans of c-MZO:In on MgO further confirms the cube-on-cube epitaxial relationship between the film and the substrate.

The SEM cross section and TEM electron diffraction images of the c-MZO:In film deposited on MgO are shown in Fig. 4.7 and 4.8. The cross-section image reveals that the film is about 500 nm thick. The diffraction pattern clearly suggests single cubic phase of c-MZO:In thin film and the cube-on-cube epitaxial relationship between the film and the substrate. It is also noted that the lattice constant of the sample is very close to that of the MgO substrate. The lattice mismatch between them is no bigger than 5%.

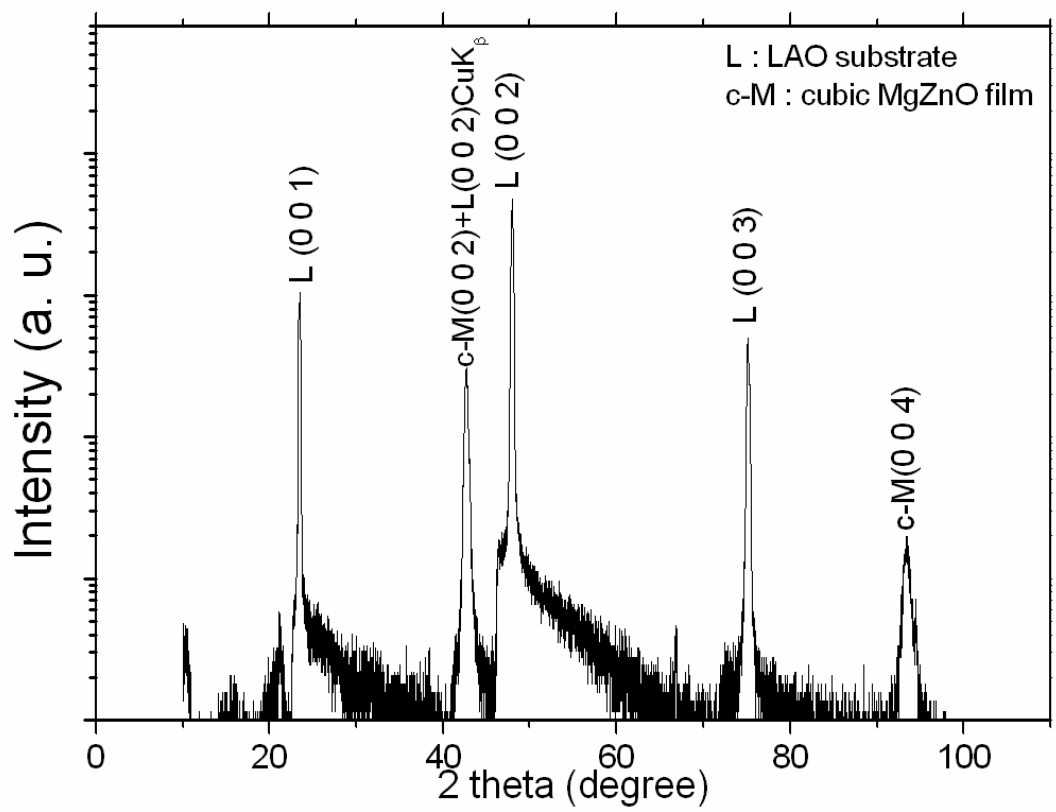

Figure 4.3 XRD θ-2θ scan of c-MZO film on LAO (0 0 1) substrate

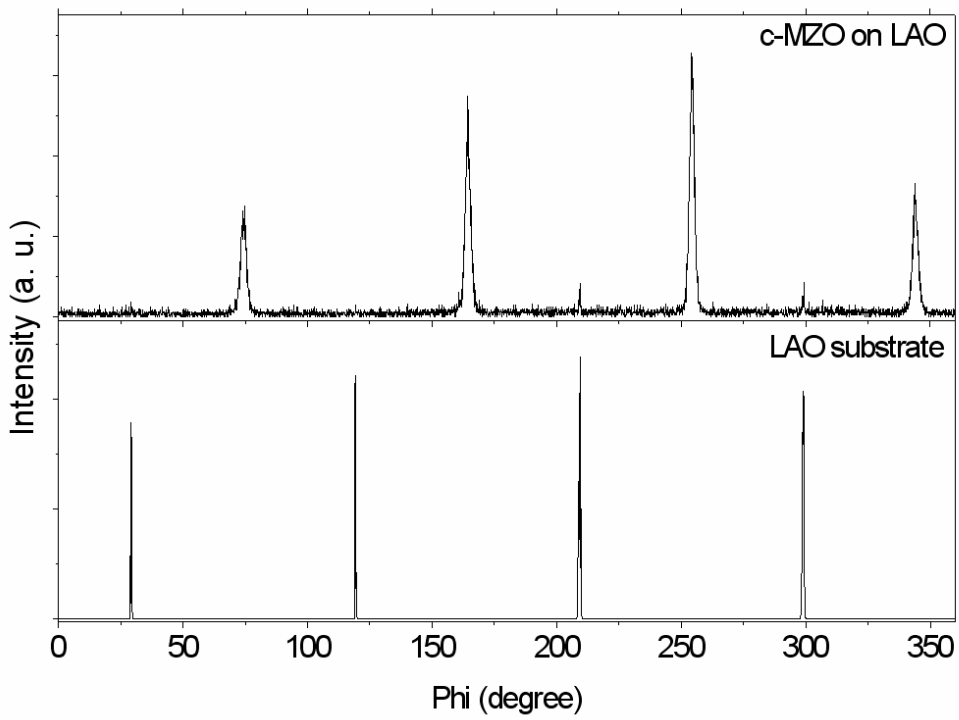

Figure 4.4 XRD 360˚ phi-scans of c-MZO film on LAO (0 0 1) substrate

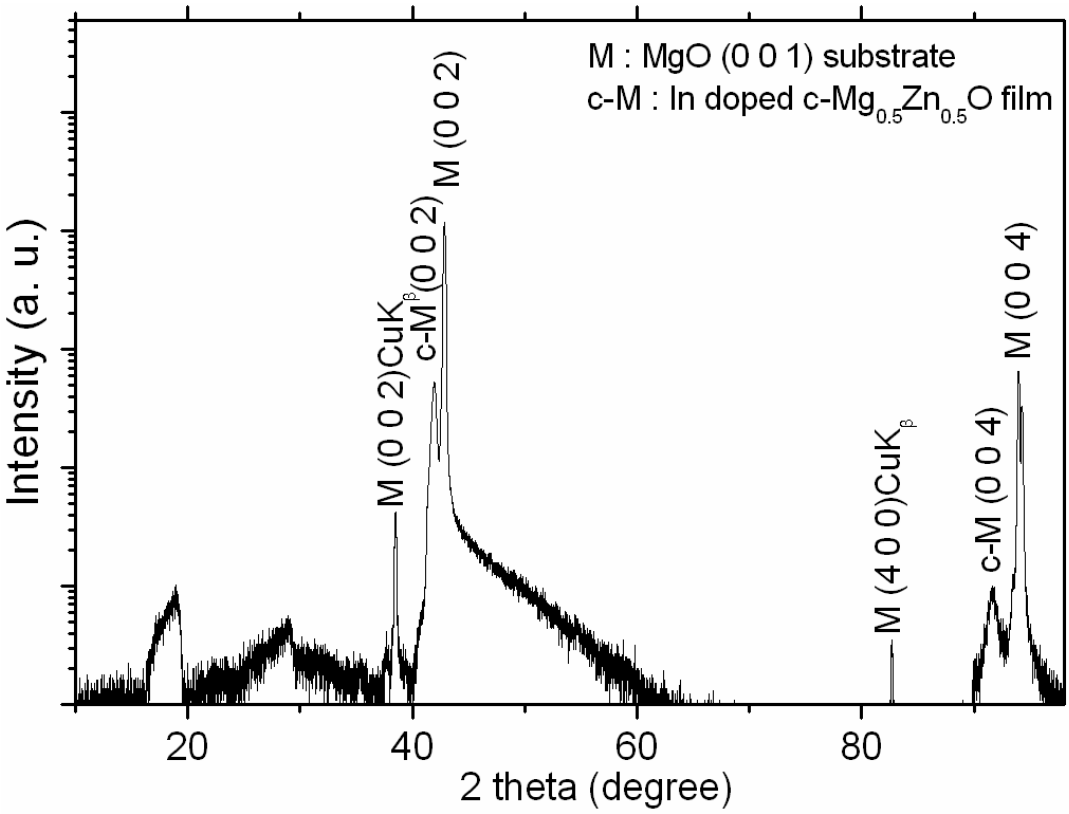

Figure 4.5 XRD θ-2θ scan of 4 at. % c-MZO:In thin film on MgO (0 0 1) substrate

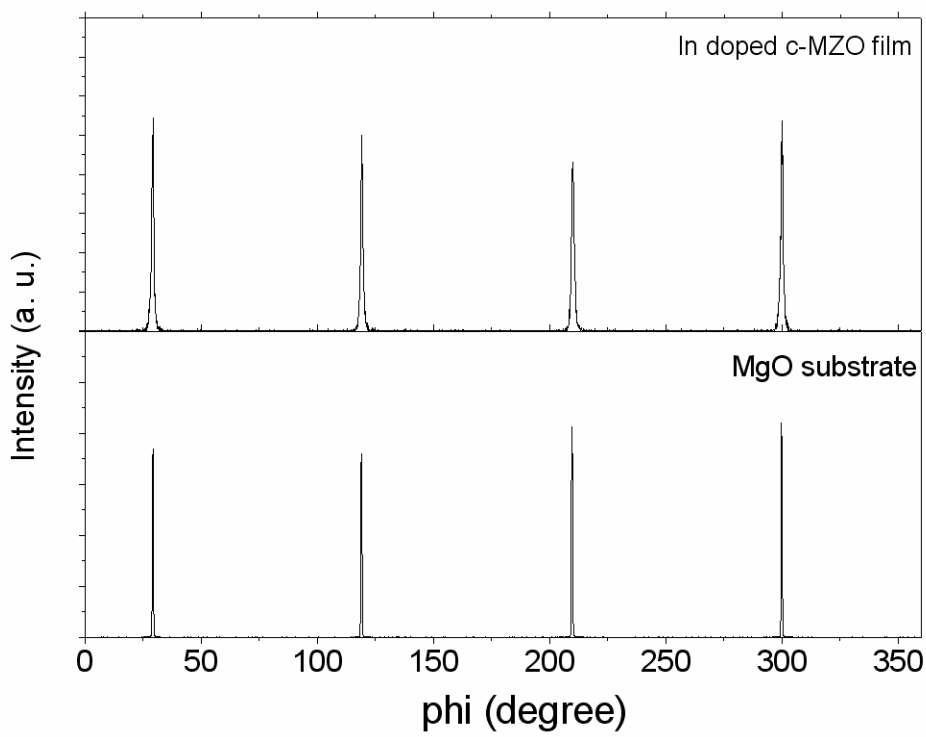

Figure 4.6 XRD 360˚ phi-scans of c-MZO thin film on MgO (0 0 1) substrate

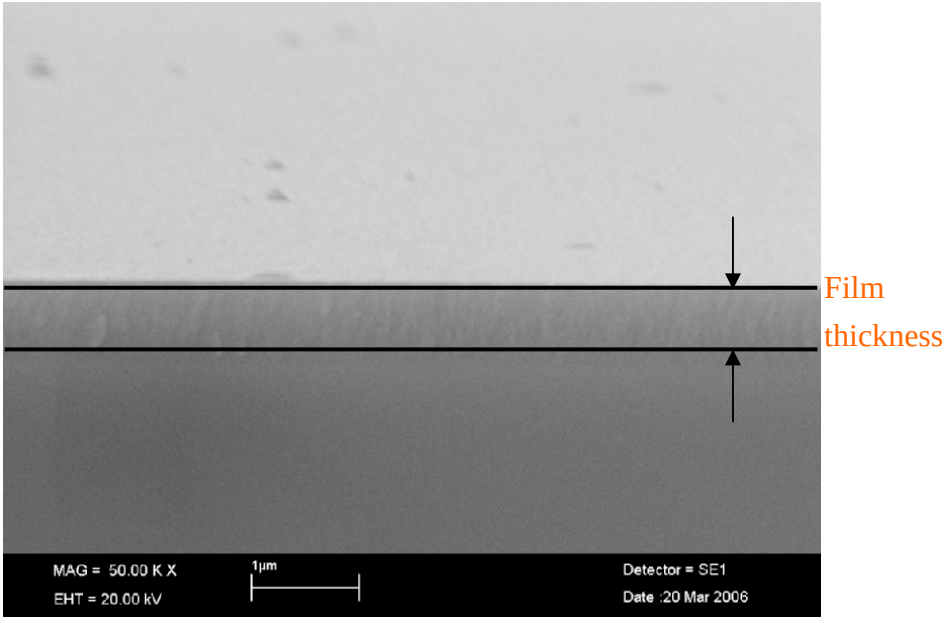

Figure 4.7 SEM cross section image of c-MZO:In on MgO (0 0 1)substrate

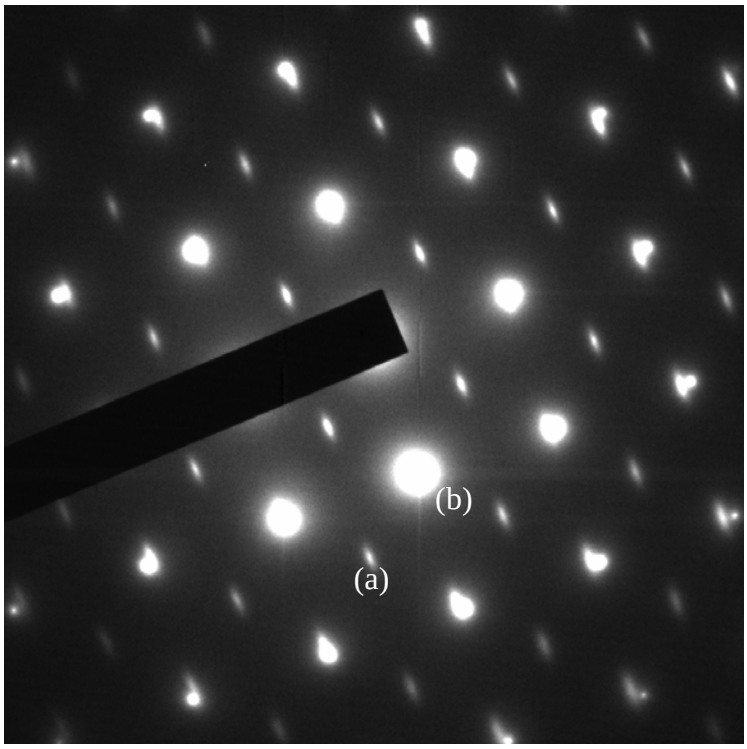

Figure 4.8 TEM electron diffraction pattern of c-MZO:In thin film (point a) on (b) MgO (0 0 1) substrate (point b)

4.2.5 Composition variation of In-doped c-MZO thin films

The compositions of various c-MZO:In thin films were studied by XPS. The amounts of Mg, Zn and In found in films are different from that of the target. Table 4.2 lists the concentration variation among the three elements in the sintering targets and the deposited films. Comparing the composition, it is seen that the Mg and In contents in the film are substantially increased (or that of Zn is reduced). This finding agrees well with the fact that Zn is preferentially vaporized during the deposition due to the much higher vapor pressure of Zn than those of Mg or In. Fig. 4.9 is the XPS studies of the concentration gradient of the 18at. % In doped $Mg_{0.5}Zn_{0.5}O$ film deposited at 300˚C. The total sputtering depth is about 100nm. Large amount of carbon is seen to attach on the surface of the film because of the presence of dust and dirt. The relative contents of Mg, Zn, and In are not constant. Their measured concentrations are often altered by the presence of carbon at the film surface. After sputtering several nanometers, no other impurities are found. The composition thus measured and calculated is then more accurate and reliable.

Target (deposition temperature)	Mg atomic %		Zn atomic %		In atomic %	
	Film comp.	(Target comp. measured from SEM EDX)	Film comp.	(Target comp. measured from SEM EDX)	Film comp.	(Target comp. measured from SEM EDX)
2.3 at. % In $Mg_{0.35}Zn_{0.65}O$ (600˚C)	59.1	(43.5)	33.4	(52.8)	7.5	(3.7)
16 at. % In $Mg_{0.5}Zn_{0.5}O$ (600˚C)	78.5	(43.5)	3.5	(40.5)	18	(15.8)
18 at. % In $Mg_{0.5}Zn_{0.5}O$ (600˚C)	68.1	(44.9)	5.7	(37.4)	26.2	(17.7)
18 at. % In $Mg_{0.5}Zn_{0.5}O$ (300˚C)	54.7	(44.9)	27	(37.4)	18.3	(17.7)

Table 4.2 Composition variation of c-MZO:In from sintered target to deposited film

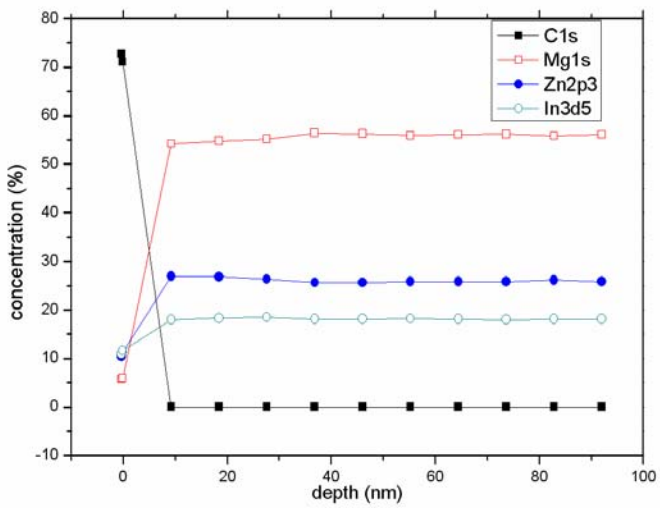

Figure 4.9 The relative compositions of 18 at. % c-MZO:In film deposited at 300˚C

4.3 Characterization of In-doped c-MZO thin films against doping concentration

4.3.1 Phase characterizations

While we have demonstrated epitaxial growth of c-MZO:In thin films on MgO and LAO substrates, we have also analyzed the influence of indium substitution in the c-MZO matrix. Fig. 4.10 shows the XRD θ-2θ scans of the c-MZO films doped with different amount of indium. It is noted that when the concentration of the indium increases, the lattice constant of the c-MZO:In increases also. This is of no surprise as the ionic radius of In is much larger than those of Mg and Zn. The substitution of indium in Zn site enlarges the unit cell of the film. Therefore, in the inset of Fig. 4.10, the Bragg's reflection peak shifts to the left, meaning that the lattice constant increases. For In concentration from 4 at % to 18 at%, the lattice constant expands from 4.30 Å to 4.36Å (Fig. 4.11).

Apart from the lattice constant, the crystallinity of the film with different indium contents is measured. The omega scan of the XRD of the c-MZO:In is plotted in Fig. 4.12. The result suggests that the introduction of the indium atoms degrades the crystallinity of c-MZO. For films deposited at 600˚C substrate temperature, the FWHM of the 4 at % In doped c-MZO:In is about 0.87˚. It increases to 1.9˚ when the In content is raised to 18 at. %.

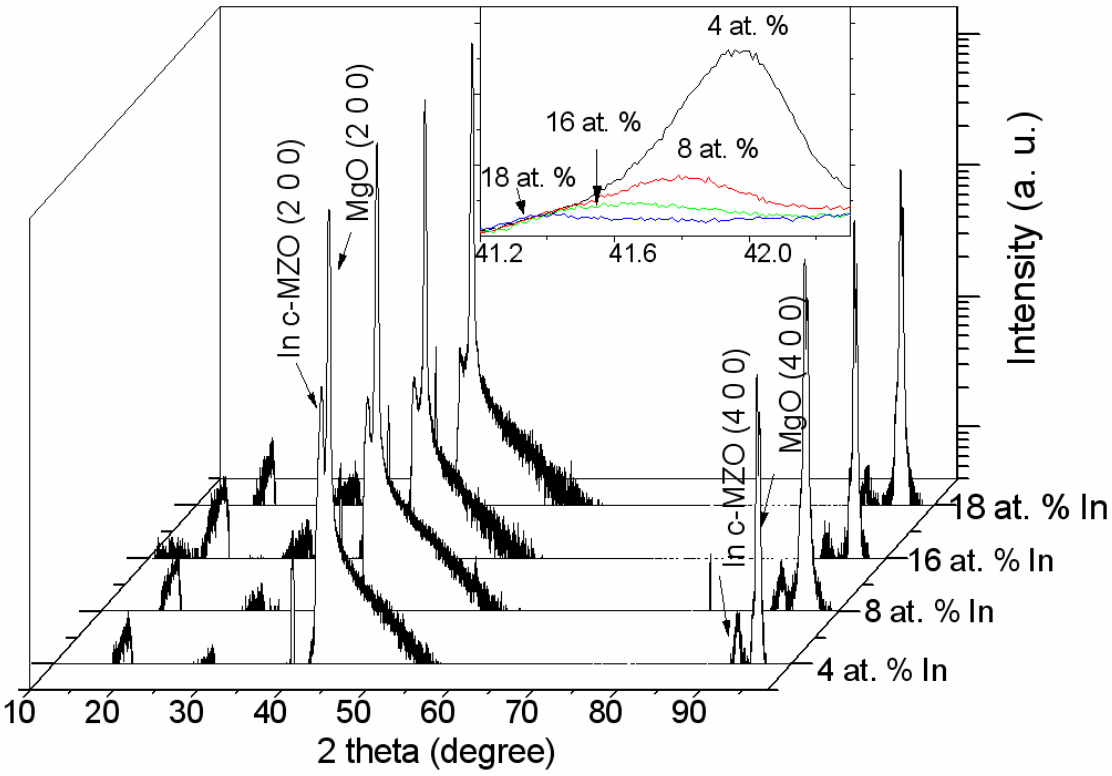

Figure 4.10 XRD θ-2θ scans of c-MZO thin films against indium content.

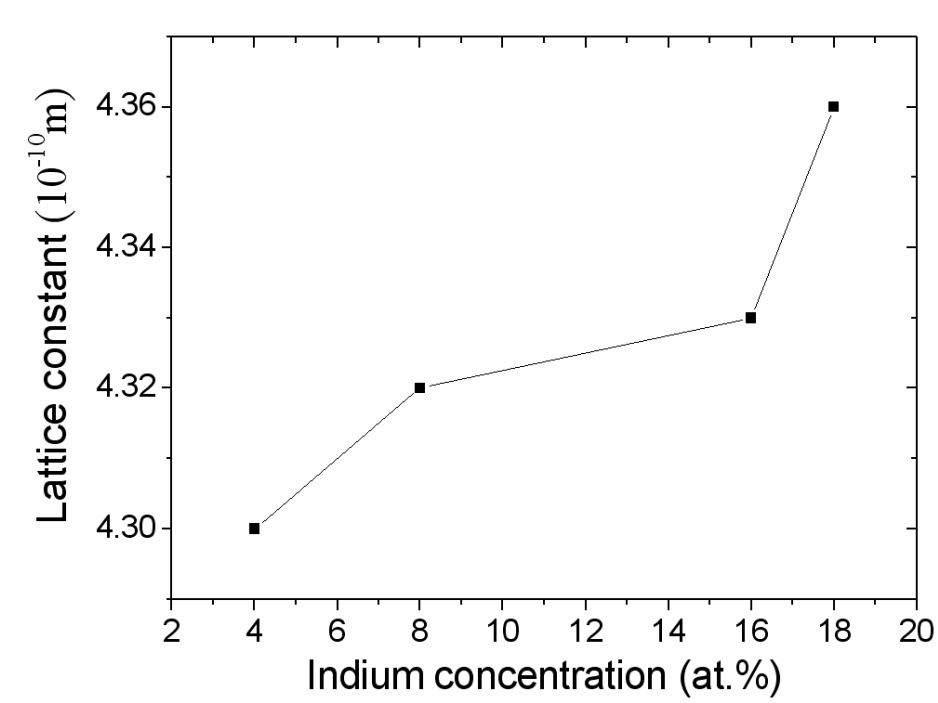

Figure 4.11 Lattice constants of c-MZO thin films against indium content.

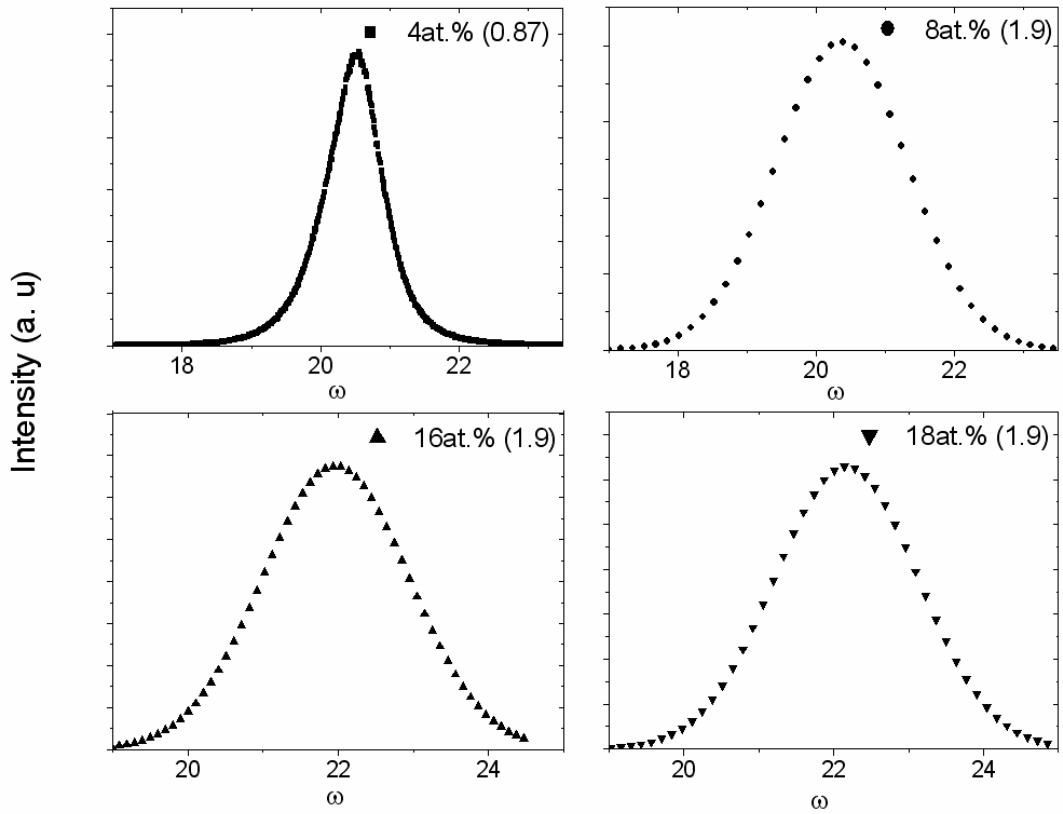

Figure 4.12 XRD ω scans of c-MZO (0 0 2) diffraction plane with different indium content

4.3.2 Surface morphologies

Fig. 4.13 shows the SEM pictures of the surface morphology of the c-MZO thin films doped with different amount of indium and grown on (0 0 1) MgO substrate. The pure c-MZO film gives a very flat and smooth surface. The grain size is so small that no features are discernable. After the introduction of indium, relatively flat surface can also be seen in 4 at. % of indium doped film. When the In content is increased to 8 at %, the surface roughness is noticeably increased. At about 16 at % In doping, filiform-like structure appears on c-MZO film. As in the usual case, films deposited at high vacuum always give a better and smooth surface. Large particulates are normally

not observed. This is because the laser induced plasma is adiabatically expanded and no gas phase condensation occurs.

In order to obtain a quantitative measurement of the surface roughness, the profile of the 18 at.% In doped c-MZO thin film deposited at 600˚C is characterized by AFM. The image is shown in Fig. 4.14. The scan area of the sample is (2.5x2.5) μm^2. The AFM measurement yields a RMS surface roughness is about 4.8nm.

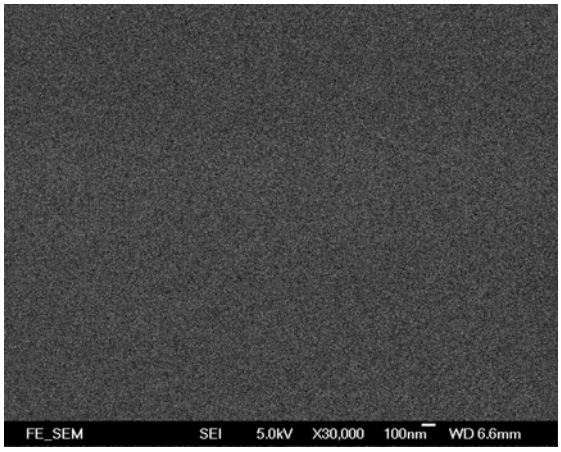

(a)

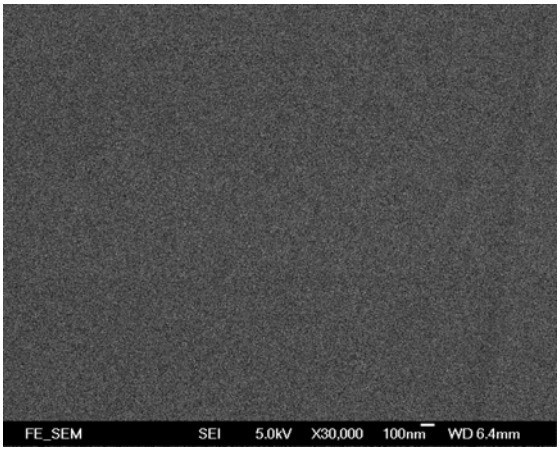

(b)

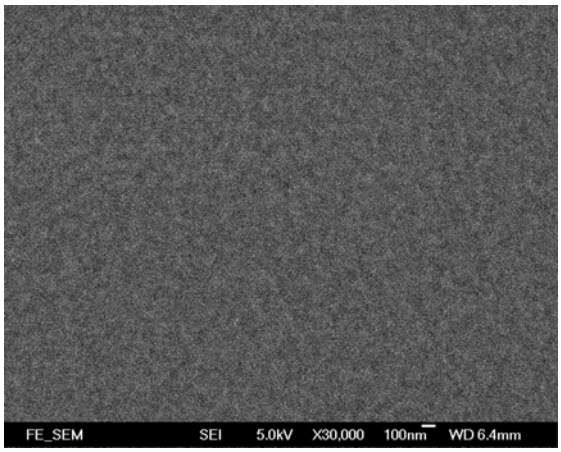

(c)

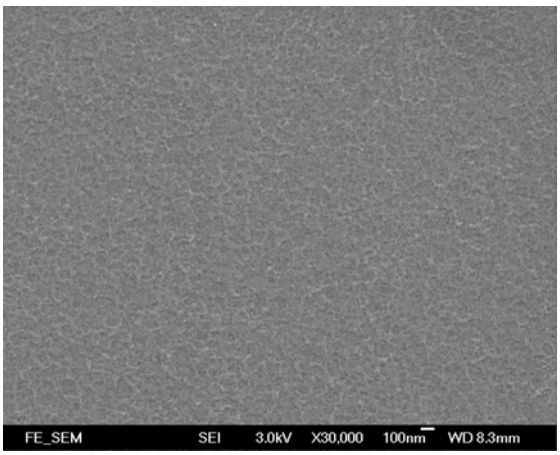

(d)

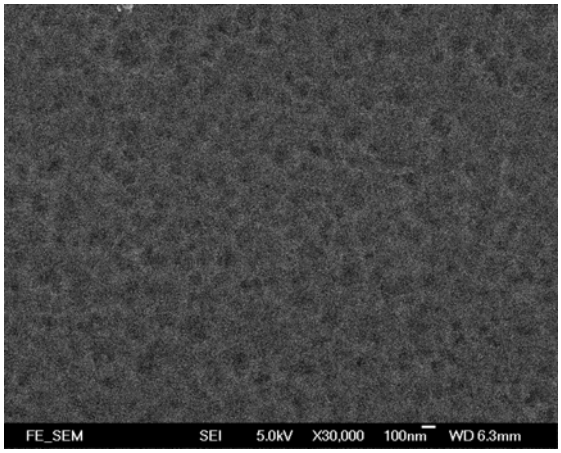

(e)

Figure 4.13 SEM images of (a) pure c-MZO, (b)4, (c)8, (d)16, (e)18 at. % indium doped c-MZO thin film surface.

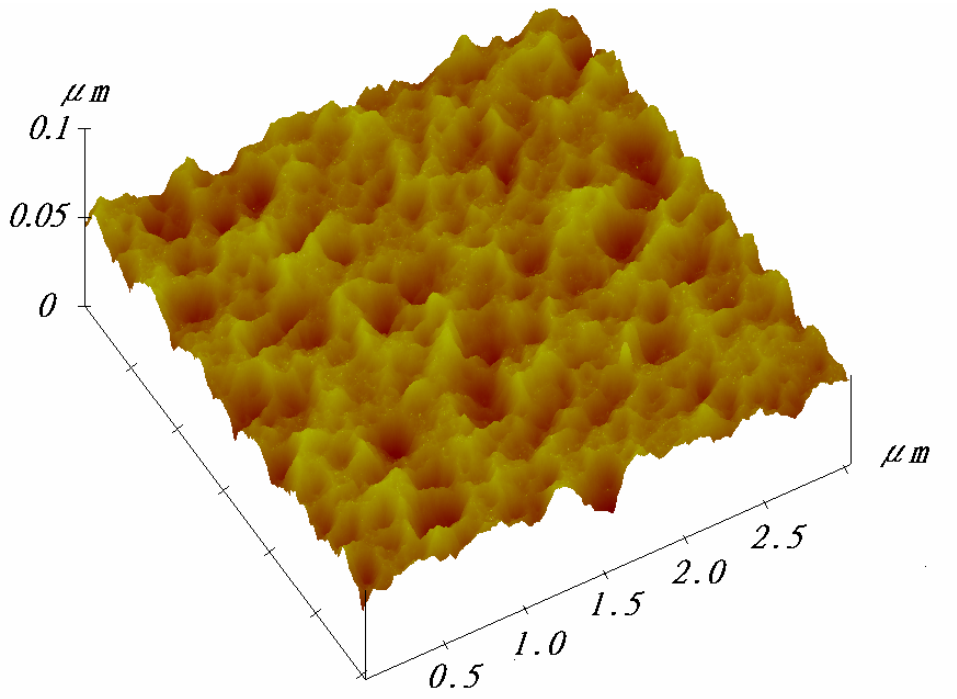

Figure 4.14 AFM image of 18 at % c-MZO:In thin film.

4.3.3 Electrical characterizations

The electrical conduction of the metal oxide originates from oxygen vacancies and the impurity dopant. The free carrier can be expressed by the following chemical equations

$$O_o \Leftrightarrow \frac{1}{2}O_2 + V_o^+ + e^-$$

$$In_2O_3 \Rightarrow 2In_{zn}^+ + 3O_o + V_{In}^{2-}$$

$$= 2In_{zn}^+ + \frac{3}{2}O_2 + 3V_o^+ + V_{In}^{2-} + 3e^-$$

O_o -The oxygen in the oxygen site
O_2 - Oxygen gas
V_o^+ - Vacancy of oxygen site with positive charge
In_{zn}^+ -Indium in the zinc site with positive charge
V_{In}^{2-} -Vacancy of Indium site with negative charge

e -electron

In_2O_3 - indium oxide

The equations express the idea of the free carrier generation. Under high vacuum and high temperature, the oxide escapes from the film, leaving an oxygen vacancy with negative charge. With the addition of In_2O_3, the free electrons is generated from the substitution of In into zinc site.

From the above equations, the introduction of group III element into the oxygen deficient c-MZO film is desired. In order to maximize the conductivity we therefore deposit the film under high vacuum and use In doped targets. The resistance of the film against temperature is measured and shown in Fig. 4.15. The resistance of the film is inversely proportional to the ambient temperatures from 380K to 20K. This result clearly demonstrates that the c-MZO:In film has semiconducting property. From the RT measurements, we can further deduce their relationship by plotting the Napierian logarithm of the resistance against the different power of temperature. In Fig. 4.16(d), a roughly straight line is obtained, so we can approximately conclude the relationship between the resistance and the temperature as:

$$Ln(R) \propto (T)^{-\frac{1}{8}}$$

$$Ln(R) = A + y \times T^{-1/8}$$

Where y and A are the slope and the intercept of the graph

From the graph, put y =3.81, A=6.525

$$Ln(R) = 6.525 + 3.81 \times T^{-1/8}$$

$$R = 682e^{3.81T^{-1/8}}$$

The excellent match between the experimental result and the empirical equation is shown in Fig. 4.15. The resistance R is seen to be linearly proportional to $T^{-1/8}$.

Figure 4.17 shows the Ln-plot of conductivity against 1/T. The activation energy for electrical conduction, which indicates the energy for an ion to hop to a free hole site, can be evaluated from Arrhenius equation $\sigma = A\exp[-E_a/kT]$. E_a is the activation energy, A is a constant and k is the Boltzmann constant. In the figure, the slop of the ln(σ) against 1/T graph represents the activation energy of the c-MZO:In system. However, as the relationship between the electrical conduction and temperature is not clear, the conductivity against temperature may not obey Arrhenius equation.

The resistivity of the films is highly dependant to the concentration of indium. Their relationships are plotted in Fig. 4.18. For intrinsic c-MZO films, the resistivity can be as high as 3×10^{7} Ωcm. They are said to be insulating. The resistance drops when indium is incorporated in the film. At about 18 at. % indium doping, the resistivity is down to 5.5×10^{-2} Ωcm. The graph shows the qualitative dependence of the resistivity against indium content. The absolute concentrations of zinc and magnesium associated with the crystalline microstructure change with the indium content. The conclusion is that the drop of resistivity of the film correlates with the decrease of indium content. The absolute change of the resistivity may also be caused by the change of Zn and Mg composition as well as the crystalline quality.

The carrier concentration of the c-MZO:In thin films is evaluated by Hall measurement. In Fig. 4.19, the negatively charged carrier concentration increases with indium dopant content. As it has been proved that the substitution of In into the Zn site substantially enhances the conductivity of the film. Moreover, we have demonstrated that In doped MgO thin film shows a much poorer electrical conduction than those of ZnInO thin film. Therefore, we believe that the resistivity improvement mainly comes from the In substitution into Zn site by donating free electron carriers to the c-MZO system though it is possible that In substitutes Mg sites. The carrier concentration of the samples changes from 1.47×10^{18} cm^{-3} to 8.22×10^{19} cm^{-3}, a respectable and useful value for a semiconducting oxide material.

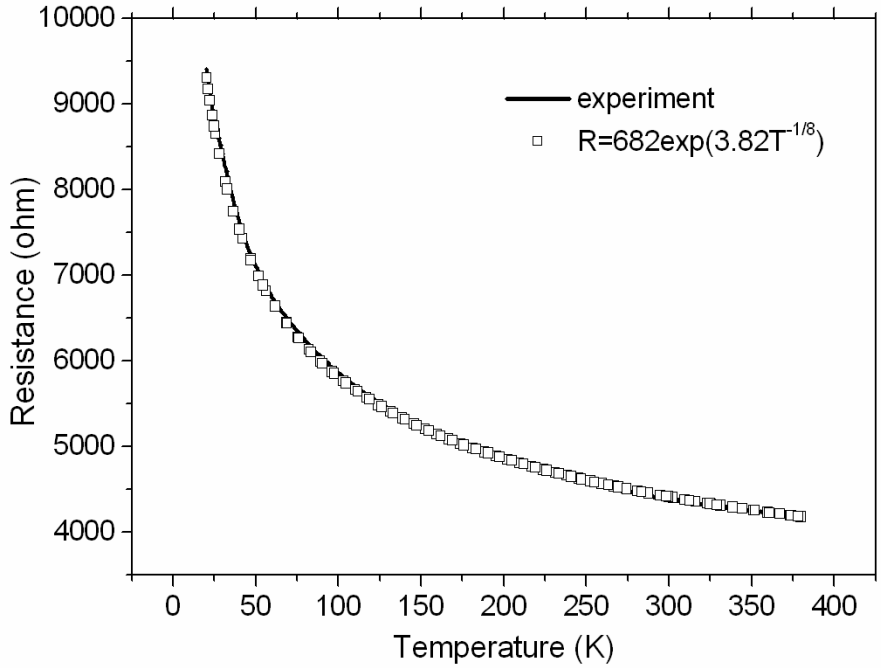

Figure 4.15 The comparison of $R \propto T^{-1/8}$ equation and the experimental result.

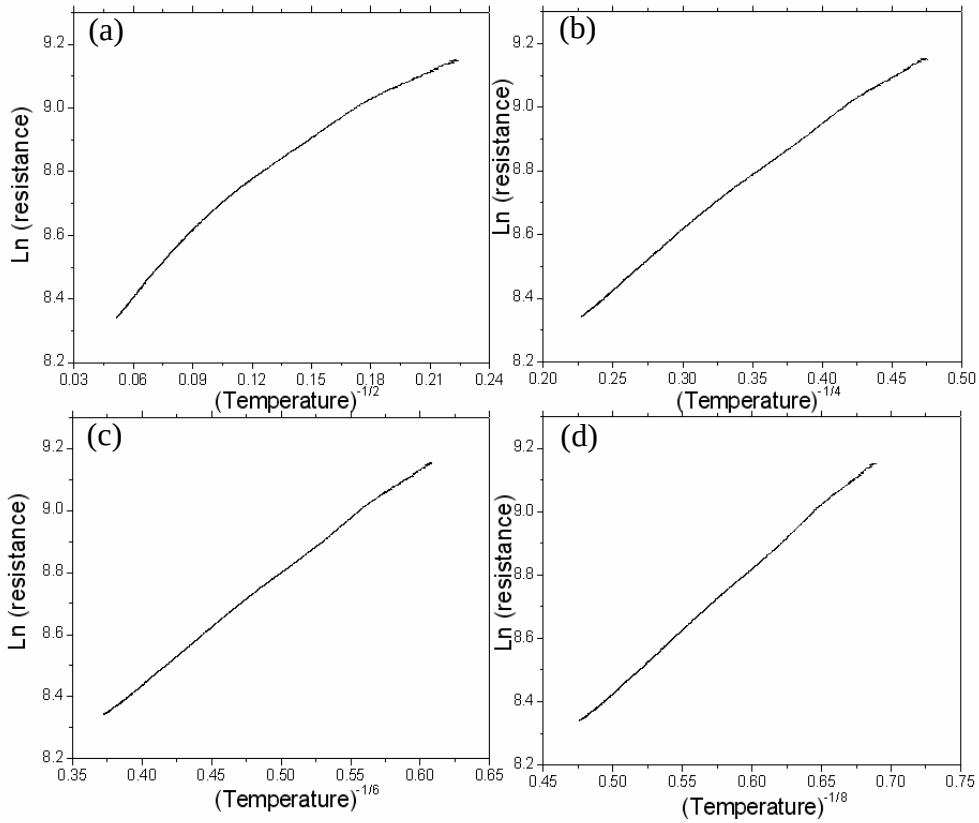

Figure 4.16 The Ln-plot of resistance against (a) $T^{-1/2}$, (b)$T^{-1/4}$, (c)$T^{-1/6}$, (d)$T^{-1/8}$

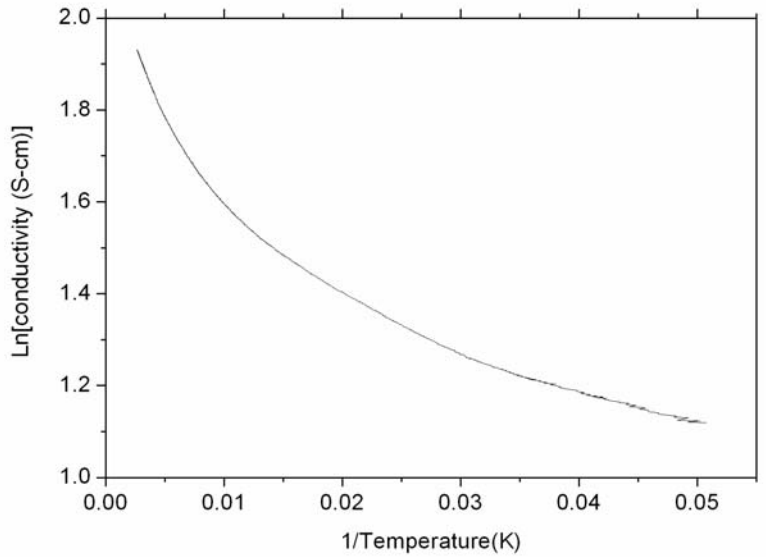

Figure 4.17. The Ln-plot of conductivity against 1/Temperature.

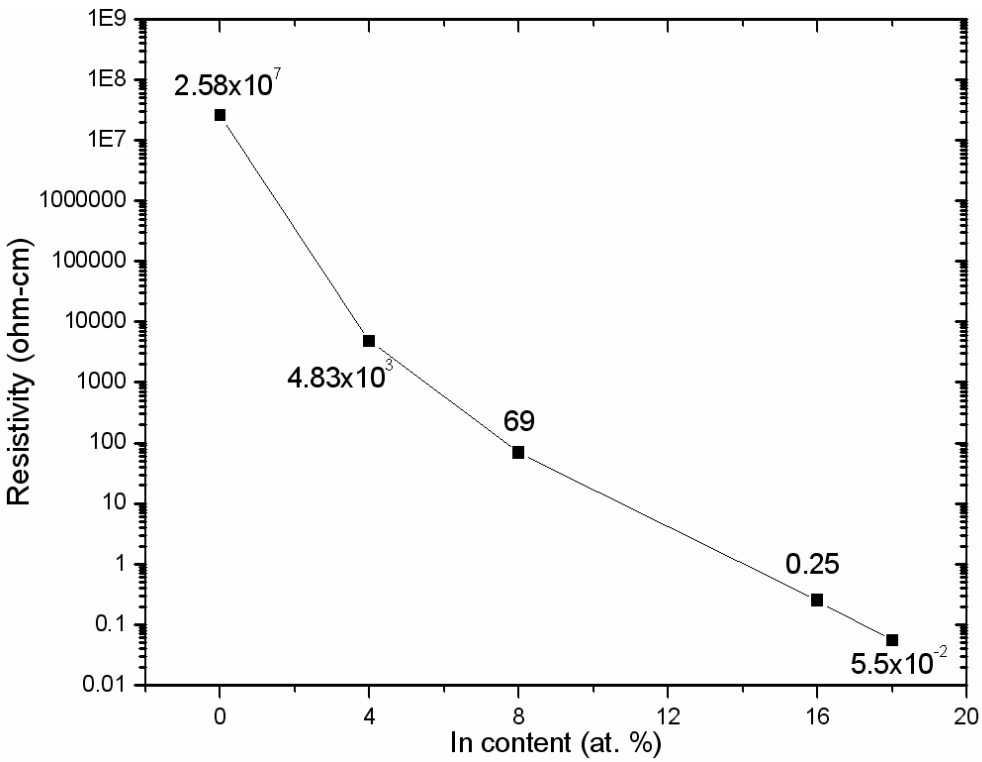

Figure 4.18 Resistivity of c-MZO aginst indium content

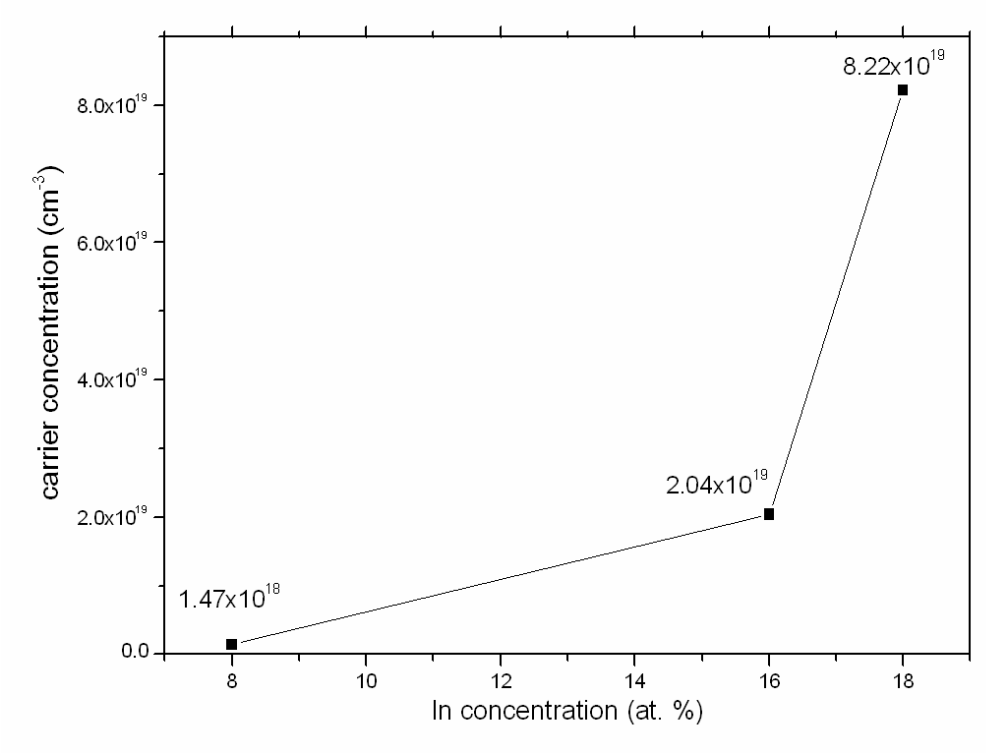

Figure 4.19 Carrier concentration of c-MZO against indium content

4.3.4 Optical characterizations

Fig. 4.20 shows the optical transmittance profile of the c-MZO thin films with indium concentration of 4, 8, 16 and 18 at %. All films are fabricated on MgO substrates with polished surfaces. The photo spectrometer automatically subtracts the transmittance of the substrate from the reference. The deposited films have transmittance over 80% in the visible spectrum, meaning not only good transparent property of the c-MZO:In film is fabricated, but also that the introduction of indium does not down grade the transparency of the c-MZO film. In terms of the band gap energy, transmittance profile reveals a red shift on the band edge with the concentration of In. The deduced band gap energies of 4, 8, 16, and 18 at. % In doped samples are 5.6, 4.4, 4.3 and 4.1eV respectively. It is clearly seen that the indium content in c-MZO lowers the band gap energy. This is likely due to the smaller band gap energy of In_2O_3

with respect to MgO. When the ratio of In to Mg increases, the resultant band gap energy drops. XRD profiles show no signal of In_2O_3. We are not sure the existence of the In_2O_3 cluster. The change of the band gap energy may due to the combination of In substituting in the Mg sites, In substituting in Zn sites, In substituting in c-MZO system and In_2O_3 clustering. If the above mentioned mechanisms do present, the transmittance of the sample will not be a simple single sharp edge. However, only one sharp edge is observed so it is likely that In substituting in c-MZO dominates the whole system

Fig. 4.21 is the graphs of $(\alpha h\nu)^2$ against photon energy, where α denotes the absorption coefficient and $h\nu$ denotes the photon energy. This is a well established method to deduce the direct band gap of the material. From the result obtained, a nearly constant slope can be plotted in the range of the absorption band edge. This is consistent with the direct band gap model.

In Fig. 4.22, the refractive index of the c-MZO:In is deduced from measurements by the prism-coupling technique. The eventual calculated value is 1.86. This is close to the refractive index of pure MgO of 1.74.

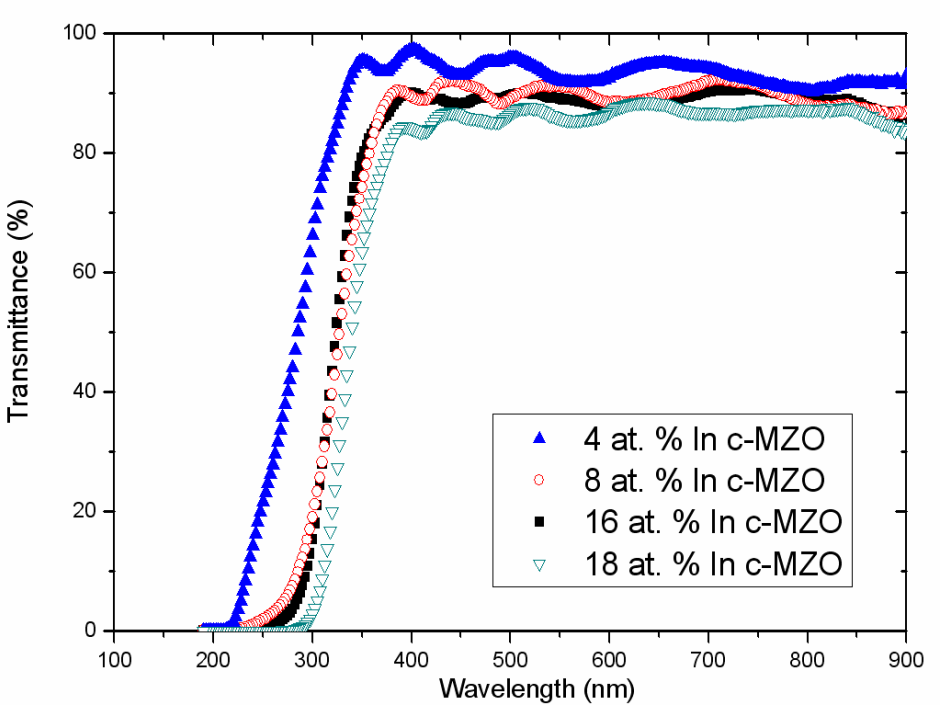

Figure 4.20 Transmittance profiles of c-MZO against indium content

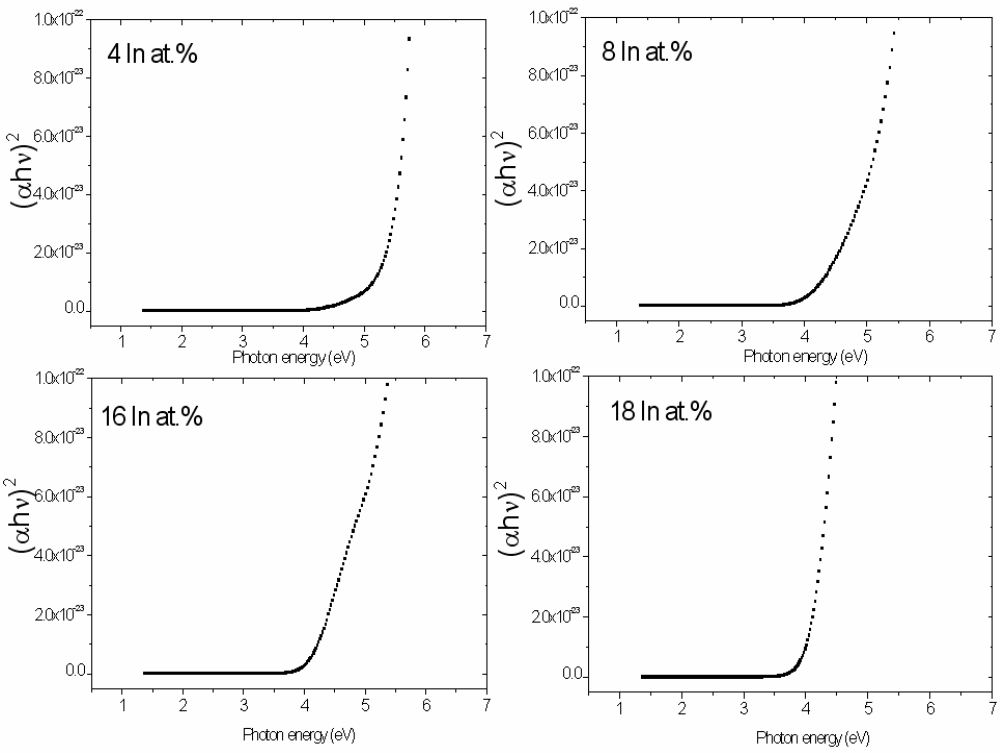

Figure 4.21 The plots of $(\alpha h\nu)^2$ against photon energy with different indium content

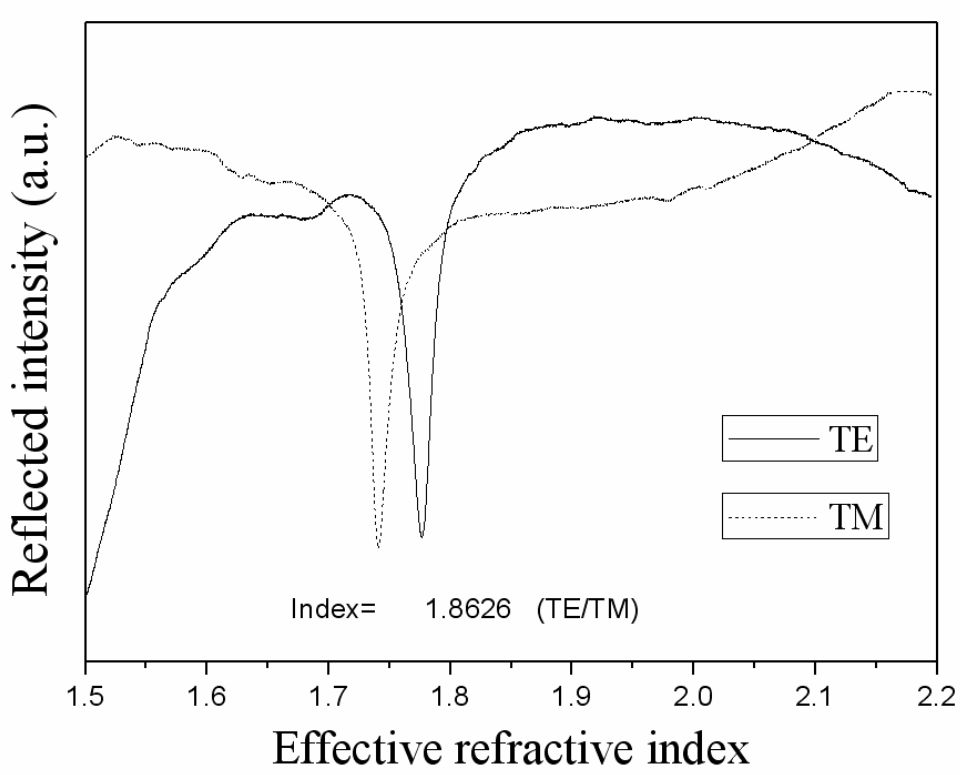

Figure 4.22 The refractive index of c-MZO:In by prism-coupling technique.

4.4 Phase characterization of In-doped c-MZO thin films against substrate temperatures

4.4.1 Phase characterization

Beside the doping concentration, substrate temperature during film growth is another crucial factor that affects the physical properties of the film. Fig. 4.23 shows the XRD patterns of 16 at % c-MZO:In films prepared under different substrate temperatures. As the film growth temperature is set from 300°C to 600°C, single c-MZO:In phase is obtained. That is, this structure can be easily fabricated under a relatively low temperature. When the substrate temperature is increased, the Bragg's diffraction shifts to the right, suggesting a reduced lattice constant. The reason may come from the loss of Zn content in the film which has been discussed in section 1.3. As the Zn is desorbed, the Zn/Mg ratio drops. Since Mg^{2+}(0.78 Å) has an ionic radius smaller than that of Zn^{2+}(0.83 Å), the lattice constant of the unit cell decreases. The lattice constant against substrate temperature is summarized as Fig. 4.24.

Substrate temperature has predominant effect on the crystallinity of the film. The omega-scan XRD profiles of the films grown at different substrate temperatures are shown in Fig. 4.25. Evidently, higher substrate temperature exhibits poor crystalline properties. This is in direct contradiction to the conventional wisdom of "better crystalline structure at higher temperature". The reason of this unusual characteristic is probable due to the increase of In content in the films at high temperature (caused by excessive loss of Zn and Mg), leading to the poor crystalline structures. For pure c-MZO thin films on LAO substrates system, Fig. 4.26 and 4.27 reveal the diffraction

peaks shift and the crystalline quality becomes better at higher substrate temperature. This illustrates that In is the cause of the “bad” crystallinity at high deposition temperature

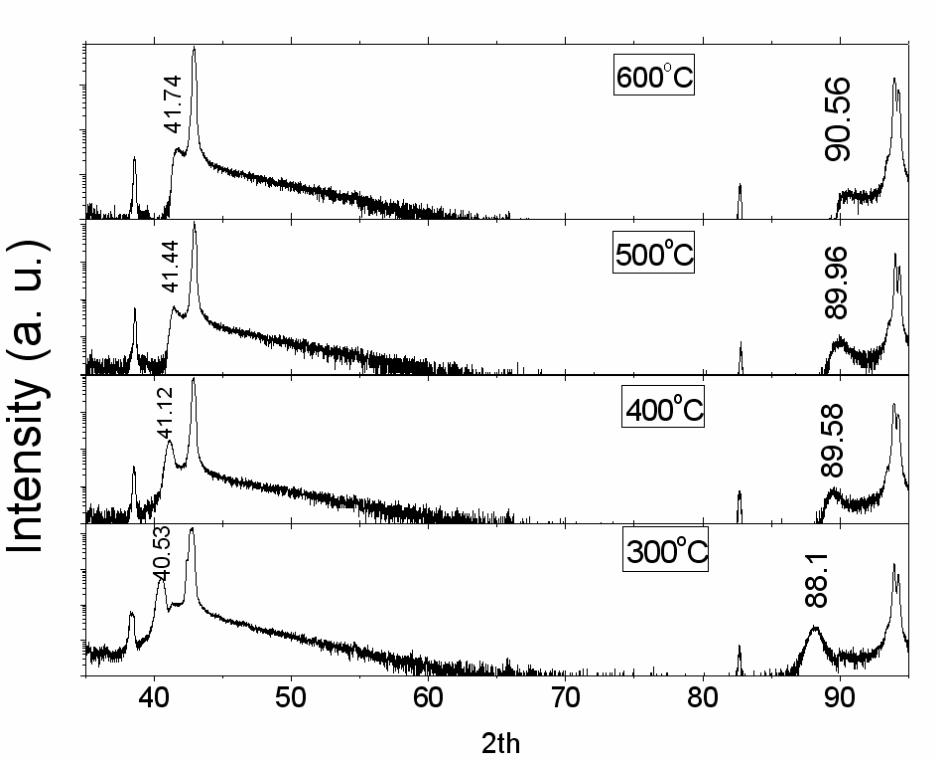

Figure 4.23 XRD θ-2θ scans of 16 at.% c-MZO:In against substrate temperature

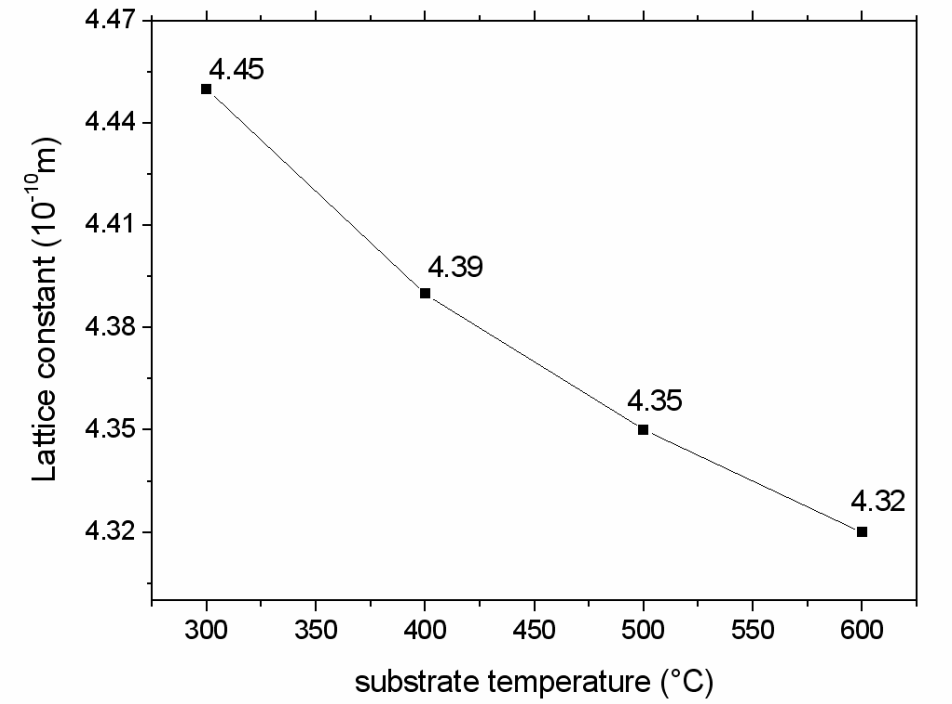

Figure 4.24 Lattice constants of 16 at % c-MZO:In against substrate temperature

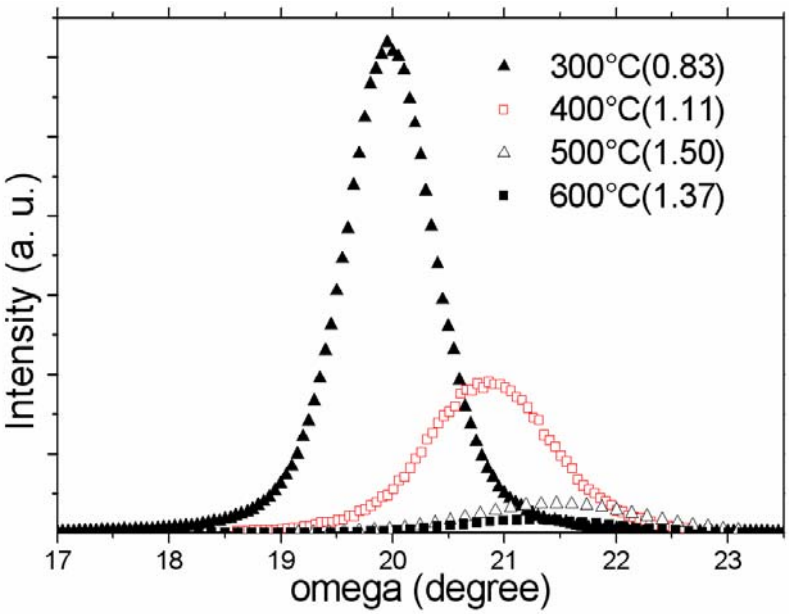

Figure 4.25 XRD ω scan of 16 at % c-MZO:In (0 0 2) diffraction plane against substrate temperature

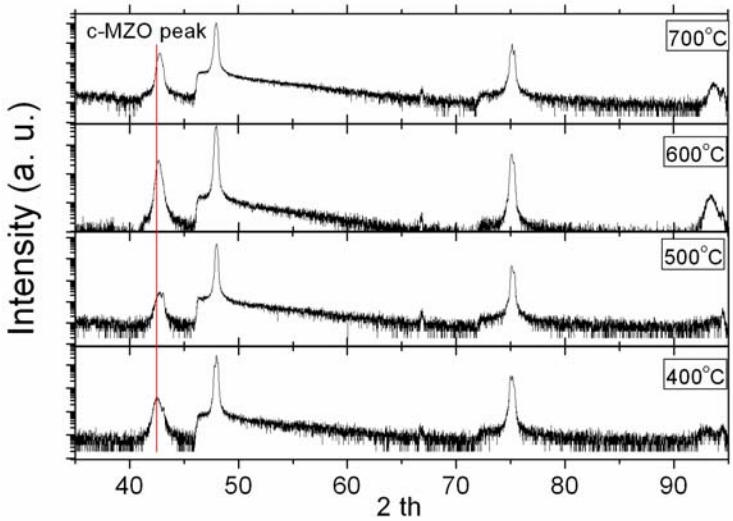

Figure 4.26 XRD θ-2θ scans of pure c-MZO against substrate temperature

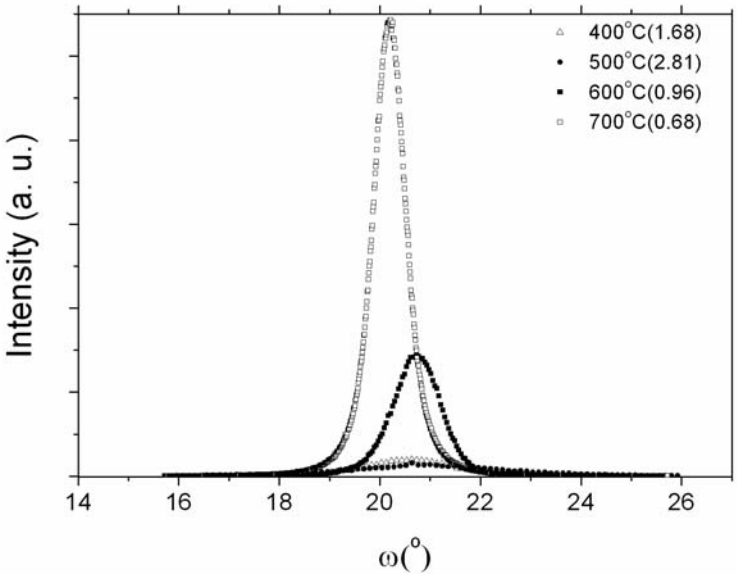

Figure 4.27 XRD ω scan of pure c-MZO (0 0 2) diffraction plane against substrate temperature

4.4.2 Surface morphologies

Fig. 4.28 shows the SEM pictures of the 18 at. % c-MZO:In thin films deposited on (0 0 1) MgO substrates at various growth temperature. At 300ºC, some ball-like grains of a few nano-meters size are uniformly distributed on the film surface. At 500 ºC, the ball-like grains disappear. Instead, the film with some holes and cracks are seen. When the temperature is increased to 600 ºC and 700 ºC, the morphology of the films is improved and relatively smooth and clean surface is seen.

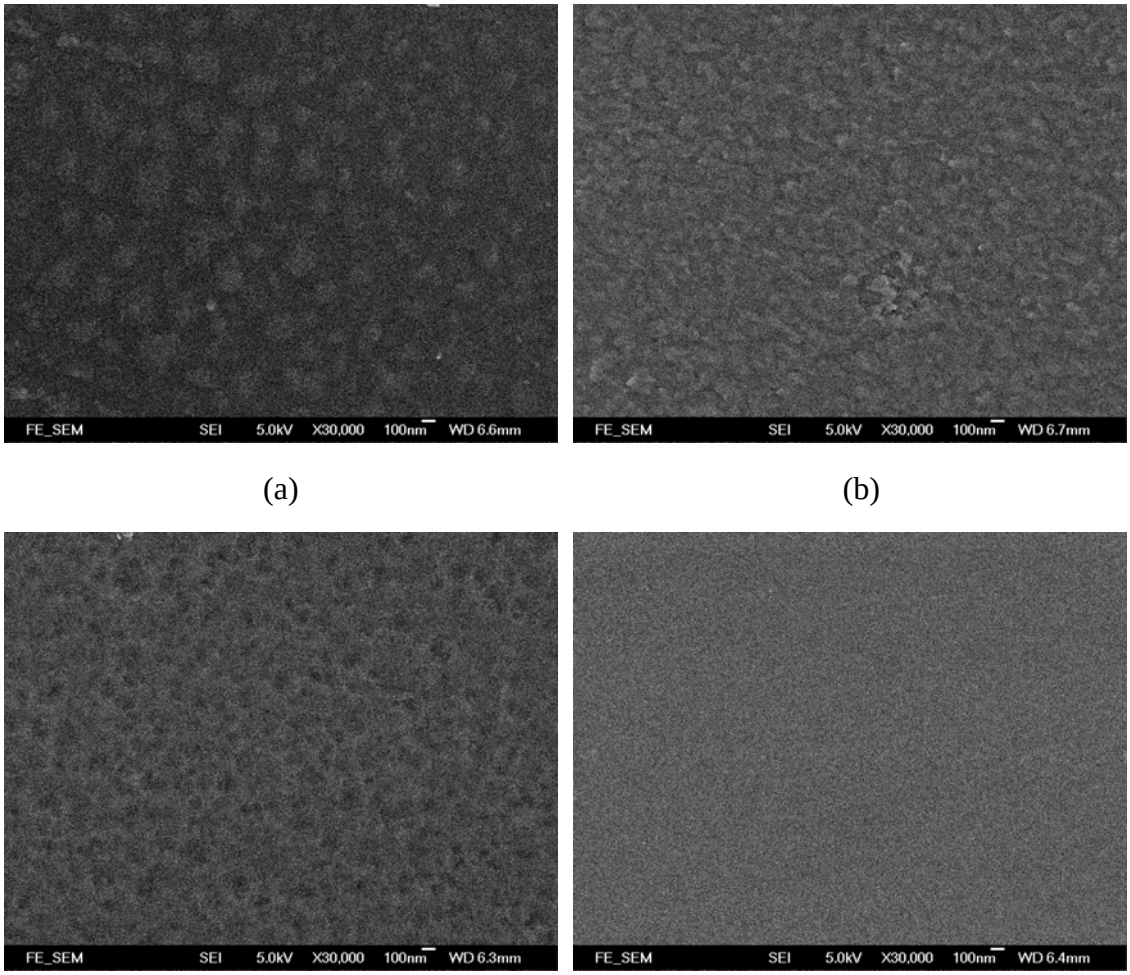

(a) (b)

(c) (d)

Figure 4.28 The SEM images of 18 at. % c-MZO:In at substrate temperatures (a)300˚C, (b)500˚C, (c)600˚C, (d)700˚C.

4.4.3 Electrical characterizations

In this section, we discuss the relationship between the electrical property and the deposition temperature, neglecting the influence the composition change in the films. It is no doubt that the substrate temperature influences the electrical conduction of the film as the crystalline quality of c-MZO and impurity substitution in the c-MZO unit cell generating free negative carriers are all being affected. Fig. 4.29 shows the relation of

the resistivity of the c-MZO:In films against the deposition temperature fabricated from 16 at. % c-MZO:In target. At 300 ºC and 400ºC, the resistivity is about several MΩcm, its value is similar to the pure c-MZO film which is deposited at 600 ºC. It is believed that the indium dopant does not have sufficient thermal energy to substitute in the c-MZO site. Instead, interstitial of indium oxide may occur, in which no extra free carriers are generated. At 500 ºC and 600 ºC, the resistivity significantly drops to 2.86 and 0.25Ωcm respectively. The critical change of the resistivity comes about between 400 ºC and 500 ºC.

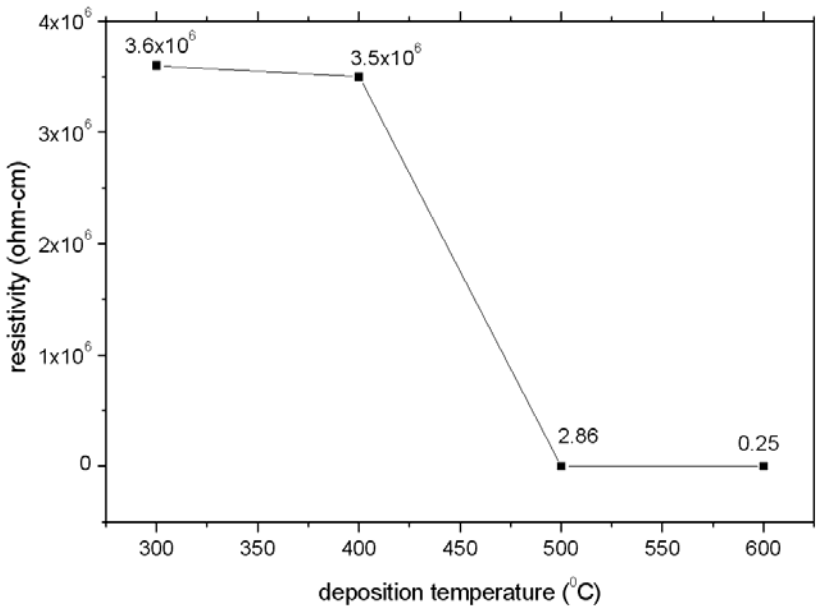

Figure 4.29 Resistivity of 16 at. % c-MZO:In films against substrate temperature.

4.4.4 Optical characterizations

In the XPS analysis, it is revealed that the composition of the c-MZO:In films changes under high substrate temperature because of the vapor pressure difference of the constituent elements. Consequently the composition variation alters the band gap

energy, hence the spectrum of transmittance. In Fig. 4.30, the transmittance profiles of 16 at. % In doped c-MZO thin films are measured. When increasing the substrate temperature, the absorption edge shift to left, indicating the band gap energy of the c-MZO:In film becomes larger with the temperature. Based on the result of the XPS, Zn content is evaporated away at high temperature with low pressure, the Mg/(Zn+In) ratio increases, the Mg content dominates in the c-MZO system, leads to the resultant band gap increase. Overall, the films deposited at the temperature range from 300˚C to 700˚C are transparent to the visible spectrum.

The transmittance profile reveals that all c-MZO:In films have good optical transparency. Apart from being a large band gap material, the c-MZO:In grows easily at temperature between 300˚C and 700˚C to form excellent crystalline films. The photon absorption and scattering by grains are therefore minimized. Still, it can be seen that the transmittance is better at higher deposition temperature. The transmittance of the film grown at 700˚C is over 90%. Those deposited at 300˚C, however, yield a transmittance of no less than 80%.

In Fig. 4.31, the plots of $(\alpha h\nu)^2$ against photon energy are made. Films of c-MZO:In deposited at 300˚C appear to be direct band gap with gap energy of ~4.2 eV. For films deposited at the temperature from 400˚C to 700˚C the plots look more complicated and there might be more than one energy state existed.

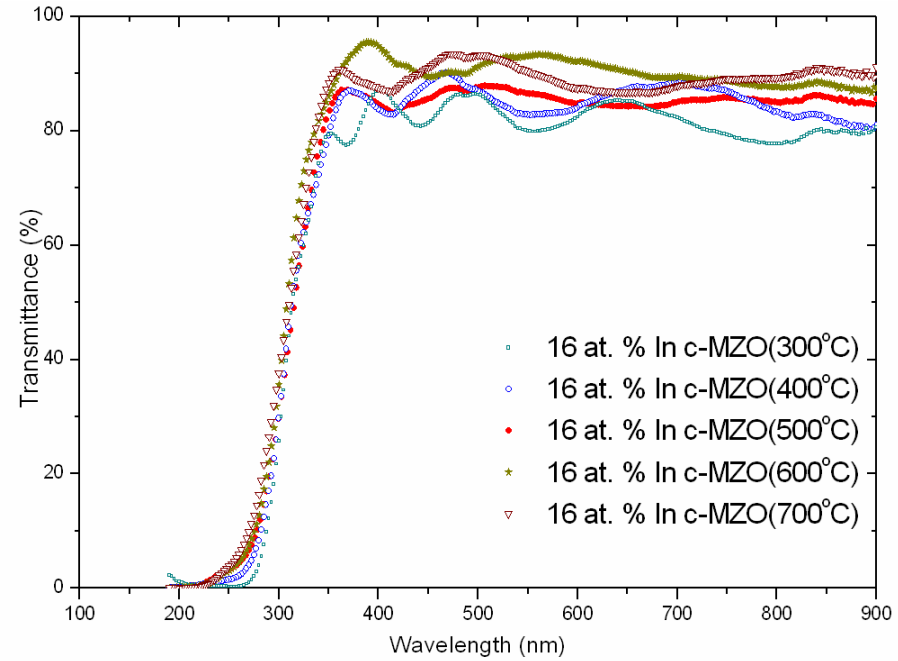

Figure 4.30 Transmittance profiles of 16 at. % c-MZO:In film against substrate temperature.

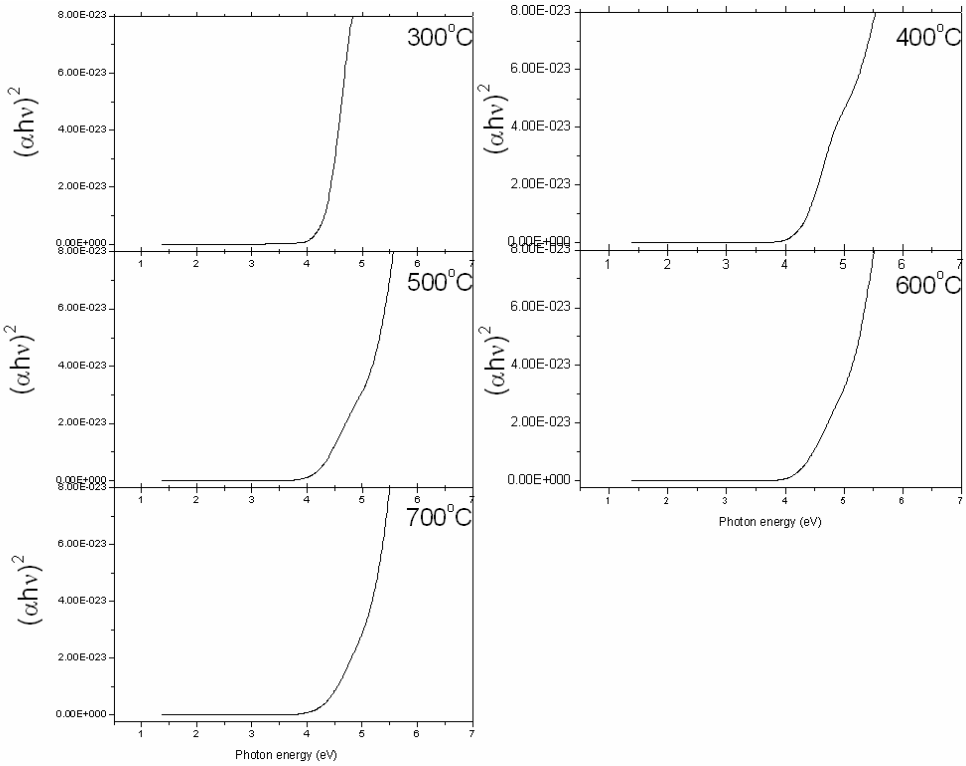

Figure 4.31 The plot of $(\alpha h\nu)^2$ against photon energy of 16 at. % c-MZO:In film with different substrate temperature.

4.5 Optimal deposition condition of c-MZO:In thin films

The above results describe the film properties and how they are affected by different processing conditions. Among all c-MZO:In thin films deposited, a better crystalline can be obtained with low indium content and at low growth temperature. On the other hand, the conductivity can be improved by depositing the film at high temperature with more In dopant. Based on the structural, electrical and optical considerations, we prefer to deposit the films at high substrate temperature with relatively high indium content. Thus, in the latter experiments, we attempt to deposit the 18 at % of In doped c-MZO:In thin film at 600ºC. The resistivity of such films is about 0.055Ωcm. The lattice constant is 4.36Å with the FWHM of the rocking curve of about 1.91º. The band gap energy is about 4.1eV, which is over the visible spectrum.

Chapter 5

Fabrication and characterization of indium doped c-MZO/LNO p-n heterojunction on LAO and MgO substrates

5.1 Introduction of all oxide p-n junction

p-n junction is the basic unit of modern electronic application. Instead of typical extrinsic silicon semiconductor, p- and n- types of semiconducting oxides can also be use to fabricate p-n diode junction. The advantages of oxide semiconductors are multitudinous. They include high operating temperature [5-1], optical transparency [5-2] and magnetic properties [5-3], [5-4], and widely tunable band gap energy [5-5], [5-6], [5-7], [5-8], [5-9], [5-10], [5-11], [5-12], [5-13], [5-14], [5-15] etc. Indeed, utilizing large band gap oxide semiconducting of n- type ZnO and p- type LiNiO (LNO), optically transparent all-oxide p-n junction is fabricated. It is proposed that the transparent p-n junctions can be used as photo-diodes. Their applications such as UV detector or transparent bipolar junction in display technology are envisaged.

In this chapter, we briefly describe the working mechanism of the p-n junction using the partial energy band diagram. The geometry of an all oxide p-n junction is discussed. The fabrication details of c-MZO and LNO bilayer structure are presented. The phases and epitaxial relation of this heterostructure are characterized. Then the

current-voltage profile and optical transmittance of the diode junction are measured and evaluated.

5.1.1 The working mechanism of all-oxide p-n junction

The working principle of silicon-based p-n junction can be applied equally well to describe the all-oxide p-n junction as the concept in both cases are very similar. It is known that for n-type semiconductor, the Fermi energy level is near the conduction edge with donor density N_d whereas p-type semiconductor has the Fermi level near the valence edge with acceptor density N_a. Both types are assumed as uniformly doped.

When two layers are merged together, the negative carriers in n layer and positive carriers in p layer diffuse and recombine each other at the junction interface, leaving the ionized donors and acceptors in both layers respectively. These ions induce an internal electric field across the junction and deplete the mobile charge carriers there. The length of this depleted region is called the depletion width. Within the depletion width, the internal electric field causes the charged carriers to drift in the opposite direction. In equilibrium condition, the drift current density and the diffusion current density are balanced, and no net current flows through the junction. From the energy band diagram, if there is no external voltage applied to the p-n junction, the Fermi energy levels of n-type and p-type are aligned, and the voltage drops across the depletion region under equilibrium condition is known as the build-in voltage. Fig. 5.1 shows the p-n junction formation illustrating the corresponding energy band structure [S. M. Sze 1981][5-16]

In considering the applied biased potential and the energy band diagram, we can

explain the non-linear current-voltage characteristic quite satisfactorily. When a forward bias is applied to the junction, meaning that the positive pole is connected to the p layer, the difference between the Fermi energy level in the n-type and p-type quasi-neutral region decreases. This is shown schematically in Fig. 5.2. According to the carrier density distribution, the electrons (from n-type material) and holes (from p-type material) can pass through the junction easily, and the current increases exponentially.

In the reversed biased case, the potential across the junction increases and so does the depletion width. The potential barrier inhibits the mobile carriers to travel across, so only a small leakage current passes through [Robert F. Pierret, 1996][5-17]

The non-linear current-voltage characteristic of p-n junction is given as the equation, $I = I_o(e^{\frac{qV_A}{kT}} - 1)$, where I_o is the saturated current, q is electron charge, V_A is the applied voltage, k is Boltzmann constant and T is junction temperature. From the equation, when $e^{\frac{qV_A}{kT}} << 1$ or V_A<0, the current is equal to -I_o which is extremely small. At the time V_A beyond the turn-on voltage, the current increases exponentially. The current also depends on the sample temperature. The amounts of free carriers are created by the thermal excitation at high temperature. Therefore, it can be expected that when the sample temperature increases, the change of current against voltage is increased and vice versa. In the following sections, we mainly focus on the relation between the current against the applied voltage and the sample temperature.

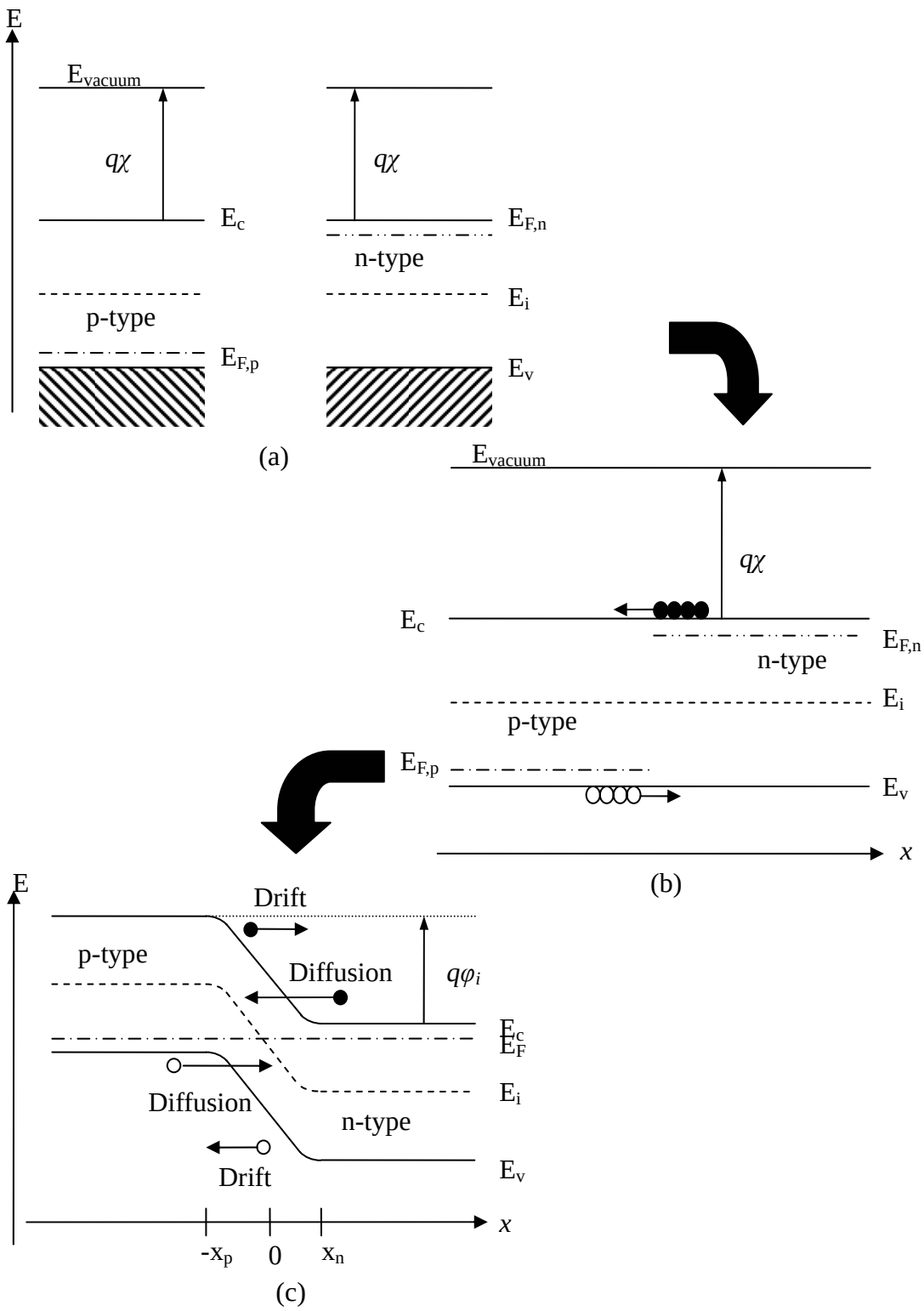

Figure 5.1 Energy band diagrams of a p-n junction (a) before, (b) after merging the n-type and p-type regions and (c) in thermal equilibrium

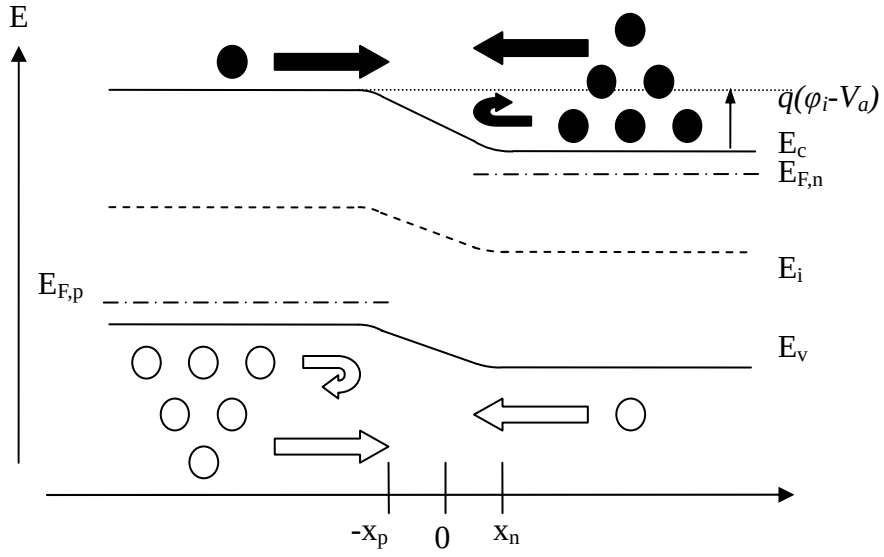

Forward biased

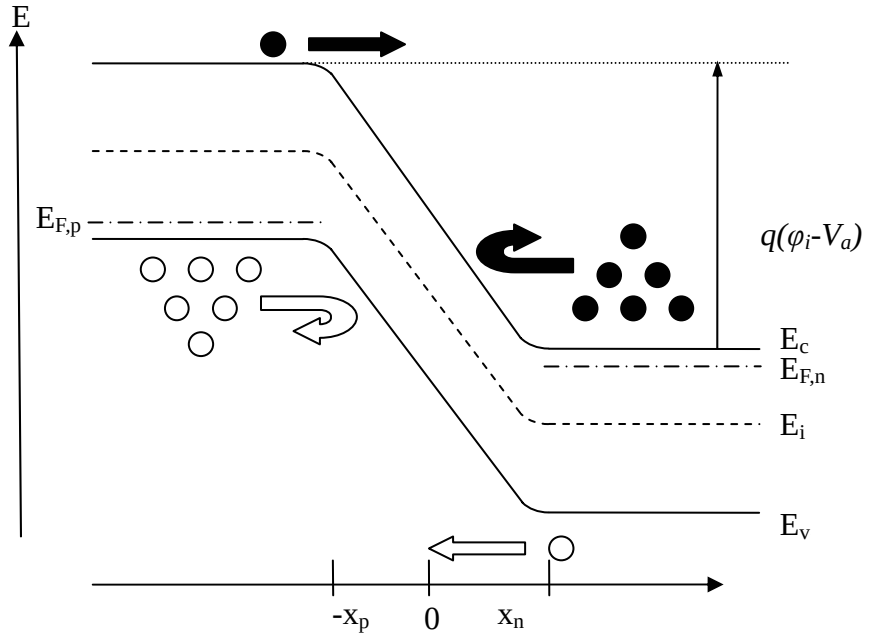

Reversed biased

Figure 5.2 Energy band diagrams of a p-n junction under (a) forward biased and (b) reversed biased.

5.2 Structural measurements of c-MZO:In/LNO p-n heterojunction

5.2.1 Structural characterization of LNO target

Intrinsic NiO thin film is highly insulating and transparent with p-type conduction [5-18], [5-19]. The employment of Lithium (Li) can enhance the conductivity but lower the transparency of the material. The lattice constant of LiNiO (LNO) is about 4.17Å according to the content of Li. With the transparent property, LNO is an excellent p-type material for fabricating transparent p-n junction.

LNO target is prepared by using Li_2CO_3 and NiO powders. The amount of Li_2CO_3 and NiO used are 0.831g and 9.524g respectively. The powders were first mixed by ball milling for at least 6 hours. Then the mixture was calcinated twice at 1100˚C and 1200˚C for 10 hours each in air. The treated powder is pressed into a 2.5cm circular disc at room temperature and then sintered at 1350˚C for 10 hours in air. The powder diffraction pattern of the LNO target is shown in Fig. 5.3.

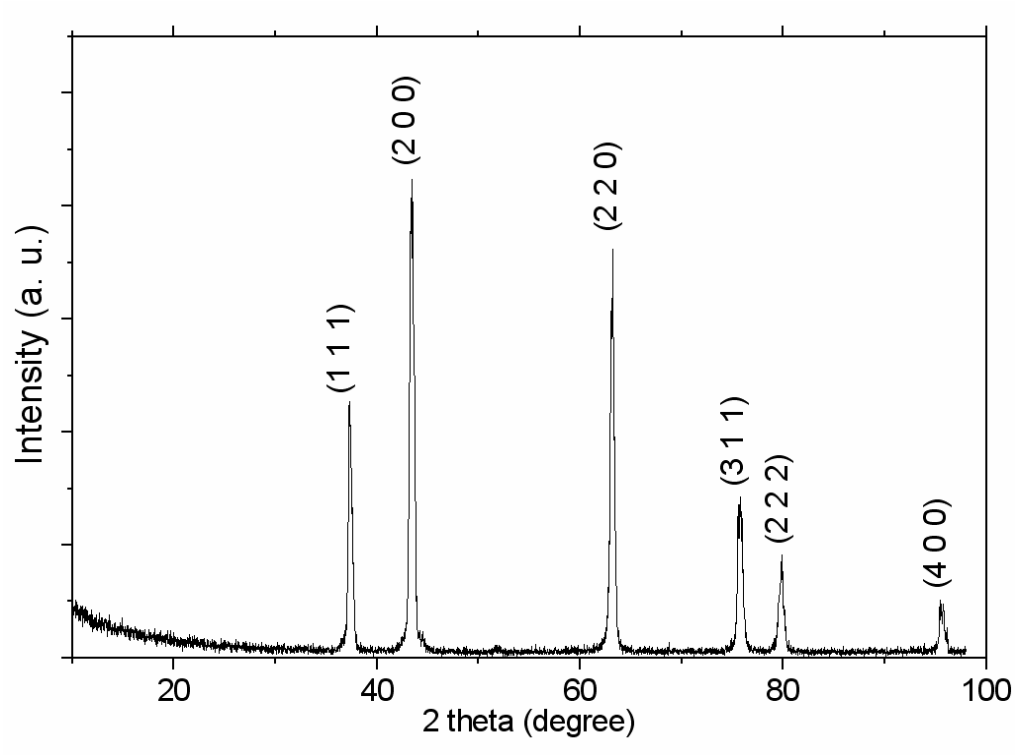

Figure 5.3 XRD powder diffraction of LNO target

5.2.2 Deposition of LNO thin films on MgO substrate

The p-type LNO thin films were deposited on MgO substrate. They were grown at different substrate temperatures at 550˚C and 600˚C. The oxygen ambient pressure during deposition was regulated at 100mTorr to 150mTorr. The fine variation of the gas pressure appears to affect the transparency and the conductivity of thin films. For pure NiO film, it is highly transparent but electrically insulating. The introduction of Li improves its conduction but lower the transparency. At high substrate temperature, Li in the LNO film tends to evaporate from the film. This leads to better transparency at the expenses of lower conductivity. The low oxygen ambient pressure also helps the substitution of Li in NiO film. The deposition time of the LNO films is 20minutes followed by 15 minutes post-annealing. The thickness of LNO film fabricated from my

group mate with similar condition was about 80nm.

5.2.3 Structural characterization of LNO thin films

Fig. 5.4 shows the θ-2θ scan of LNO thin film grown on MgO (0 0 1) substrate. The single cubic phase of LNO peaks are observed. The lattice constant is about 4.18Å. Lattice mismatch with the MgO substrate is less than 2 %. The omega scan shown in Fig. 5.5 reveals that the rocking curve of LNO films is about 0.42˚. LNO epitaxially grown on MgO substrate is verified from the 360˚ phi-scans in Fig. 5.6.

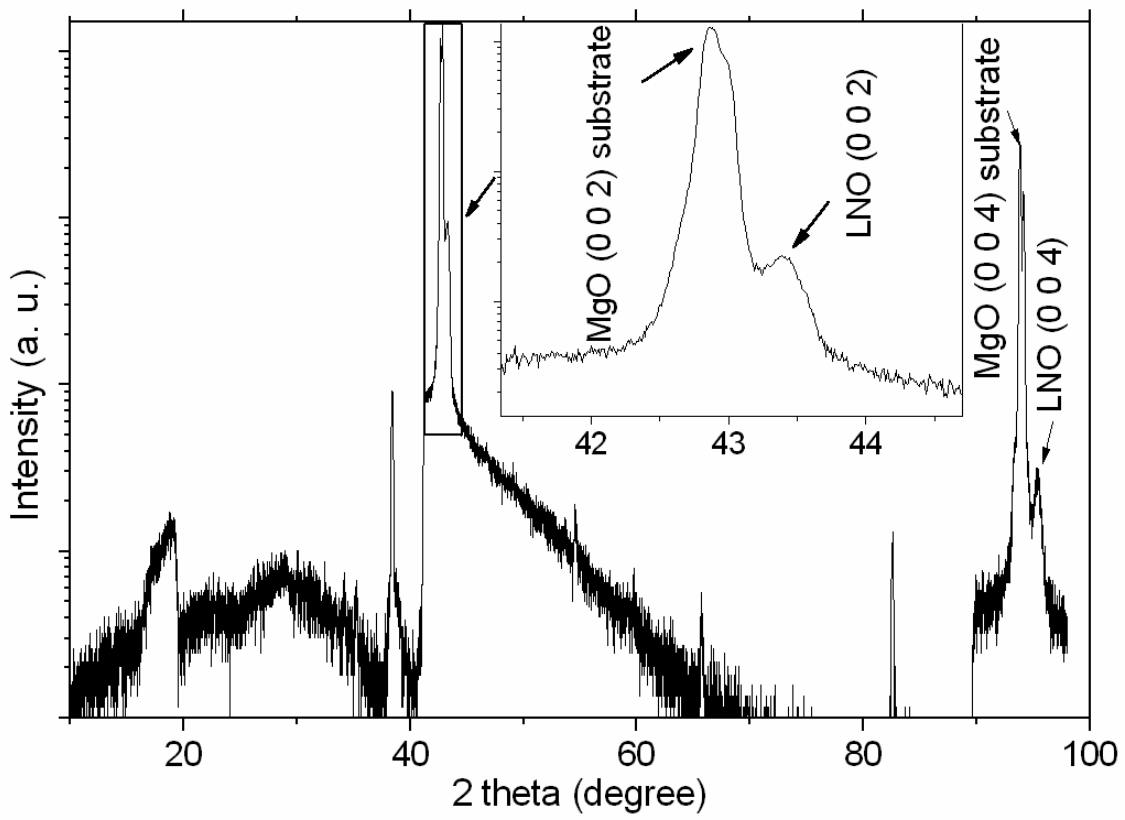

Figure 5.4 XRD θ-2θ scan of LNO thin film on MgO (0 0 1) substrate.

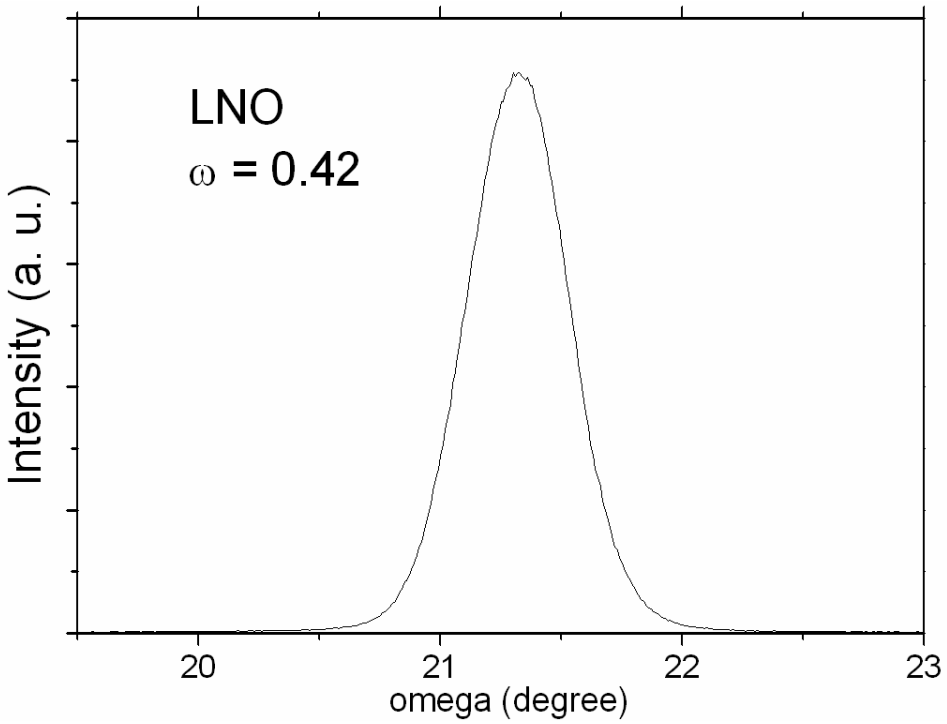

Figure 5.5 XRD ω scan of LNO (0 0 2) diffraction plane on MgO (0 0 1) substrate

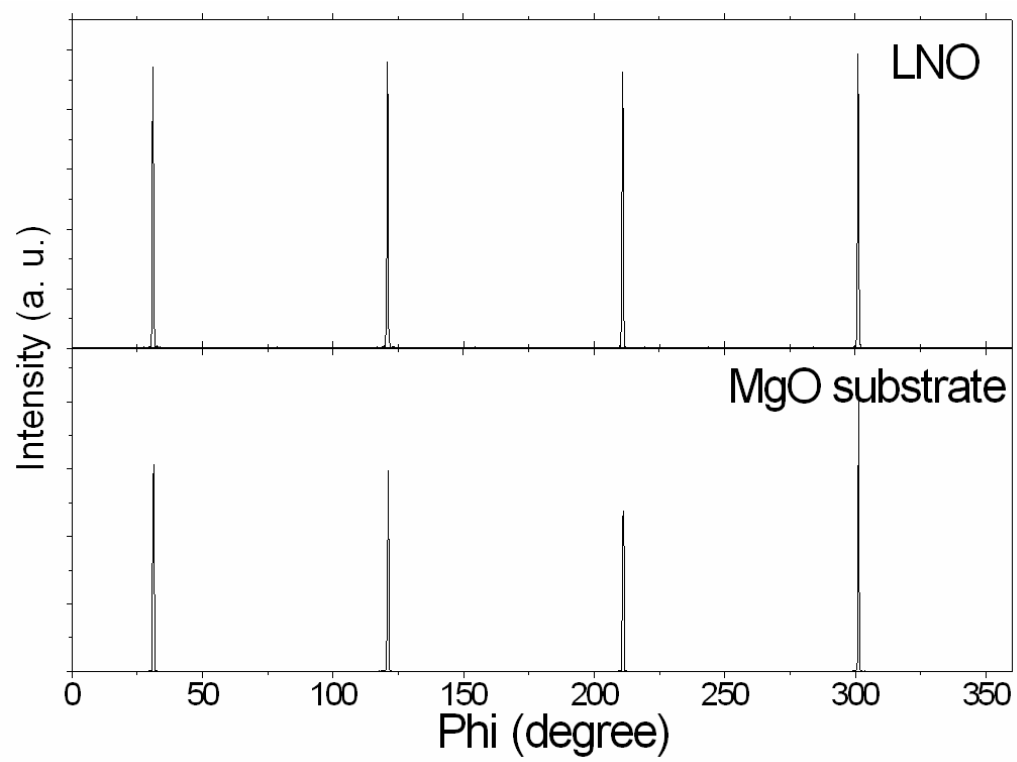

Figure 5.6 XRD 360˚ phi-scans of LNO on MgO (0 0 1) substrate

5.2.4 Structural characterization of c-MZO:In/LNO bi-layer structure

We have demonstrated epitaxial growth of LNO thin film on MgO substrate. In previous chapter, epitaxial c-MZO:In thin films fabricated on MgO and LAO substrates were reported. Thus, it is believed that heteroepitaxial c-MZO:In/LNO p-n junction can be fabricated on both substrates, especially if we deposit c-MZO:In layer first on the substrate and then LNO on top of the c-MZO:In layer.

The deposition processes of the p-n junction were no more complicated than those of single oxide layer. First of all, the c-MZO:In n-type layer was deposited on the (0 0 1) MgO or LAO substrate under the optimal condition. Then a stainless steel mask with regular array of holes of 500 μm×500μm square was positioned to cover the n-type layer surface. LNO p-type layer was then deposited, so that square LNO islands on the top of the n layer were produced, the separation between the square islands is roughly equal to 1.5mm, we assume that the area of the LNO is about 0.0025cm^2, same as the square mask. Finally, we aligned another mask having circular holes of 200μm diameter on the LNO surface. Subsequent PLD of Pt therefore produced spot electrodes for junction measurements. The schematic diagram of the p-n junction is shown in Fig. 5.7. The electric conduction path between the two electrodes is comparatively long. As the resistivity of the c-MZO:In is about 10^{-2} Ωcm, part of the potential is dropped along the n layer. The measured applied voltage will be larger than the potential drop across the junction interface.

The crystalline phases of the p-n junction deposited on MgO and LAO substrates were characterized by XRD. Fig. 5.8 and 5.11 show the θ-2θ scans of the films with

substrates. Apparently single cubic phase exists in all films. From the graphs, the lattice constants of all films can be evaluated. For LNO/c-MZO:In/LAO heterostructure, the lattice constants of LNO, c-MZO and LAO are 4.17Å, 4.32 Å and 3.79 Å, respectively. For LNO/c-MZO:In/MgO the lattice constants of LNO, c-MZO and MgO are 4.16Å, 4.36 Å and 4.21 Å, respectively. The lattice change of the n layer can be attributed to the internal strain from the substrate. The lattice mismatches between the n and p layers are no more than 5%. The induced stress is thus expected small. Fig. 5.9 and 5.12 show the omega scans of the two layers. The FWHM of rocking curve of the n-type (0 0 2) c-MZO:In diffraction peak is about 1.25˚ for films grown on MgO and 2.26˚ for those deposited on LAO. The corresponding p-type (0 0 2) LNO films reveal FWHM rocking curves of 0.81˚ and 2.02˚. The 360˚ phi-scans profiles of the p-n junctions are depicted in Fig. 5.10 and 5.13. These results match well to those reported in the previous chapter. For example, the c-MZO:In is 45˚ in-plane twisted grown on LAO and is cube-on-cube epitaxially grown on MgO substrates. Moreover, the LNO p-layers grow epitaxially on the c-MZO:In n-layers. The epitaxial relation helps minimizing the electron scattering and increasing the efficiency of electrons transportation at the interface. Consequently the I-V characteristic of the junction can be improved.

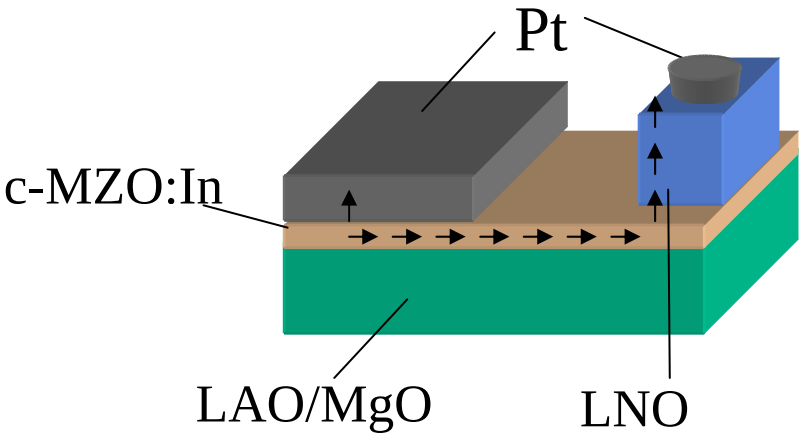

Figure 5.7 The schematic structure of c-MZO:In/LNO heterojunction on LAO/MgO substrate.

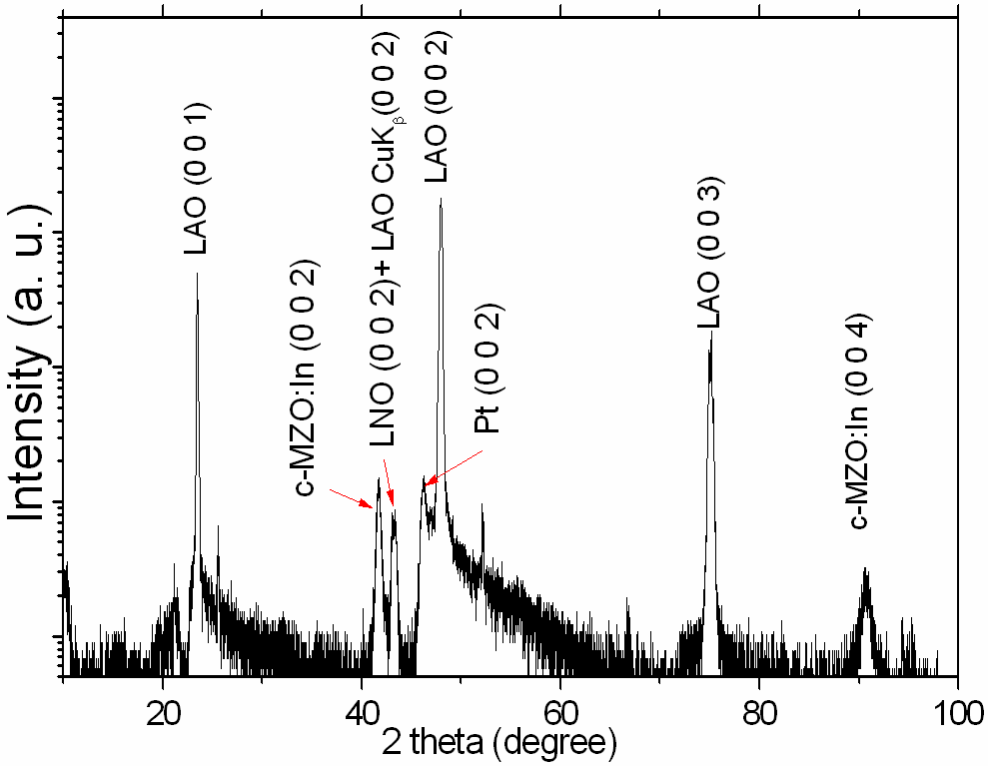

Figure 5.8 XRD θ-2θ scan of c-MZO:In/LNO heterojunction on LAO (0 0 1) substrate

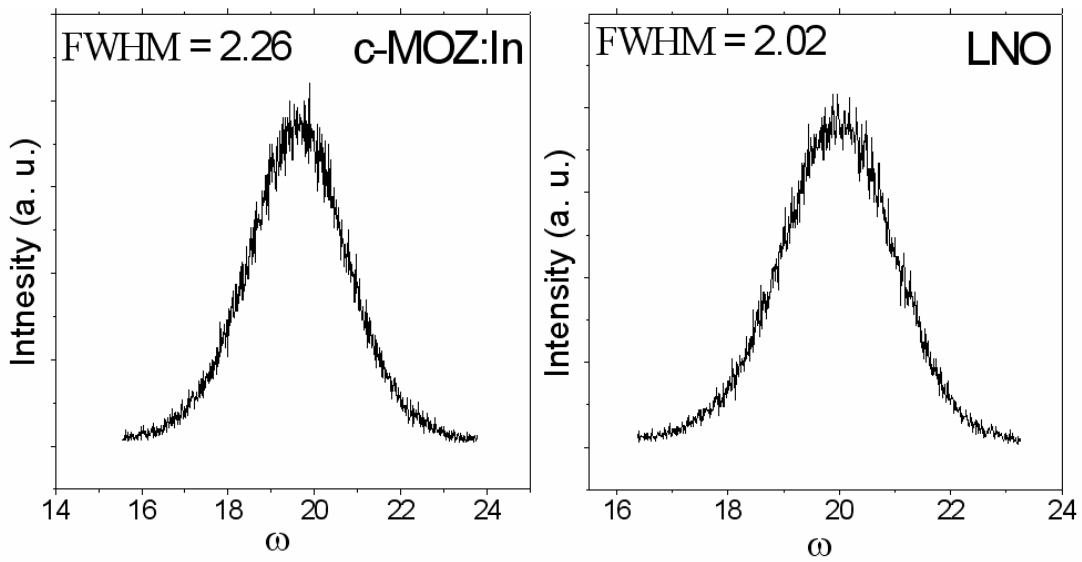

Figure 5.9 XRD ω scans of c-MZO:In/LNO (0 0 2) diffraction planes heterojunction on LAO (0 0 1) substrate

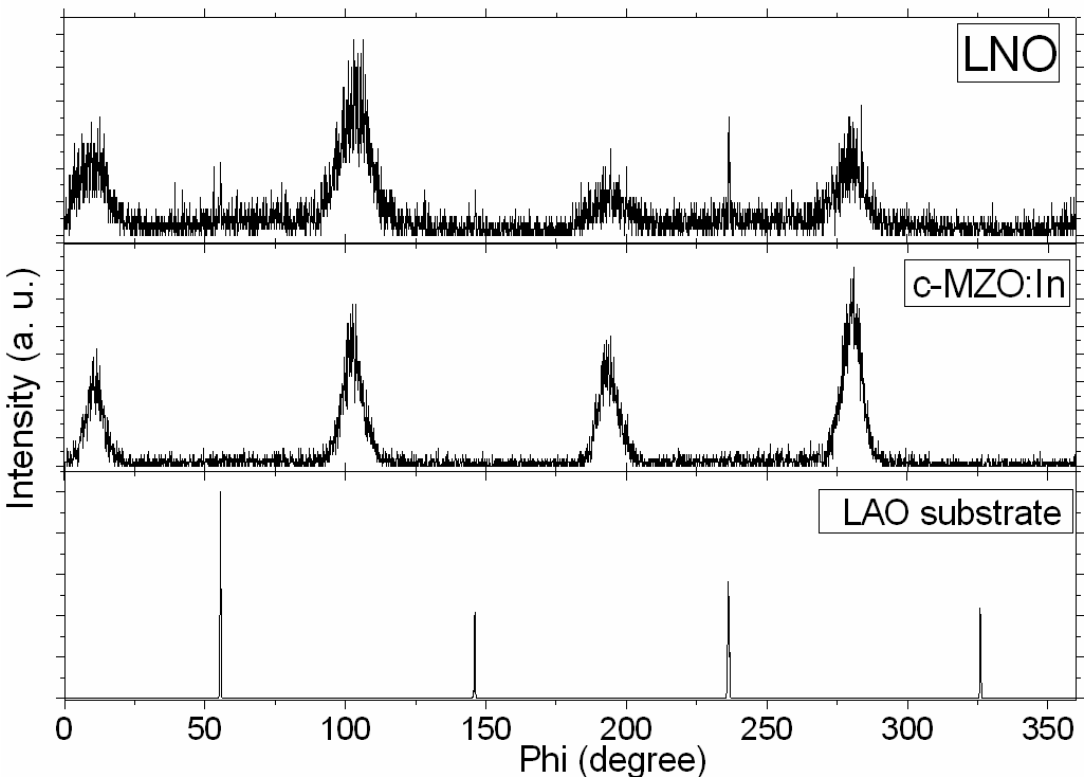

Figure 5.10 XRD 360˚ phi-scans of c-MZO:In/LNO heterojunction on LAO (0 0 1) substrate

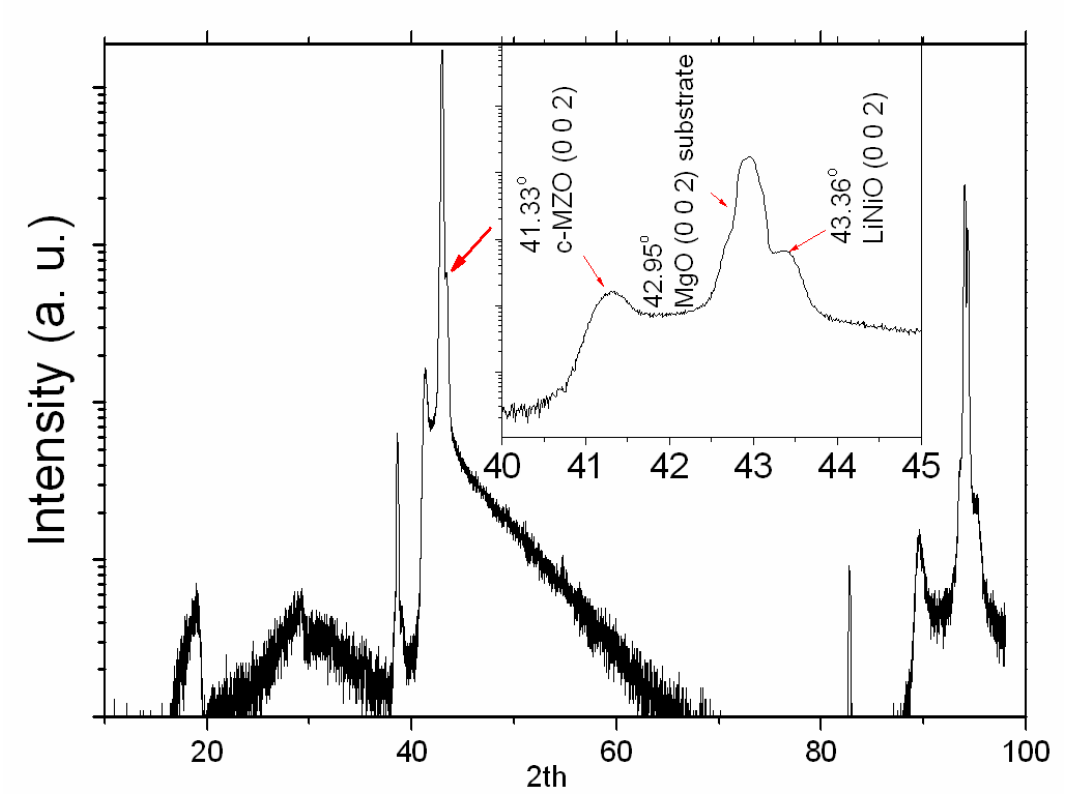

Figure 5.11 XRD θ-2θ scan of c-MZO:In/LNO heterojunction on MgO (0 0 1) substrate

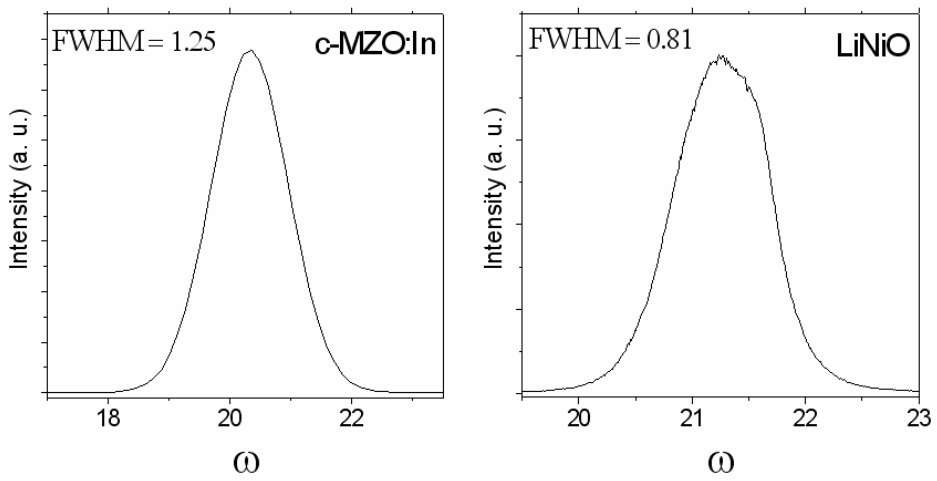

Figure 5.12 XRD ω scans of c-MZO:In/LNO (0 0 2) diffraction planes heterojunction on MgO (0 0 1) substrate

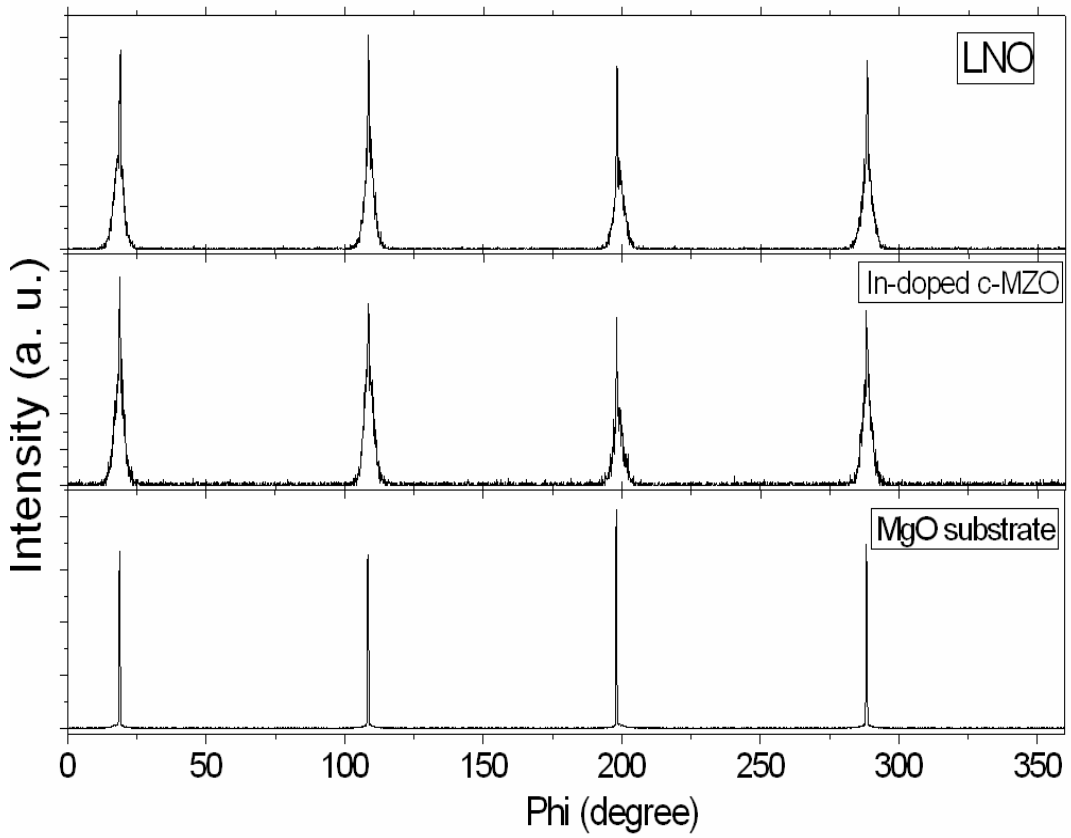

Figure 5.13 360˚ phi-scans of c-MZO:In/LNO heterojunction on MgO (0 0 1) substrate

5.3 Electrical measurement of c-MZO:In/LNO p-n heterojunction

5.3.1 Current-voltage characteristic

The current-voltage characteristic of the c-MZO:In/LNO p-n heterojunction fabricated on MgO substrate by PLD is measured at room temperature. In Fig. 5.14, ohmic contacts are confirmed between Pt and c-MZO:In as well as LNO single layers. Fig. 5.15 shows the nonlinearity of the current-voltage curves of the junctions against different separations between two electrodes. Junctions with closer electrode separation display higher forward current. The reverse biased currents show similar dependence. The slopes of the I-V curves in the forward biased voltage represent the series resistance of the junctions, indicating the resistance of the junctions changes against the separation of the c-MZO:In film. The turn-on voltages of all junctions are approximately at 1.8V.

In order to examine the effect of the resistivity of c-MZO:In film on the measured junction characteristics, c-MZO:In n-layer with two different In content, 16 and 18 at. %, are used. The deposition conditions for the LNO p-layers are kept unchanged. I-V curves of the p-n junctions are plotted and shown in Fig. 5.16 and 5.17. Surely, the two I-V curves give different slopes in the forward biased currents. The resistivities of the two c-MZO:In films are greatly different as has been shown in previous chapter. Apart from having smaller forward current, the p-n junction with lower In content exhibits larger leakage current too. In Fig. 5.18, we measure the ratio of the forward current to the backward current for the two p-n junctions. For the one with higher In content, the ratio reaches about 60 when the applied voltage is 2.5V. The other junction shows a ratio of only 11. When the voltage is larger than 2.5V, the ratios of both junctions

become smaller because of the large leakage currents. From the diagram shown, the difference of the turn-on voltage of two junctions is small.

I-V profiles of p-n junction fabricated under other deposition conditions are also illustrated in Fig. 5.19. All results show alike non-linear characteristic but with slight variation in magnitude of current. The junctions give similar turn-on voltage though. It can be concluded that the deposition conditions used for growing c-MZO:In and LNO layers in the present work are optimized for good rectifying properties of the junction.

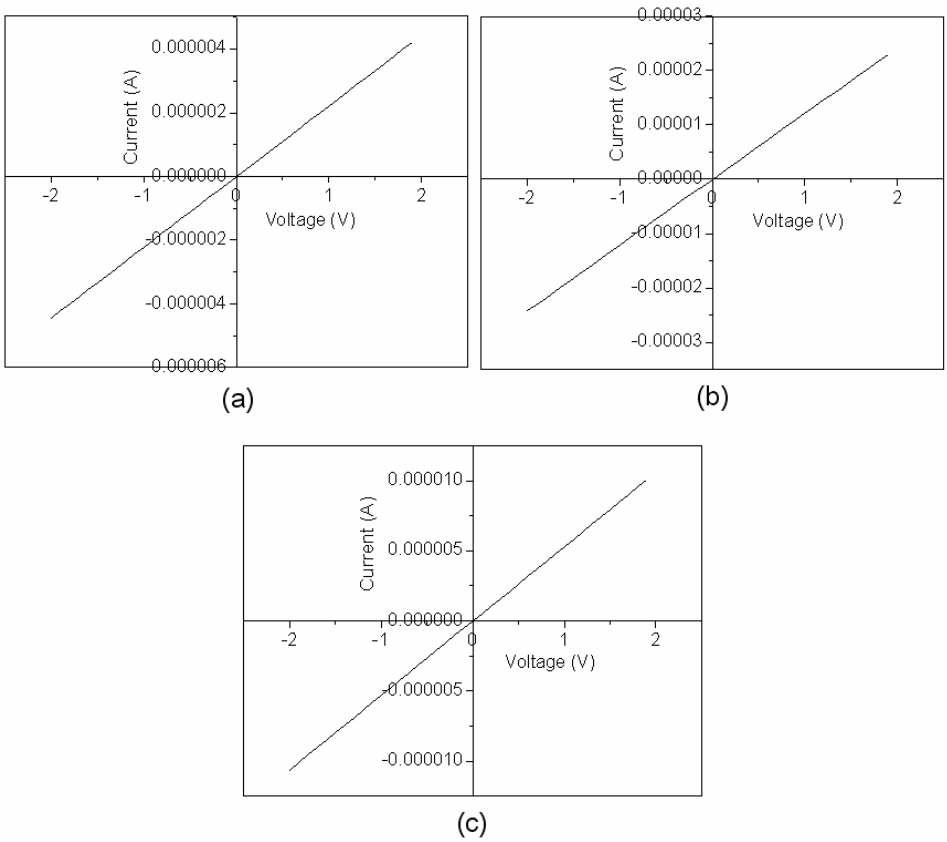

Figure 5.14 Ohmic contacts of (a) Pt on c-MZO:In, (b) Pt on LNO and (c) Au on c-MZO:In

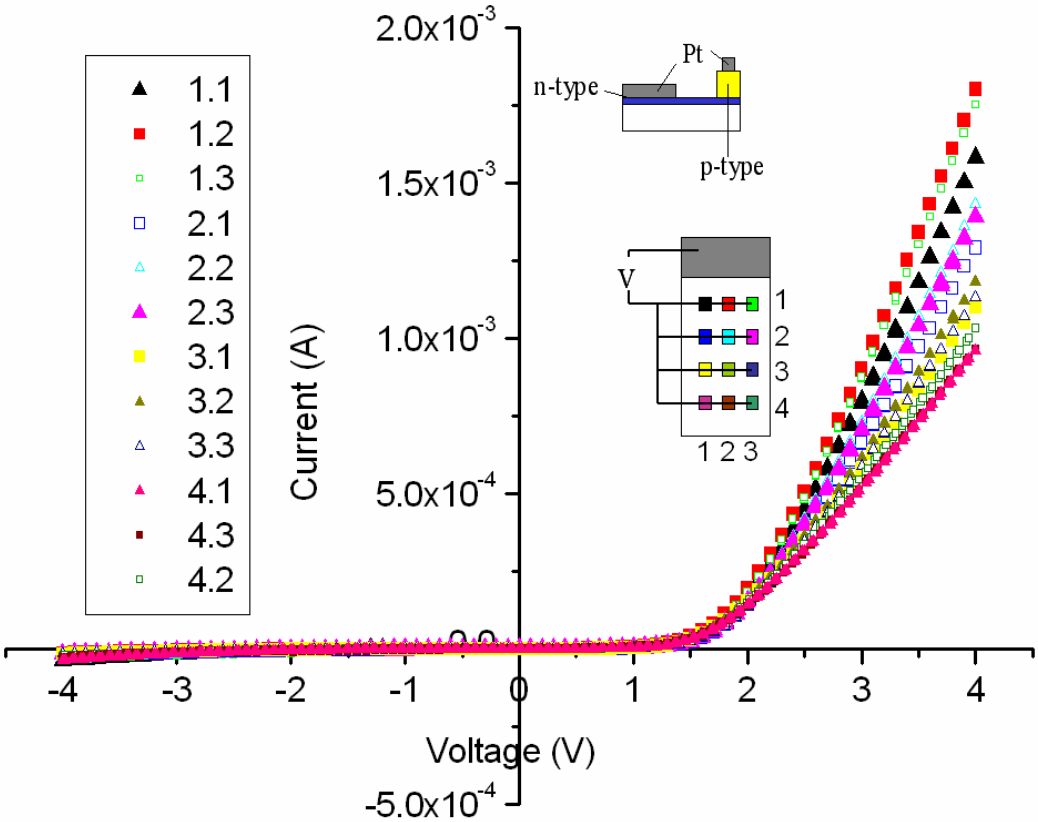

Figure 5.15 The rectifying profiles of c-MZO:In/LNO heterojunction on MgO (0 0 1) substrate

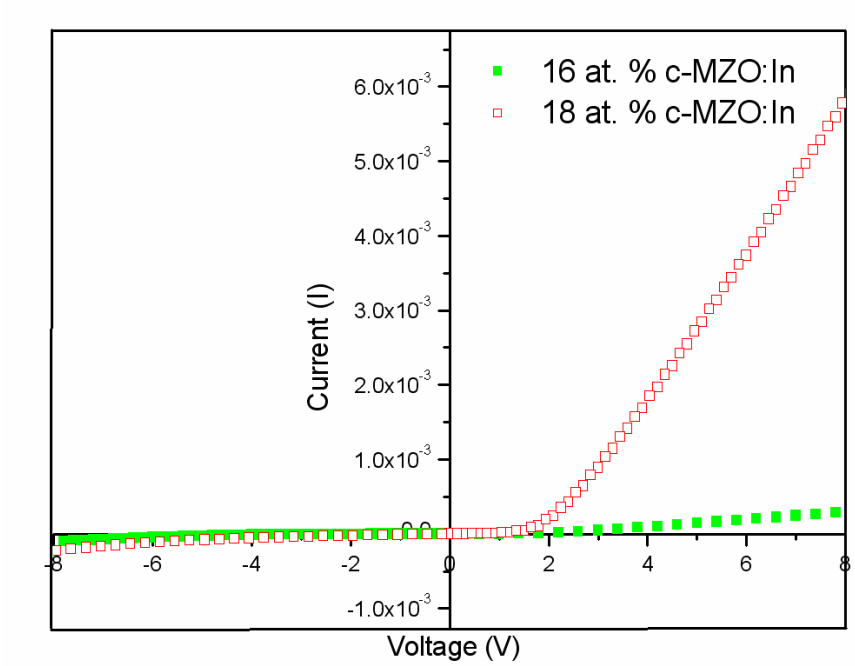

Figure 5.16 The rectifying profiles of c-MZO:In/LNO heterojunction with 16 and 18 at. % indium (same scale)

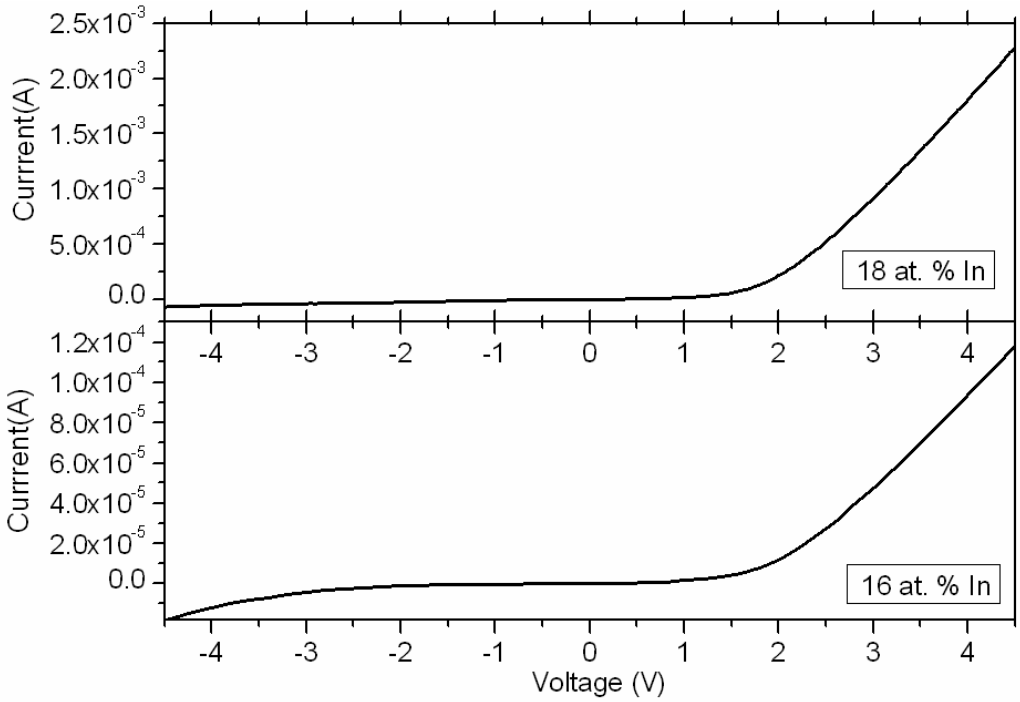

Figure 5.17 The rectifying profiles of c-MZO:In/LNO heterojunction with 16 and 18 at. % indium (not in scale)

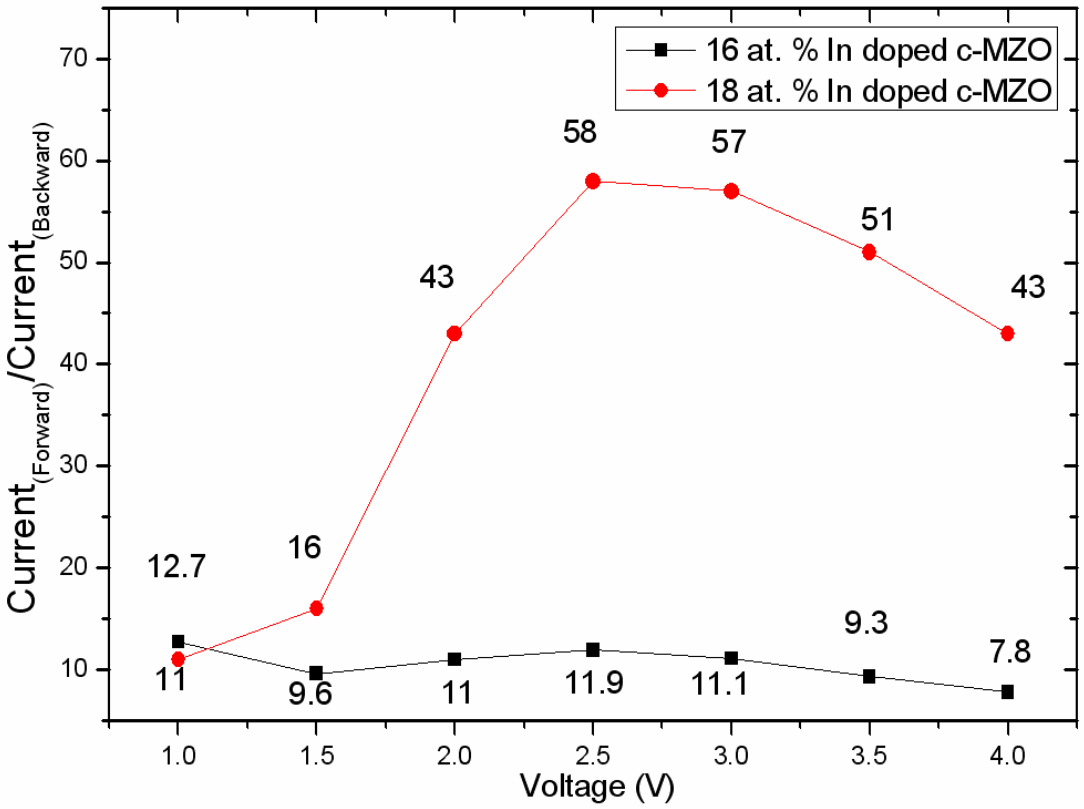

Figure 5.18 The ratios of forward to backward current of c-MZO:In/LNO heterojunction with 16 and 18 at. % indium

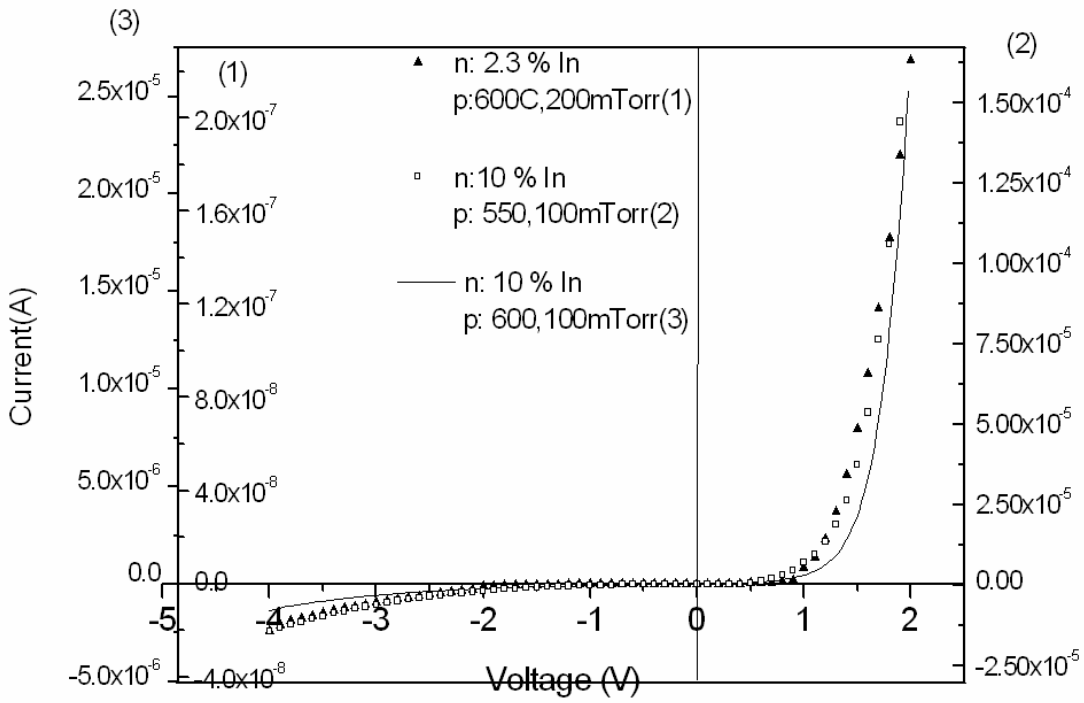

Figure 5.19 The rectifying profiles of c-MZO:In/LNO heterojunctions with different deposition conditions

5.3.2 Temperature dependence current-voltage characteristic

One of the noted characteristics of oxide is its stability at even high temperature. The oxide based semiconductors are therefore expected to withstand high temperature operation. We have measured the I-V profile of the c-MZO:In/LNO heterojunction at different temperatures. The results are shown in Fig 5.20. It can be observed that the turn-on voltage decreases with increase of temperature. The current passes through the junction is also increased. At the forward bias of 4V, 1.5mA of forward current is measured at 330K while less than 10 μA passes through at 130K.

As discussed previously, the measured I-V profiles are much affected by the series resistance caused by the semiconducting c-MZO:In of relatively low conductance. They do not reflect truly the p-n junction characteristics. In order to yield a more realistic picture of the junction performance at different temperature, we eliminate the series resistance effect of the junction by subtracting the potential drop across the film. Fig. 5.21 shows the I-V curves of the junction after the subtraction treatment. Nearly ideal rectifying profiles are seen. The turn-on voltages are measured and plotted in Fig. 5.22. From 380K to 250K, the turn-on voltage changes from 1.6V to 2.6V with a rate of $-6.7mVK^{-1}$. In the range 250K to 130K the rate is more than double at $-15mVK^{-1}$.

The Napierian logarithms of current against voltage with different sample temperatures are plotted in Fig. 5.23. There are gradual changes of slopes with various applied voltage when the temperature drops. If we compare the same plot of silicon diode shown in the inset of Fig. 5.23 [5-20], some characteristics of the non-ideal diode also appear in the all oxide p-n junction at low temperature. For silicon diode, the

ln(I)-V plot can be classified into four regions. The regions are the depletion region recombination, ideal diode current, high injection region and series resistance region.

In the real p-n junction, the material quality is not very pure. There are inevitably chemical impurities present. The doping process itself can cause defects such as vacancies, interstitials, etc. [Jasprit Singh, 2001] [5-21] When small external voltage is applied to the junction, electrons and holes enter the depletion region. One possible way they cross the region without overcoming the potential barrier is to recombine with each other. This leads to an additional flow of charged particles. This is the recombination-generation current, which is

$$I_{GR} = I_{GR}^{o}(e^{\frac{qV_A}{2kT}} - 1)$$

Therefore, the total current is

$$I = I_o(e^{\frac{qV_A}{kT}} - 1) + I_{GR}^{o}(e^{\frac{qV_A}{2kT}} - 1)$$

$$I \cong I_s(e^{\frac{qV_A}{nkT}} - 1)$$

where *n* is called the diode ideality factor. At low applied voltage, I_{GR}^{o} is much larger than I_o for real devices, thus the diode current is dominated by the generation-recombination current and n=2. When the applied voltage increases, the diffusion current starts to dominate, then n=1. The two regions in the forward I-V characteristics of the c-MZO:In/LNO p-n junction are shown as Fig. 5.24.

When the voltage keeps rising, the injected level increases, eventually the injected

minority carrier density becomes comparable to the majority carrier density. Thus, the voltage drops in the undepleted region significantly. The current stops to increase exponentially with the applied voltage but becomes saturated. As the forward bias increases, the p-n junction starts to have ohmic behavior, where the current-voltage relation is given by a simple linear expression. The potential is now dissipated by the resistance of the n-type and p-type regions.

For c-MZO:In/LNO p-n heterojunction, similar characteristic appears when the sample temperature decreases from 380K to 130K. The slope is sketched to define different regions of the junction characteristic. The ideality factors of the junction are measured. At 180K the factors is 15.73 at the zones of depletion region recombination and high injection, while it changes to 20.94 in the ideal diode region. The values show that the efficiency is much lower than the Si diode.

At the temperature range from 130K to 230K, the ideality factors with the four regions can be indicated and the values are calculated in Fig. 5.25 and Table 5.1. It is noticed that the ideality factors increase when the temperature drops. From the I-V equation $I \cong I_s(e^{\frac{qV_A}{nkT}} - 1)$, the product of the ideality factors and thermal energy kT increase means that the exponential function has sharp change at a higher applied voltage value. This directly corresponds to a rise in turn-on voltage. At the temperature higher than 230K, the regions of four different physical phenomena are hard to be identified.

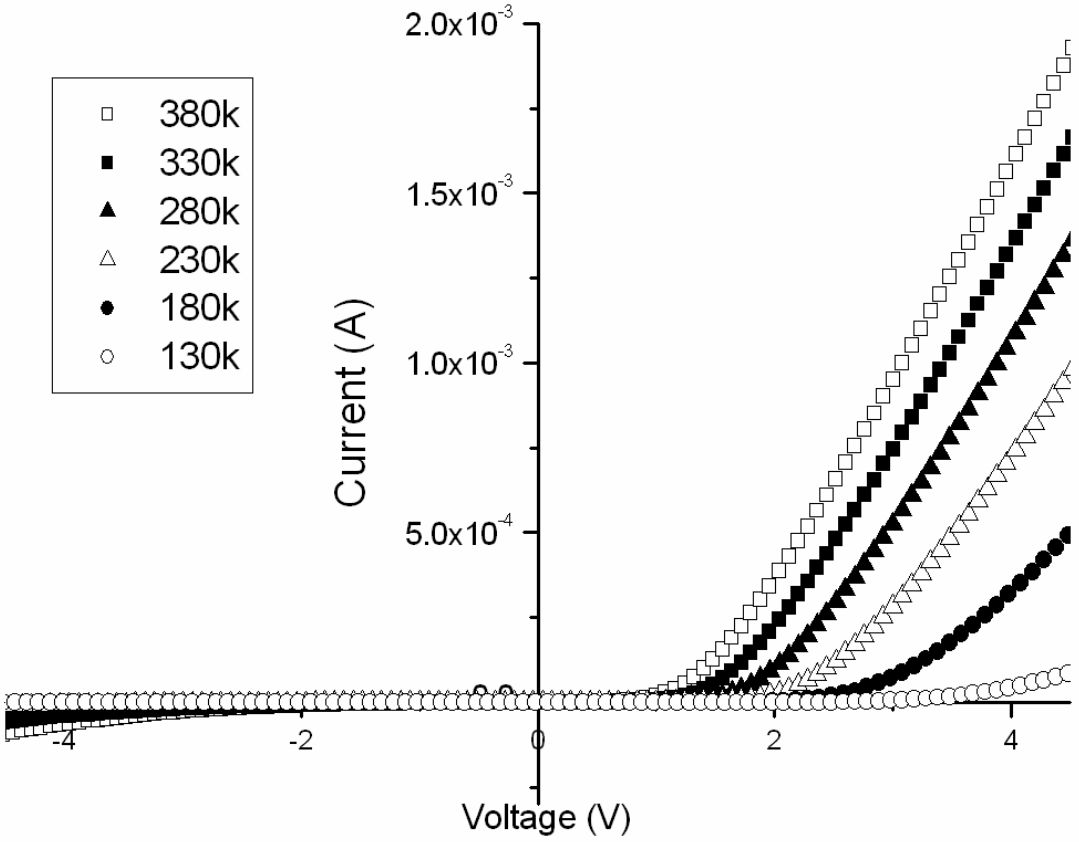

Figure 5.20 The rectifying profiles of 18 at. % c-MZO:In/LNO heterojunction under different measuring temperature.

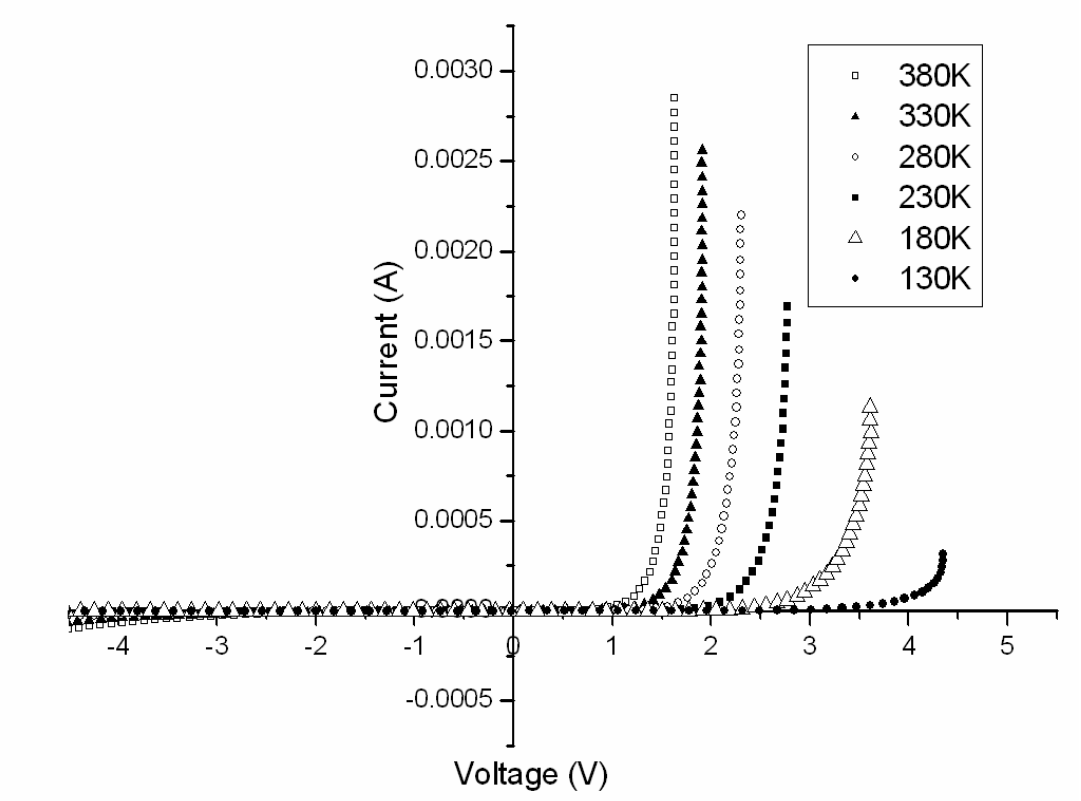

Figure 5.21 The rectifying profiles of 18 at. % c-MZO:In/LNO heterojunction series resistance elimination under different measuring temperature.

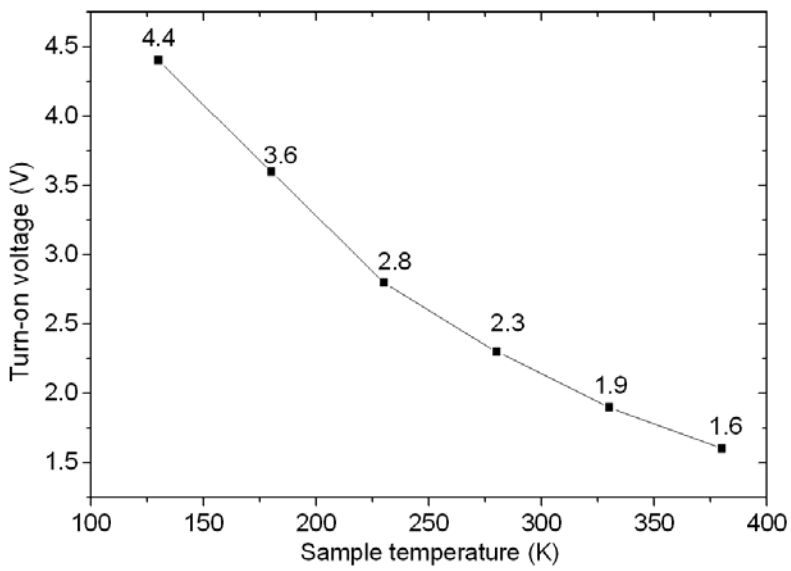

Figure 5.22 The turn-on voltages of 18 at. % c-MZO:In/LNO heterojunction under different measuring temperature.

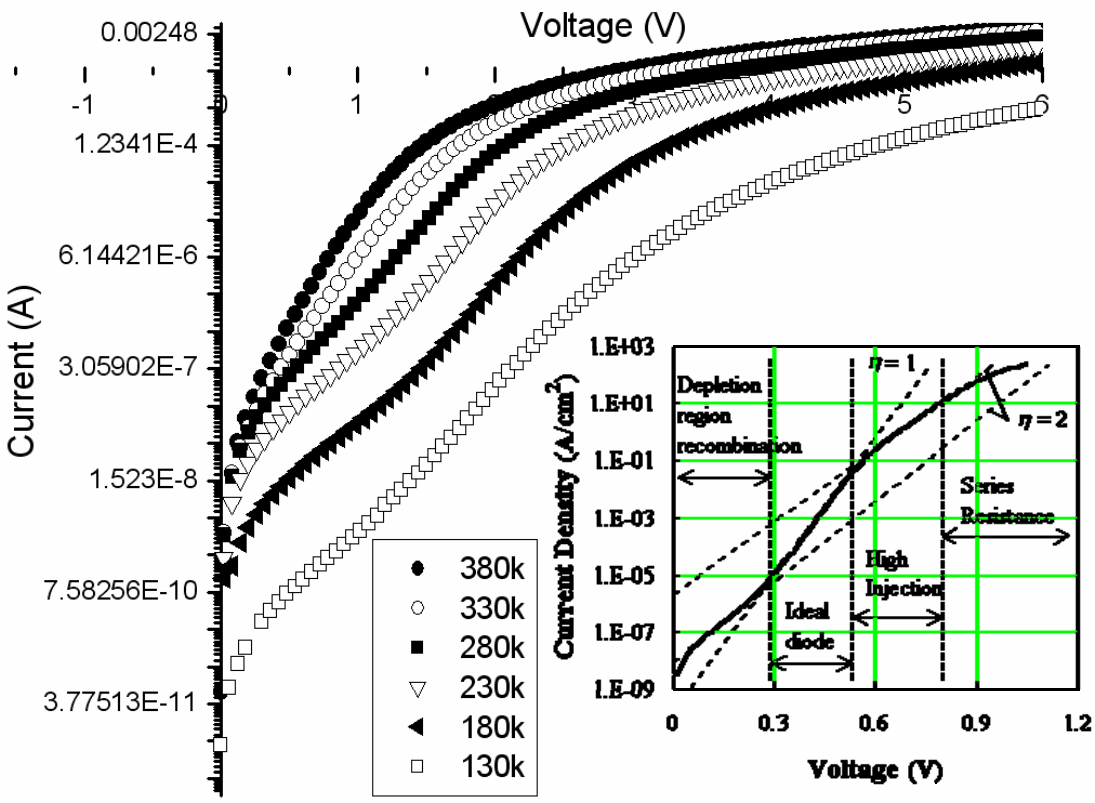

Figure 5.23 The ln plot of rectifying profiles of 18 at. % c-MZO:In/LNO heterojunction under different measuring temperatures and Si non-ideal I-V curve (from Bart Van Zeghbroeck [5-20]).

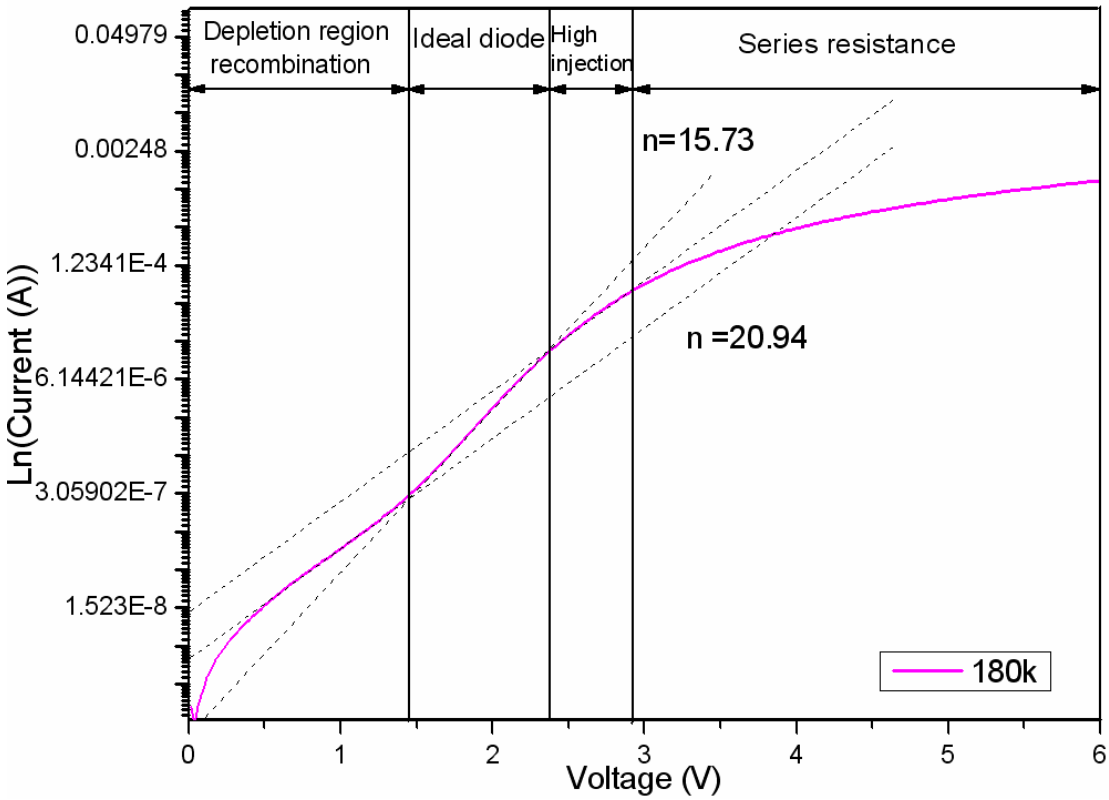

Figure 5.24 Current-Voltage characteristics of a c-MZO:In/LNO p-n junction under forward bias.

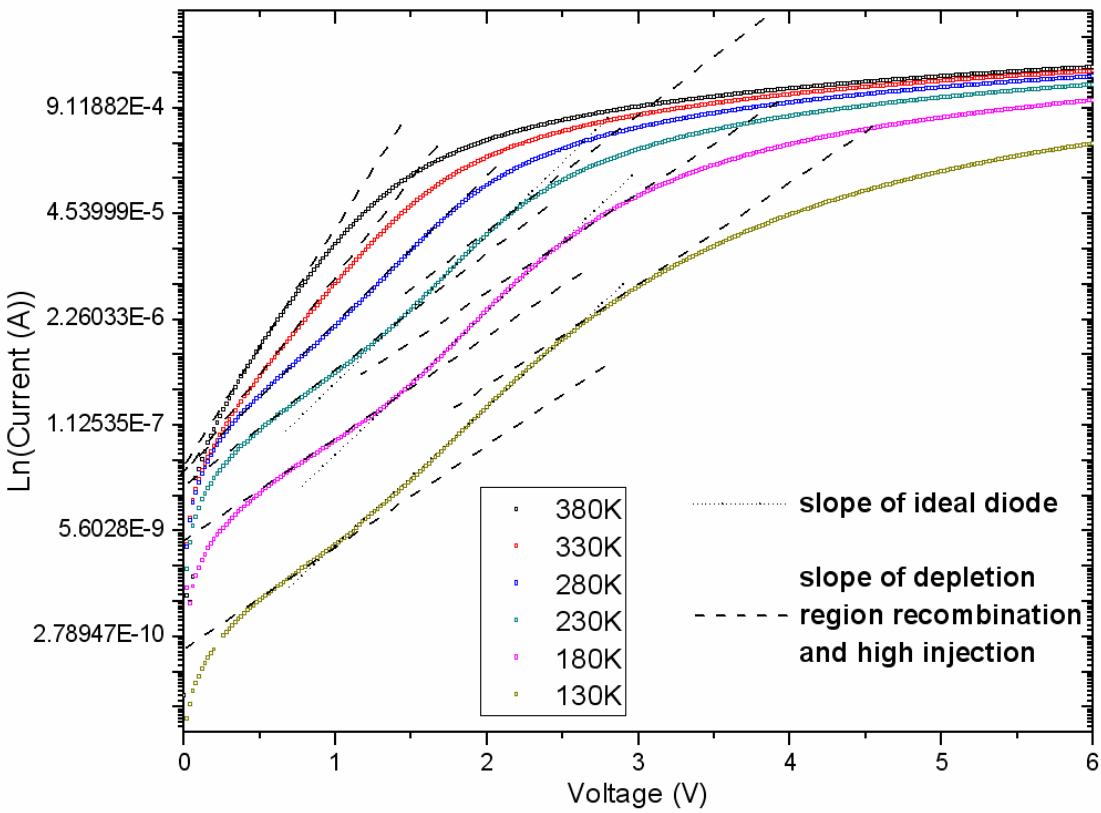

Figure 5.25 The slopes of the Ln(I) against voltage at different non-ideal characteristic.

Sample temperature	Slope of depletion region recombination	Ideality factor of depletion region recombination	Slope of ideal diode	Ideality factor of ideal diode
380K	6.72	4.55		
330K	5.60	6.28		
280K	4.16	9.97		
230K	3.45	14.63	4.13	12.22
180K	3.08	20.94	4.10	15.73
130K	3.14	28.43	3.86	23.13

Table 5.1 The values of the ideality factors at different regions against sample temperature.

5.4 Optical measurements of c-MZO:In/LNO p-n heterojunction

In the previous sections, c-MZO:In and LNO thin films have been shown to be good transparent conducting semiconductors independently. By merging the two films together, a transparent all-oxide p-n heterojunction is fabricated.

In Fig. 5.26, the transmittance profile illustrates the good optical transparency of the junctions. The deposition condition of the n-type c-MZO:In layers is fixed at 600˚C substrate temperature and 5×10^{-5} Torr vacuum condition, while the p-type LNO are deposited at various conditions: the substrate temperatures at 550˚C with 100 mTorr oxygen ambient, 600˚C with 100 mTorr and 600˚C with 150 mTorr. All deposited heterojunctions have average transmittance over 60% in the whole visible spectrum. The absorption edge changes with the LNO deposition condition but maintains good optical transparency. For the LNO films deposited at 600˚C with 150 mTorr, 600˚C with 100 mTorr and 500˚C with 100 mTorr, the absorption edges are about 330nm, 320nm and 300nm, representing the band gap energies are 3.76, 3.88 and 4.14eV respectively.

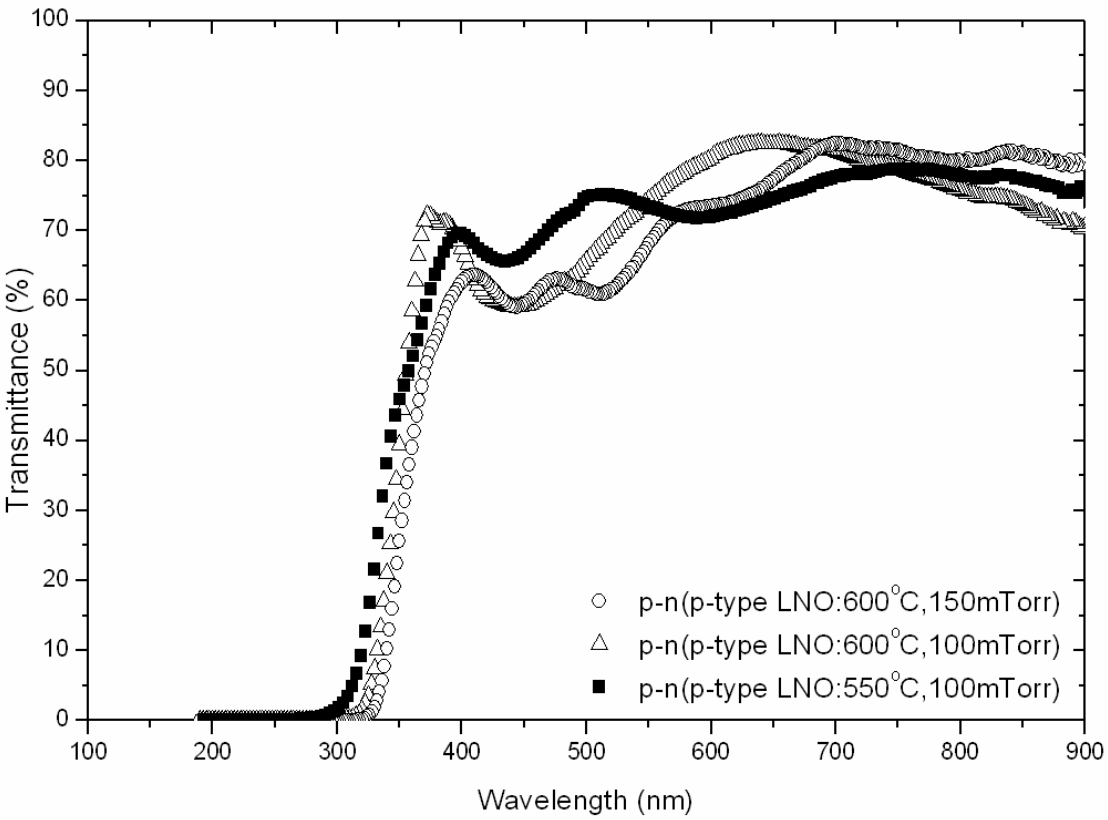

Figure 5.26 Transmittance profiles of the c-MZO:In/LNO heterojunction with different deposition condition of LNO.

Chapter 6

Fabrication and characterization of c-MZO:In/LNO on TiN buffered Si substrate

6.1 Introduction of TiN thin film

The c-MZO:In/LNO all-oxide p-n heterojunction is fabricated on titanium nitride (TiN) buffered silicon substrate. TiN thin film exhibits low electrical resistivity [6-1]. It can help to shorten the conduction path of the p-n junction described in previous chapter. TiN also possesses chemical inertness at atmosphere and high melting point (2930˚C). It has been commonly used as protective and decorative coatings in industrial electronics [6-2], [6-3], [6-4], [6-5], [6-6]. In our case, TiN buffer layer also acts as a barrier preventing inter-diffusion between the c-MZO:In layer and the Si substrate as deep-level trapping may occur under high deposition temperature [6-1]. The oxidation of silicon is another problem associated with device integration. The formation of amorphous SiO_2 layer substantially weakens the electrical performance of Si and inhibits epitaxial grow of crystalline films. TiN has been proposed to be a template for buffer growth of crystalline oxide films on Si [6-7], [6-8], [6-9]. It can be grown epitaxially on Si via domain matching.

The pure cubic phase TiN films are fabricated on Si substrates by PLD. The lattice constant of TiN (4.24Å) is structurally matched with that of the c-MZO:In layer (~4.2Å).

Therefore, we believe that the c-MZO:In/LNO can be epitaxially deposited on TiN buffered Si. In this chapter, the structural properties of all layers are discussed. We also highlight the electrical characteristic of the p-n junctions deposited on Si and compare their performance with those grown directly on MgO substrates.

6.2 Deposition of TiN on Si substrate

6.2.1 TiN target analysis

The TiN target was bought from the Electronic Space Products International Company (ESPI) with purity of 99.95%. Before the deposition, the target was examined by the XRD. Fig. 6.1 shows the XRD pattern of the TiN crystalline target. The diffraction peaks match with the data book values of the TiN structure, so the target is ready for the thin film deposition without further treatment. The TiN has a cubic structure and a lattice constant (bulk target) of 4.23Å, which is structurally compatible with Si substrate (5.43Å) and c-MZO:In thin film(~4.2Å).

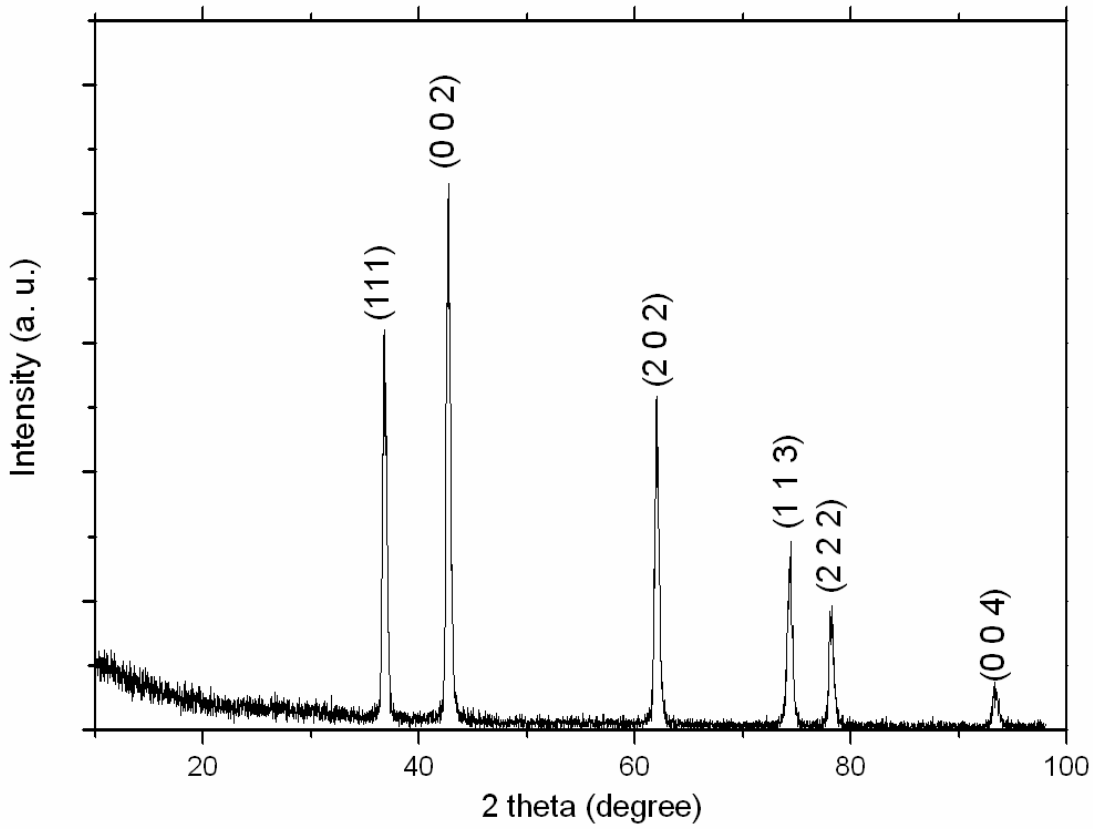

Figure 6.1 XRD powder diffraction of TiN target.

6.2.2 Deposition of TiN, c-MZO:In and LNO layers

TiN thin films were fabricated on Si (0 0 1) substrates by ablating the TiN crystalline target. As the oxidation of Si on the surface will influence the epitaxial growth of TiN, the substrates were first degreased by the ultrasonic cleaner in acetone. Then they were etched by a freshly prepared 5% HF acid solution for 4 minutes. The etched substrates were quickly placed in the vacuum chamber, which was then evacuated to 3×10^{-5} Torr base pressure by a diffusion pump. At such low pressure, the substrate temperature was raised to 600˚C. The deposition time was fixed at 30 minutes with 20 minutes of post-deposition annealing.

After the deposition of TiN on Si, c-MZO:In thin film was fabricated on top of the TiN layer, cover most part of the TiN film. The c-MZO without any dopant was grown between the n-type layer and the Pt electrode as an insulator. The purpose of the above geometry is to minimize the current path through the c-MZO:In so as to reduced the series resistance of the p-n junction measurements. On the top of the n-type c-MZO:In film, 500μm×500μm square p-type LNO and the 200μm diameter electrode were deposited. Fig. 6.2 is the schematic diagram of the p-n junction grown on TiN buffered Si. The injected current starts from the electrode on the TiN layer, passes through the TiN layer and vertically travels across the c-MZO:In/LNO heterojunction. The advantage of this design is that the TiN, having low resistivity, provides an electrical conduction path from the electrical leads to the p-n junction. So now the current-voltage characteristics can more truly reveal the performance of the junction.

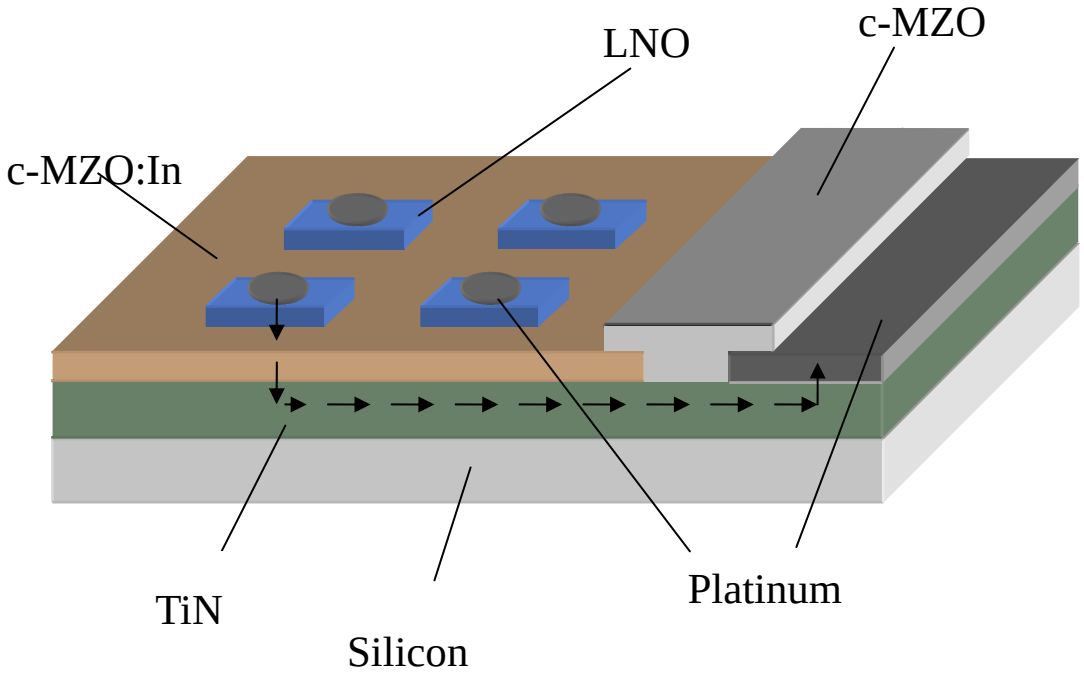

Figure 6.2 The schematic structure of c-MZO:In/LNO heterojunction on TiN buffered Si, the arrows are the flow of the electrons.

6.3 Structural measurements of c-MZO:In/LNO on TiN buffered Si substrate

6.3.1. Structural characterization of TiN on Si

Fig. 6.3 is the θ-2θ scan of the TiN layer on Si (0 0 1) substrate. Single cubic phase is observed with the peak angle at 42.49˚, indicating that the lattice constant is about 4.25Å. It matches with the lattice constant of the TiN (0 0 2) peak of the target. Therefore, we believe that the internal strain between the film and the substrate is small. The crystallinity of the TiN is relatively poor. The FWHM is about 2.79˚ from the omega scan shown in Fig. 6.4. The reason may attribute to the poor vacuum condition of the chamber.

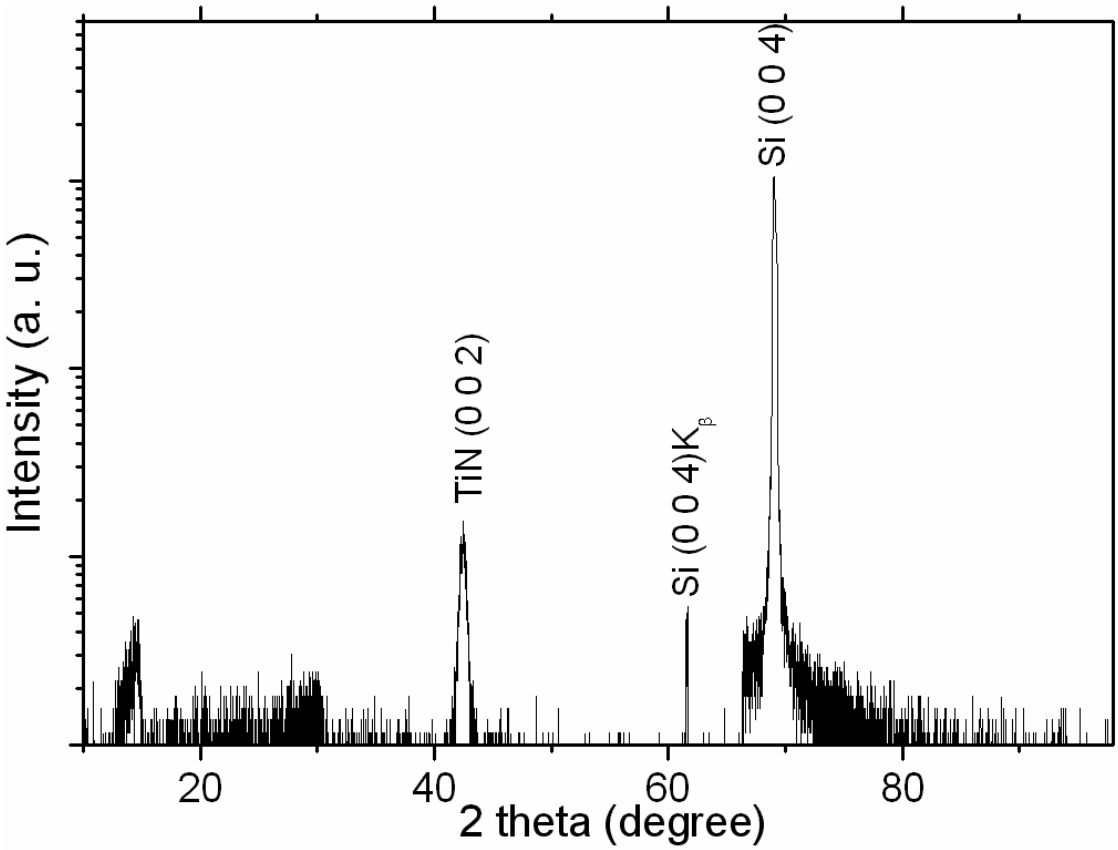

Figure 6.3 XRD θ-2θ scan of TiN on Si (0 0 1) substrate

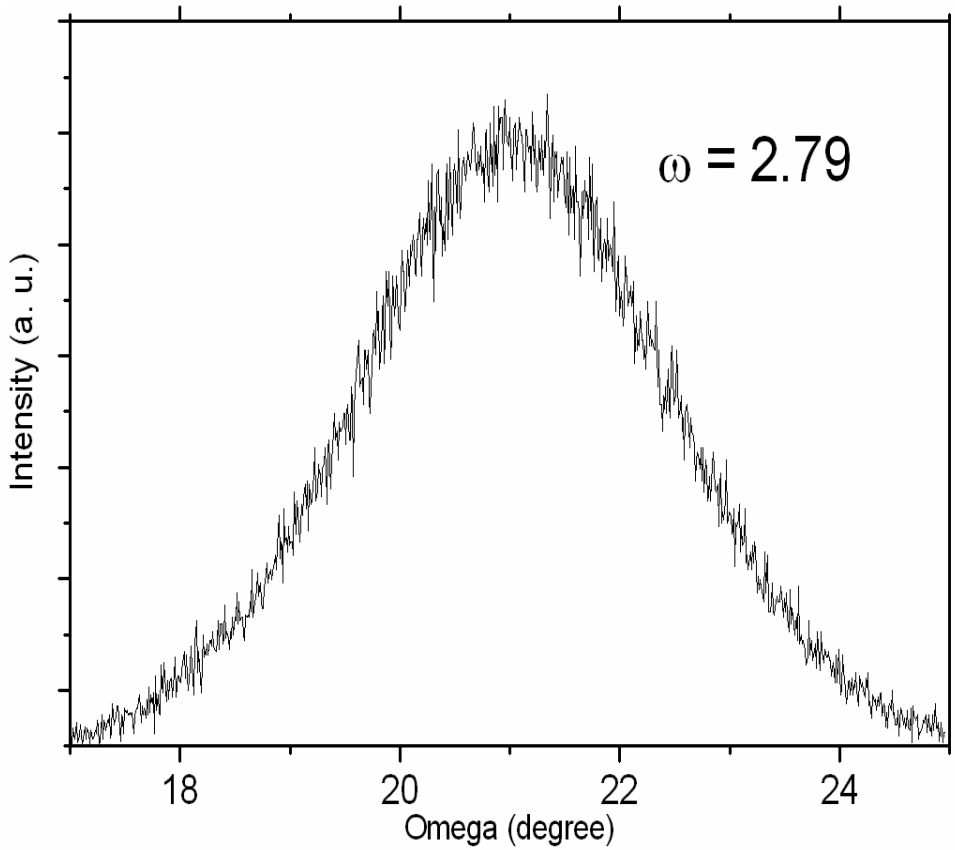

Figure 6.4 XRD ω scan of TiN (0 0 2) on Si (0 0 1) substrate

6.3.2 Structural characterization of c-MZO:In/LNO on TiN buffered Si substrate

In Fig. 6.5, the diffraction peaks indicate the cubic phases of c-MZO:In and LNO films (0 0 2) and how they orientated on the TiN film. It can be seen that all the peaks can be resolved from the inset of Fig. 6.5. The calculated lattice constants of c-MZO:In, TiN and LNO layers are 4.32Å, 4.25Å and 4.18Å respectively. The FWHM of the films are as poor as the TiN bottom layer. The FWHM of the (0 0 2) films of TiN, c-MZO:In and LNO are 3˚, 2.39˚, and 1.86˚ respectively. These are worse than the films deposited as single layer on the substrate. In Fig. 6.7, the 360˚ phi-scans reveal that all layers exhibit cubic epitaxial relationship with the typical four-fold of symmetry.

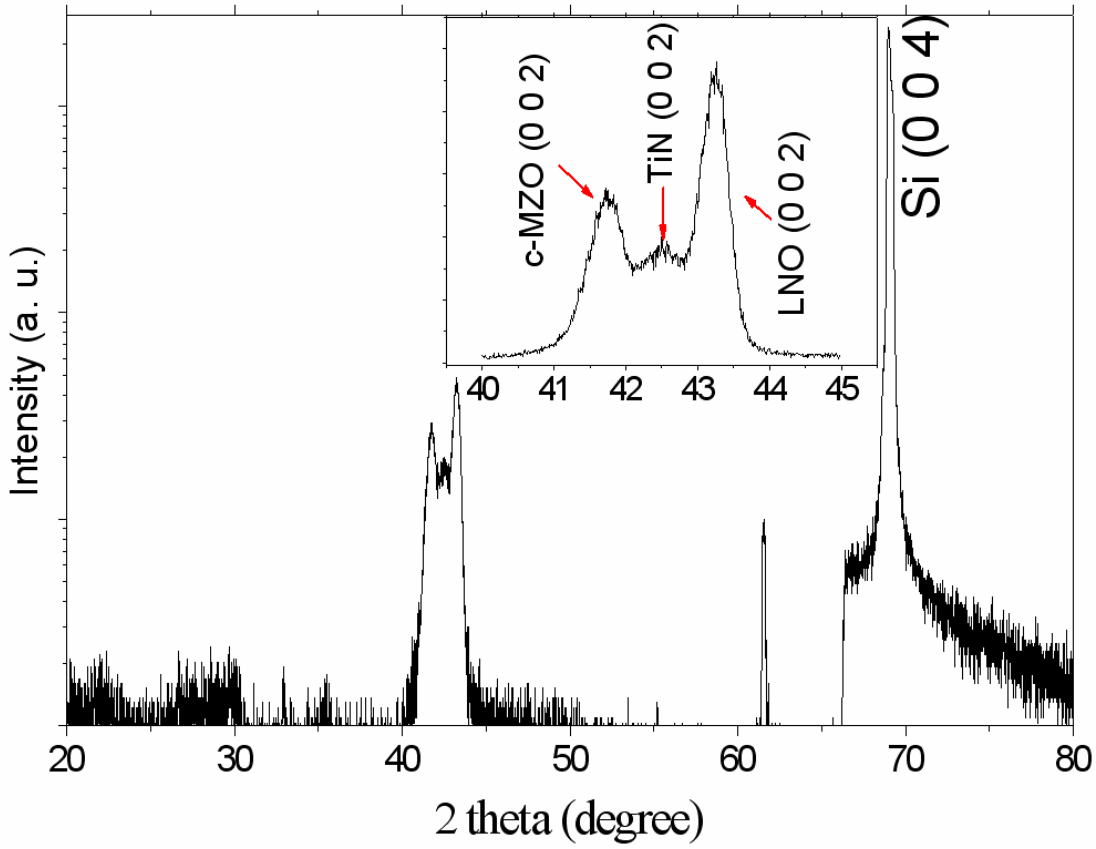

Figure 6.5 XRD θ-2θ scan of c-MZO:In/LNO heterojunction on TiN buffered Si (0 0 1) substrate.

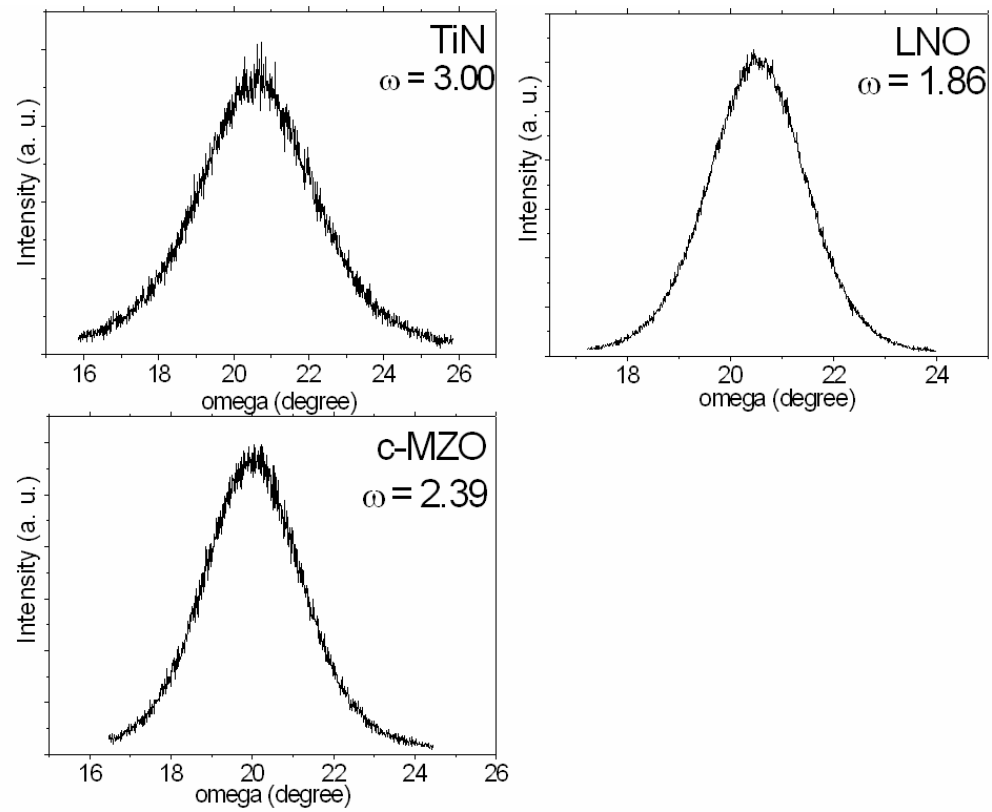

Figure 6.6 XRD ω scans of c-MZO:In/LNO (0 0 2) diffraction planes heterojunction on TiN buffered Si.

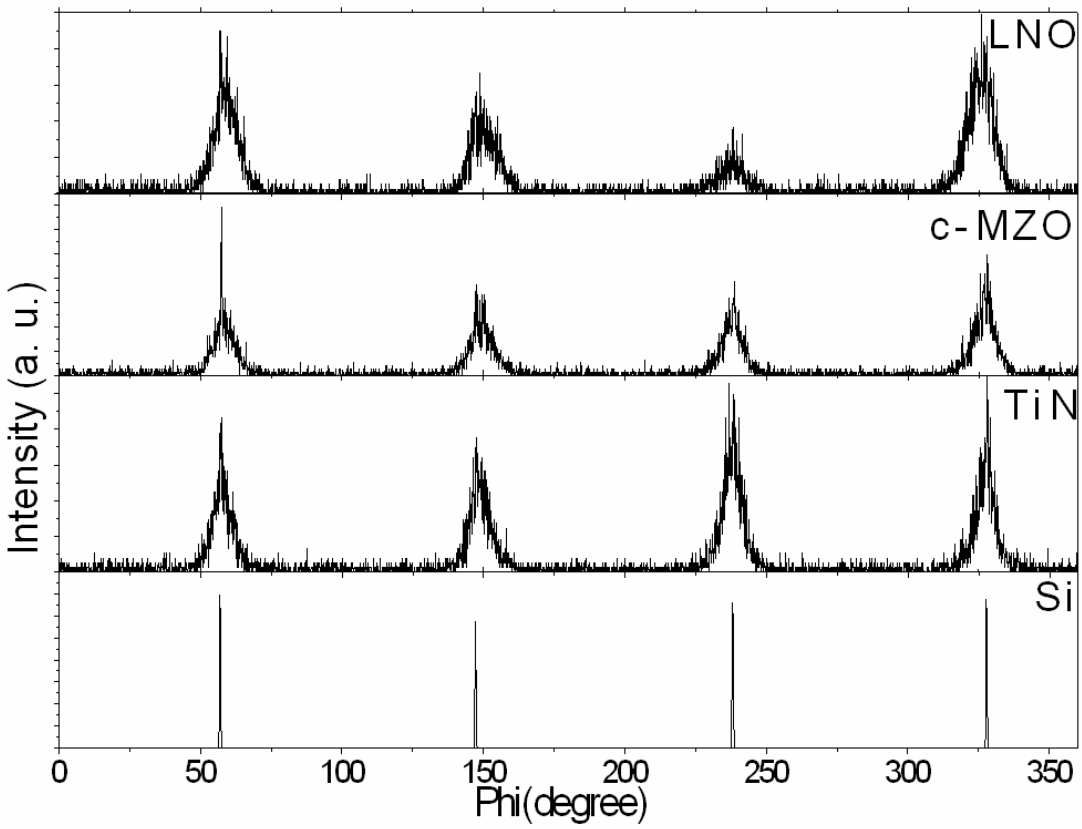

Figure 6.7 XRD 360˚ phi-scans of c-MZO:In/LNO heterojunction on TiN buffered Si.

6.4 Electrical measurements of c-MZO:In/LNO on TiN buffered Si substrate

6.4.1 Current-voltage characteristic

The current-voltage profile of the p-n junction is plotted as Fig. 6.8. The junction exhibits excellent rectifying characteristics. In the forward bias, the turn-on voltage of the junction is about 2.8 V, the leakage current is remarkably small which is different form the typical case of the all-oxide p-n junction. Traditionally, oxide p-n junction has a very narrow depletion width at the interface. At the reversed bias, the electrons can pass through the junction by tunneling. Therefore, all-oxide p-n junction normally demonstrates large leakage current. In the case of the c-MZO:In/LNO heterojunction on TiN buffered Si, the low reversed biased current is recorded.

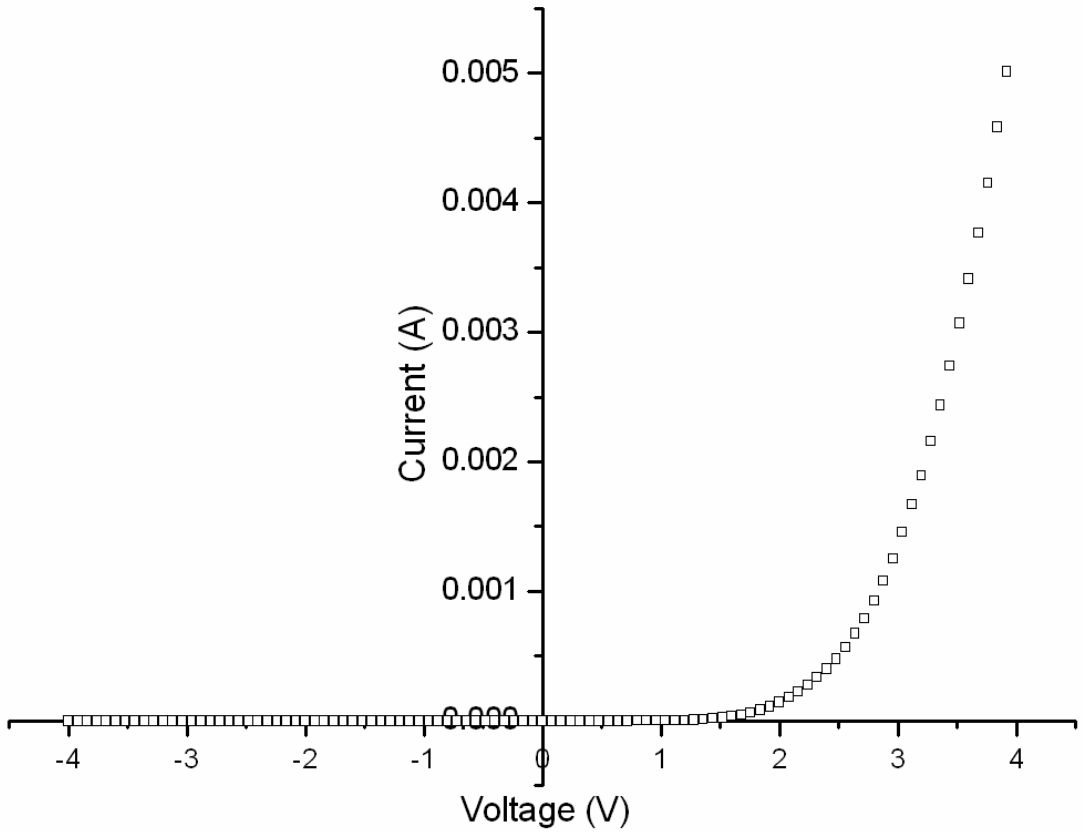

Figure 6.8 The rectifying profile of c-MZO:In/LNO heterojunction on TiN buffered Si

6.4.2 Comparison of c-MZO:In/LNO junction on MgO and Si substrates

Heterostructures of c-MZO:In/LNO p-n junction were deposited on MgO and TiN buffered Si substrates. The n-type layers were deposited at the same condition. For the p-type LNO, the one on MgO substrate was deposited at 600˚C with 100mTorr oxygen ambient pressure. The other on Si was deposited at 600˚C with 150mTorr. A comparison of the performance of these two p-n junctions was conducted.

It is believed that the two junctions have similar rectifying profile except the series resistance in the MgO substrate case is larger as the resistivity of the c-MZO:In layer is much larger than that of the TiN layer. I-V curves of the junctions are shown in Fig. 6.9.

When the curves are shown in the same scale, it can be seen that the p-n junction deposited on Si exhibits lager forward current due to the small series resistance of the TiN film. Apart from the larger forward current, the leakage current is also smaller in the Si case. In Fig. 6.10, when the two curves are lapped on the same graph but with different current scale, the turn-on voltages of the two curves are dissimilar. The p-n junction grown on Si demonstrates a larger turn-on voltage.

For the rectifying profile (the series resistance eliminated) shown in Fig. 6.11, the junctions behave very similar with the same shaped rectifying profiles. The ratios of the forward biased current to the reverse biased current for junctions grown on both substrates are measured. Fig. 6.12 shows different ratio and trends between the two cases. The ratio of the p-n junction grown on MgO substrate increases from bias voltage of 0.5V to 2.5V reaching a maximum value of 58. It is then dropped when the voltage is further increased to 3V. On the other hand, the current ratio of the p-n junction grown on TiN buffered Si keeps a monotonic increase within the measuring range. The ratio starts from 5 at 0.5V, climbing to approximately about 2200 when the voltage is up to 4 V.

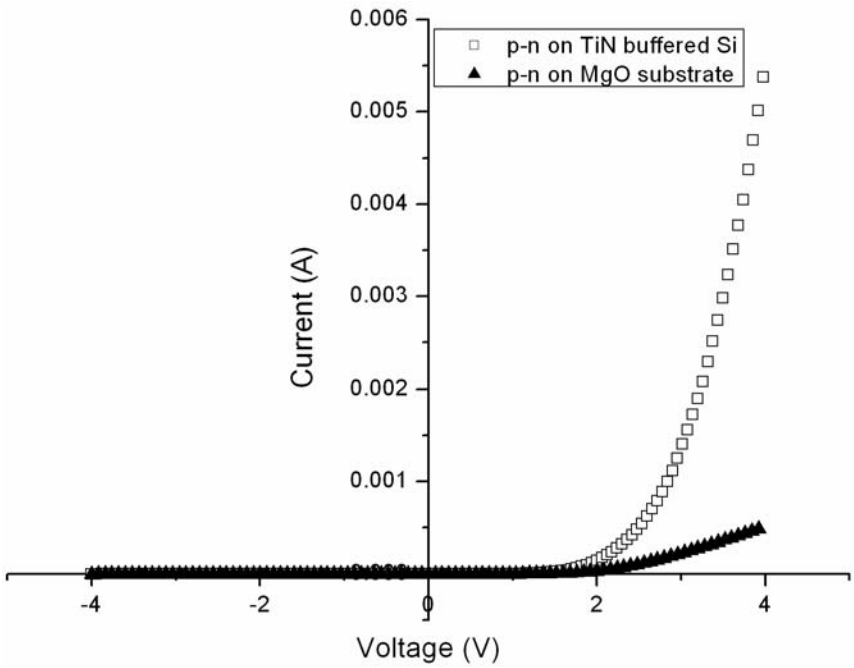

Figure 6.9 Comparison of c-MZO:In/LNO heterojunction on TiN buffered Si and MgO substrates (same scale)

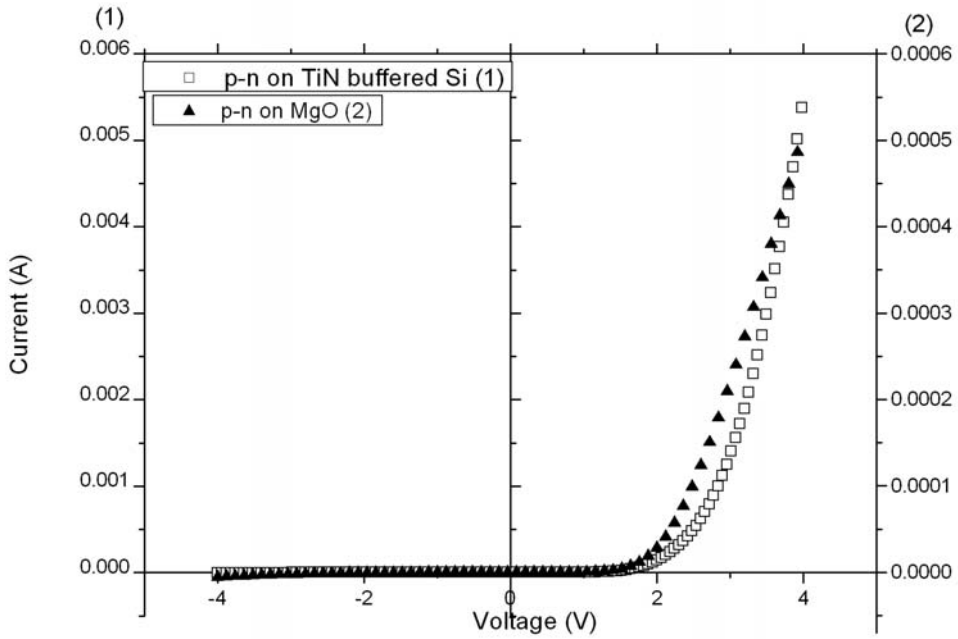

Figure 6.10 Comparison of c-MZO:In/LNO heterojunction on TiN buffered Si and MgO substrates (not in scale)

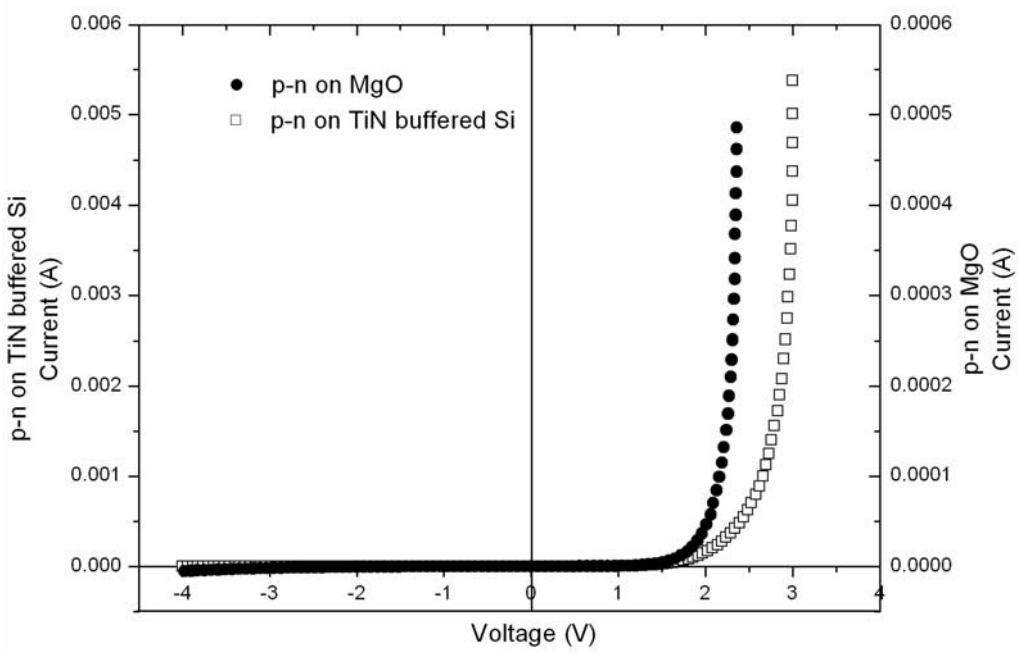

Figure 6.11 Comparison of c-MZO:In/LNO heterojunction on TiN buffered Si and MgO substrates without series resistance.

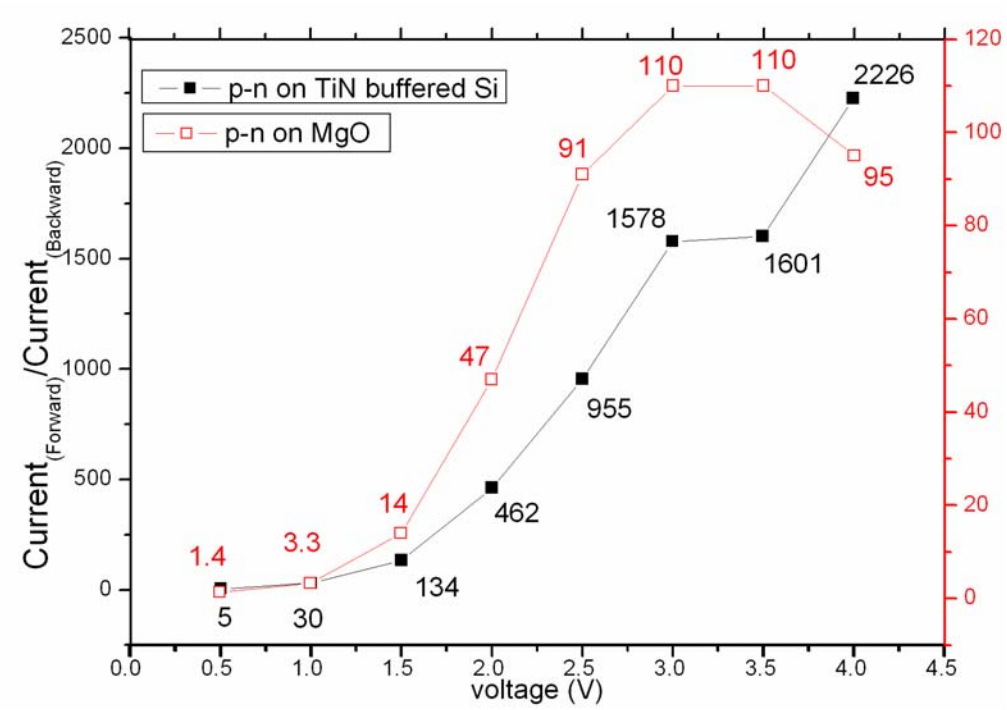

Figure 6.12 The ratios of forward to backward current of c-MZO:In/LNO heterojunction on TiN buffered Si and MgO substrates

Chapter 7

Conclusion

In our present investigation, indium doped cubic magnesium zinc oxide thin films were deposited on various substrates using pulsed laser deposition method. The mixed oxide targets were sintered with different composition of MgO, ZnO and In_2O_3. The crystal structure and surface morphology of the deposited films were studied. The electrical resistivity was measured as function of temperature from 20K to 380K. The transparent property of the films was also evaluated via absorption spectrometry. The relative composition variation of Mg, Zn and In from target to film was also investigated by XPS.

Single phase c-MZO:In films were successfully fabricated on MgO and LAO substrates. The deposition time was about 30 minutes followed by a 20 minutes post-deposition annealing. The film thickness was determined to be about 500nm by SEM cross-section imaging. At high deposition temperature, the Zn content was preferentially re-evaporated, leading to an increase of the Mg and In contents in the as-deposited films. Their structural qualities were studied by XRD and TEM. Films grown on MgO substrate reveal cube-on-cube heteroepitaxy. Those grown on LAO substrate however, show a heteroepitaxial relationship of $(0\ 0\ 1)_{c\text{-}MZO}||(0\ 0\ 1)_{LAO}$ and $(011)_{c\text{-}MZO}||(010)_{LAO}$.

The characterization of c-MZO films against indium dopant and substrate temperature was conducted. With different indium concentration from 4 at. % to 18 at. %, the lattice constants of the c-MZO:In films deposited at 600˚C vary from 4.30Å to 4.36Å. This leads to little lattice mismatch (2~3%) with the MgO substrates. The quality of crystalline structure of the c-MZO:In films is also dependent on the indium content. For a 4 at. % In doping, the FWHM of the film is 0.87˚. It increases to 1.9˚ if the In content rises to 18 at. %. The introduction of In also influences the surface morphology of all deposited films. At low indium concentration, however, the film is flat and smooth. The roughness increases at high doping concentration. The r.m.s roughness is about 4.8nm. Because of the free electron generation from In doping, the resistivity drops from $2.57\times10^{7}\Omega$cm for pure c-MZO to $5.5\times10^{-2}\Omega$cm for 18 at. % In doped c-MZO. the semiconducting behavior of the c-MZO:In is confirmed by measuring the temperature dependent resistivity. Hall measurement suggests that the c-MZO:In films has n-type conduction. The carrier concentration of 8, 16 and 18 at. % In doped c-MZO:In are 1.47×10^{18}, 2.04×10^{19} and 8.22×10^{19} cm^{-3} respectively. The transmittance of all deposited films is above 80% over the whole visible wavelengths. The band gap energy of the 4, 8 16 and 18 at. % In doped c-MZO:In films are 5.6, 4.4, 4.3 and 4.1eV respectively. The reason of the smaller band gap with higher In concentration may attribute to the decline of the Mg/Zn ratio. The refractive index of c-MZO:In is found by “prism coupling” technique to be about 1.86.

The effect on the properties of c-MZO:In thin films due to different substrate temperatures during film growth were studied. Structurally, the lattice constant of c-MZO:In thin film increases with the substrate temperature. Same as the band gap

energy variations, the lattice constant is also composition dependent. The low vapor pressure of Zn leads to an increase of the relative ratio of In and subsequently enlarging the unit cell of the c-MZO system. Therefore, the crystalline quality is expected to be poor at high In content. Films grown at high substrate temperatures also show better and smoother surface morphology. The resistivity of the thin films is highest when the substrate temperatures are kept at 300˚C and 400˚C during film growth. At these relatively low temperatures the dopant may not have sufficient thermal energy to substitute into the Zn site for free carrier generation. For films grown at 500˚C to 600˚C, their resistivities are substantially reduced to 2.86 and 0.25Ωcm respectively. The transmittance measurement of the films deposited at different substrate temperatures shows small shifts in band gap energy of the c-MZO:In films due to composition changes. Based on the structural, electrical and optical considerations, the optimal film deposition condition is to use the 18 at. % In doped MZO target to grow n-type semiconducting c-MZO:In thin film at 600˚C substrate temperature.

After perfecting the fabrication of n-type c-MZO:In thin film, we turned our attention to grow p-type LNO conducting oxide thin films. For the LNO single layer deposited on MgO, the lattice constant of the LNO is measured as 4.18Å. This is very close to the lattice constant of the c-MZO:In film. We then fabricated the c-MZO:In/LNO p-n heterojunction on MgO and LAO substrates. All the LNO and c-MZO:In bilayers on MgO and on LAO substrates show pure cubic phases and has good epitaxial relationships.

The c-MZO:In/LNO heterojunction demonstrates good rectifying profile. The

turn-on voltage is about 1.8V. The p-n junction with different conduction separation changes the forward biased current, indicating that the non-ideal I-V characteristic exists. Various doping concentrations can substantially improve the magnitude of the forward biased current without altering the turn-on voltage. The ratios of the forward to backward current proof that the p-n junction with higher doping concentration has the better performance

Experimenting at different temperature range, the p-n junction demonstrates various non-linear rectifying profiles. From 130k to 380k, the forward biased current at the same potential increases rapidly. Excellent I-V rectifying profile is obtained after the deduction of the series resistance. The turn-on voltage decreases with increase of temperature, changing from 4.4V at 130K to 1.6V at 380K. The Napierian logarithm of current against voltage plots further display the non-ideal I-V characteristic. The four current regions of the non-ideal p-n junction appear. They are the depletion region recombination, ideal region, high injection and series resistance.

The c-MZO:In/LNO heterojunction was also fabricated on TiN buffered Si. Electrical properties of the c-MZO:In/LNO heterojunctions were studies by measuring the I-V characteristic. Comparing the junctions grown on TiN buffered Si and on MgO, it is shown that the p-n junction fabricated on TiN buffered Si actually shows a much better performance with larger forward biased and smaller reversed current. The ratio of the forward to backward current reaches 2000. This gives about 20 times higher than the value of the junction fabricated on the MgO substrate. This last result is remarkable in that it suggests the real possibility of producing a truly integrated all-oxide p-n junction

diode.

Based on the results obtained, the c-MZO:In can act as a transparent n-type conducting template or electrode for growing other kinds of oxide ceramics thin films. Other possible application of c-MZO:In single layer can be a tunable UV filter. By merging with another transparent p-type material, optically transparent thin film transistor (TFT) for LCD display, UV detector, photovoltaic devices and even UV diode lasers are possible. If the transition metal (Co, Ni, Mn, Fe,…) doped c-MZO:In turns out to be a room temperature diluted magnetic semiconductor (DMS), it can be a very useful spintronic material for new types of magneto-electronics such as spin valves and tunnel junction devices.

References

[1-1]. J. H. Kim, H. J. Kim, D. J. Kim, Y. E. Ihm, W. K. Choo, "The origin of room temperature ferromagnetism in cobalt-doped zinc oxide thin films fabricated by PLD" , J. Eur. Ceram. Soc., v 24, n 6, p 1847-51, 2004.

[1-2]. I. Apostol, R. Stoian, C. Luculescu, R. V. Dabu, A. Stratan, S. Udrea, C. Flacau, "Laser ablation of YBCO targets and optical-breakdown-assisted PLD for high Tc superconducting thin films deposition ", Proceedings of the SPIE - The International Society for Optical Engineering, v 3423, p 379-83, 1998

[1-3]. F. K. Shan, G. X. Liu, W. J. Lee, G. H. Lee, I. S. Kim, B. C. Shin, Y. C. Kim, "Transparent conductive ZnO thin films on glass substrates deposited by pulsed laser deposition ", J. Cryst. Growth, v 277, n 1-4, p 284-92, 2005.

[1-4]. C. L. Yuan, P. Darmawan, Y. Setiawan, P. S. Lee, "Formation of SiO2 nanocrystals in Lu_2O_3 high-k dielectric by pulsed laser ablation and application in memory device", Nanotechnology, v 17, n 13, p 3175-7, 2006.

[1-5]. F. K. Shan, B. I. Kim, G. X. Liu, Z. F. Liu, J.Y. Sohn, W.J. Lee, B.C. Shin and Y.S. Yu, "Blueshift of near band edge emission in Mg doped ZnO thin films and aging ", J. Appl. Phys. 95, 4772, 2004

[1-6]. K. Matsubara, H. Tampo, H. Shibata, A. Yamada, P. Fons, K. Iwata, S. Niki, "Band-gap modified Al-doped Zn1-xMgxO transparent conducting films deposited by pulsed laser deposition ",Appl. Phys. Lett., v 85, n 8, p 1374-1376, 2004

[1-7]. D.B. Buchholz, R.P.H. Chang, J.H. Song, J.B. Ketterson, "Room-temperature ferromagnetism in Cu-doped ZnO thin films ",Appl. Phys. Lett. v87, n8, p82504-1-3, 2005.

[1-8]. L. A. Bendersky, I. Takeuchi, K. S. Chang, W. Yang, S. Hullavarad, R. D. Vispute, "Microstructural study of epitaxial Zn1-xMgxO composition spreads ", J. Appl. Phys., v 98, n 8, p 083526, 2005.

[1-9]. W. Yang, S. S. Hullavarad, B. Nagaraj, I. Takeuchi, R. P. Sharma, T. Venkatesan, R. D. Vispute, H. Shen, "Compositionally-tuned epitaxial cubic MgxZn1-xO on Si(100) for deep ultraviolet photodetectors ", Appl. Phys. Lett., v 82, n 20, p 3424-3426, 2003

[1-10].N. B. Chen, C. H. Sui, Mat. Sci. Eng. B-solid, "Recent progress in research on MgxZn1-xO alloys",v 126, n 1, p 16-21, 2006

[1-11].C. Ambe, T. Takeuchi, H. Katoh, K. Isomura, T. Satoh, R. Mizumoto, S. Yamaguchi, C. Wetzel, H. Amano, I. Akasaki, Y. Kaneko, N. Yamada, "GaN-based laser diode with focused ion beam-etched mirrors", Mat. Sci. Eng.

B-solid, 59, 1-3, 382-385, 1999

[1-12].H. Yuang, L. X. Zheng, J. B. Li, X. J. Wang, D. P. Xu, Y. T. Wang, and X. W. Hu, P. D. Han, "Cubic-phase GaN light-emitting diodes" ,Appl. Phys. Lett., 74, 17, 2498-2500, 1999

[1-13].H. Sankur, J. T. Cheung, "Highly oriented ZnO films grown by laser evaporation.", J. Vac. Sci. Technol. A, v1, n4, p 1806-1809, 1983.

[1-14].B. M. Ataev, I. K. Kamilov, W. V. Lundin, V. V. Mamedov, A. K. Omaev, and Sh.-M. O. Shakhshaev "High-quality ZnO/GaN/α-Al2O3 heteroepitaxial structures grown by CVD", Tech. Phys. Lett., v. 27 no. 1, p 55- 7, 2001

[1-15].L. J. Meng, M.P. dos Santos, "Direct current reactive magnetron sputtered zinc oxide thin films the effect of the sputtering pressure ", Thin Solid Films, v 250, n 1-2, p 26-32, 1994

[1-16].H. X. Li, J. Y. Wang, H. Liu, H. J. Zhang, X. Li, "Zinc oxide films prepared by sol-gel method" J. Cryst. Growth, v 275, n 1-2, p e943-6, 2005

[1-17].H. W. Liang, Y. M. Lu, D. Z. Shen, Y. C. Liu, B. H. Li, J. Y. Zhang, X. W. Fan, "Growth of zinc oxide thin films on (400) Si by plasma-molecular beam epitaxy ", Proceedings of the SPIE - The International Society for Optical Engineering, v

4913, p 187-90, 2002

[1-18].X. S. Wang, Z. C. Wu, J. F. Webb, Z. G. Liu, "Ferroelectric and dielectric properties of Li-doped ZnO thin films prepared by pulsed laser deposition", Appl. Phys. A-Mater., v 77, n 3-4, p 561-565, 2003

[1-19].H. Z. Wu, J. Liang, Y. F. Lao, N. B. Chen, P. Yu, T. N. Xu, "Characterization of cubic phase MgZnO/Si(100) interfaces ", Appl. Surf. Sci., v 252, n 4, p 1147-52, 2005.

[1-20].A. Ohtomo, M. Kawasaki, T. Koida, K. Masubuchi, H. Koinuma, Y. Sakurai, Y. Yoshida, T. Yasuda, Y. Segawa, "MgxZn1-xO as a II-VI widegap semiconductor alloy", Appl. Phys. Lett., v 72, n 19, p 2466-8, 1998.

[1-21].J. Narayan, A. K. Sharma, A. Kvit, C. Jin, J. F. Muth, O. W. Holland, "Novel cubic ZnxMg1-xO epitaxial heterostructures on Si (100) substrates", Solid State Commun., v 121, n 1, p 9-13, 2001.

[1-22].J. L. Zhao, X. M. Li, J. M. Bian, W. D. Yu, X. D. Gao, "Structural, optical and electrical properties of ZnO films grown by pulsed laser deposition (PLD)", J. Cryst. Growth, v 276, n 3-4, p 507-12, 2005

[1-23].D. C. Look, "Progress in ZnO materials and devices", J. Electron. Mater., Vol. 35, No. 6, p 1299-305 2006

[1-24].S. Kim, B. S. Kang, F. Ren, Y. W. Heo, K. Lp, D. P. Norton, S. J. Pearton, "Contacts to p-type ZnMgO", Appl. Phys. Lett., 84, 1904-1906, 2004.

[1-25].M. Joseph, H. Tabata, H. Saeki, K. Ueda, T. Kawai, "Fabrication of the low-resistive p-type ZnO by codoping method", Physica B, v 302-303, p 140-8, 2001

[1-26].M. Joseph, H. Tabata, T. Kawai, "p-type electrical conduction in ZnO thin films by Ga and N codoping", Jap. J. Appl. Phys., v 38, n 11A, p L1205-7, 1999

[1-27].Z. Vashaei, T. Minegishi, H. Suzuki, M. W. Cho, T. Yao, "A high-resolution electron microscopy study of MgxZn1-xO films grown on MgO/c-sapphire", Phys. Status. Solidi. C, v 3, n 4, p 1042-1045, 2006.

[1-28].S. Choopun, R. D. Vispute, W. Yang, R. P. Sharma, T. Venkatesan, H. Shen, "Realization of band gap above 5.0 eV in metastable cubic-phase MgxZn1-xO alloy films", Appl. Phys. Lett., v 80, n 9, p 1529, 2002.

[1-29].H. P. Zhou, W. Z. Shen, N. B. Chen, H. Z. Wu, "Observation of negative thermo-optical coefficient in cubic MgZnO thin films", Appl. Phys. Lett., v 85, n 17, p 3723-5, 2004.

[1-30].H. Z. Wu, P. Yu, N. B. Chen, T. N. Xu, Y. F. Lao, J. Liang, "Cubic $Mg_xZn_{1-x}O$

films grown on SiO_2 substrates", Opt. Mater., v 28, n 3, p 271-5, 2006.

[2-1]. John L.Vossen and Werner Kern, "Thin Film Processes", 1978.

[2-2]. Robert Eason, "Pulsed laser deposition of thin films: applications-led growth of fundamental materials",2006.

[2-3]. A. Inam, M. S. Hegde, X. D. Wu, T. Venkatesan, P. England, P. F. Miceli, E. W. Chase, C. C. Chang, J. M. Tarascon, J. B. Wachtman, "As-deposited high Tc and Jc superconducting thin films made at low temperatures", Appl. Phys. Lett., v 53, n 10, p 908-10, 1988.

[2-4]. Douglas B. Chrisey, Graham K. Hubler, "Pulsed Laser Deposition of Thin Films", 1994.

[2-5]. http://www.tdcoating.com/td_glossary_terms3.htm

[2-6]. Hari Singh Nalwa, "Deposition and processing of thin films", 2002.

[3-1]. C. Suryanarayana and M. Grant Norton, "X-ray diffraction: A practical approach", 1998.

[3-2]. Stanley L. Flegler, John W. heckman, Jr, Karen L. Klomparens, "Scanning and transmission electron microscopy: an introduction", 1993.

[3-3]. Hatsuo Ishida, “Characterization of composite materials", 1994.

[4-1]. K. Subba Ramaiah, V. Sundara Raja, A. K. Bhatnagar, R. D. Tomlinson, R. D. Pilkington, A. E. Hill,S. J. Chang, Y. K. Su and F. S. Juang, “Optical, structural and electrical properties of tin doped indium oxide thin films prepared by spray-pyrolysis technique”, Semicond. Sci. Tech., 15 676–683, 2000.

[4-2]. K. Matsubara, H. Tampo, H. Shibata, A. Tamada, P. Fons, K. Iwata, and S. Niki, “Band-gap modified Al-doped Zn1-xMgxO transparent conducting films deposited by pulsed laser deposition”, Appl. Phys. Lett. v85, n 8, p 1374-6,2004

[5-1]. S. Yoshida, J. Li, T. Wada, H. Takehara, “High-temperature operation of an AlGaN/GaN HFET on a Si substrate using a thin GaN film”, Phys. Status. Solidi. C, n 7, p 2343-6, 2003.

[5-2]. A. V. Singh, R. M. Mehra, A. Yoshida, A. Wakahara, “Doping mechanism in aluminum doped zinc oxide films”, J. Appl. Phys., v 95, n 7, p 3640-3, 2004.

[5-3]. S. J. Pearton, C. R. Abernathy, G. T. Thaler, R. M. Frazier, D. P. Norton, F. Ren, Y. D. Park, J. M. Zavada, I. A. Buyanova, W. M. Chen, A. F. Hebard, “Wide band gap GaN-based semiconductors for spintronics”, J. Phys-Condens. Mat., v 16, n 7, p R209-45, 2004.

[5-4]. S. J. Pearton, W. H. Heo, M. Ivill, D. P. Norton, T. Steiner, “Dilute magnetic

semiconducting oxides", Semicond. Sci. Tech., v19, n 10, R59-R74, 2004.

[5-5]. A. Ohtomo, R. Shiroki, I. Ohkubo, H. Koinuma, and M. Kawasaki, "Thermal stability of supersaturated MgxZn1-xO alloy films and MgxZn1-xO/ZnO heterointerfaces", Appl. Phys. Lett. v75, n26, p4088-90, 1999.

[5-6]. T. Gruber, C. Kirchner, R. Kling, F. Reuss, and A. Waag, "ZnMgO epilayers and ZnO-ZnMgO quantum wells for optoelectronic applications in the blue and UV spectral region", Appl. Phys. Lett. v84, n26, p 5359-61, 2004.

[5-7]. K. Ogata, K. Koike, T. Tanite, T. Komuro, F. Yan, S. Sasa, M. Inoue, and M. Yano, "ZnO and ZnMgO growth on α-plane sapphire by molecular beam epitaxy", J. Cryst. Growth, v 251, n 1-4, p 623-27, 2003.

[5-8]. S. Krishnamoorthy, A. A. Iliadis, A. Inumpudi, S. Choopun, R. D. Vispute, and T. Venkatesan, "Observation of resonant tunneling action in $ZnO/Zn_{0.8}Mg_{0.2}O$ devices", Solid State Electron., v 46, n 10, 1633-7, 2002.

[5-9]. D. J. Cohen, K. C. Ruthe, and S. A. Barnett, "Transparent conducting $Zn_{1-x}Mg_xO$:(Al,In) thin films", J. Appl. Phys. v 96, n 1, p 459-67, 2004.

[5-10].A. Ohtomo, M. Kawasaki, I. Ohkubo, H. Koinuma, T. Yasuda, and Y. Segawa, "Structure and optical properties of ZnO/Mg0.2Zn0.8O superlattices", Appl. Phys. Lett. v 75, n 7, p 980-982, 1999.

[5-11].H. D. Sun, T. Makino, Y. Segawa, M. Kawasaki, A. Ohtomo, K. Tamura, and H. Koinuma, "Enhancement of exciton binding energies in ZnO/ZnMgO multiquantum wells", J. Appl. Phys., v 91, n 4, 1993-7, 2002.

[5-12].T. Makino, Y. Segawa, M. Kawasaki, A. Ohtomo, R. Shiroki, K. Tamura, T. Yasuda, and H. Koinuma, "Band gap engineering based on MgxZn1-xO and CdyZn1-yO ternary alloy films", Appl. Phys. Lett. v 78, n 9, 1237-9, 2001.

[5-13].T. Makino, C. H. Chia, N. T. Tuan, Y. Segawa, M. Kawasaki, A. Ohtomo, K. Tamura, and H. Koinuma, "Radiative and nonradiative recombination processes in lattice-matched (Cd,Zn)O/(Mg,Zn)O multiquantum wells", Appl. Phys. Lett. v 77, n 11, p 1632-4, 2000.

[5-14].O. Vigil, L. Vaillant, F. Cruz, G. Santana, A. Morales-Acevedo, and G. Contreras-Puente, "Spray pyrolysis deposition of cadmium-zinc oxide thin films", Thin Solid Films, v 361–362, p 53-5, 2000.

[5-15].Y. S. Choi, C. C. Lee, and S. M. Cho, "Transparent conducting ZnxCd1-xO thin films prepared by the sol-gel process", Thin Solid Films, v 289, n 1-2, 153-8, 1996.

[5-16].S. M. Sze, "Physics of Semiconductor devices 2nd edition", 1981.

[5-17].Robert F. Pierret, “Semiconductor Devices fundamentals”,1996.

[5-18].U. S. Joshi, Y. Matsumoto, K. Itaka, M. Sumiya, H. Koinuma, “Combinatorial synthesis of Li-doped NiO thin films and their transparent conducting properties“, Appl. Surf. Sci., v 252, n 7, p 2524-8, 2006.

[5-19].P. Puspharajah, S. Radhakrishna, A. K. Arof, “Transparent conducting lithium-doped nickel oxide thin films by spray pyrolysis technique”, J. Mater. Sci., v 32, n 11, p 3001-6, 1997.

[5-20].Bart Van Zeghbroeck “Principles of semiconductor devices”,2004

[5-21].jasprit singh, “Semiconductor devices basic principles”, 2001.

[6-1]. M. Wittmer, B. Studer, H. Melchior, “Electrical characteristics of TiN contacts to N-silicon”, J. of Appl. Phys., v 52, n 9, p 5722-6, 1981.

[6-2]. M.Y. Al-Jaroudi, H.T.G. Hentzel, S.E. Hornstrom, A. Bengston, “Titanium nitride deposition on hardened high speed steel by reactive magnetron sputtering”, Thin Solid Films, v190, n2, p265-77, 1989.

[6-3]. S. Kadlec, J. Musil, J. Vyskocil, “Growth and properties of hard coatings prepared by physical vapor deposition methods”, Surf. Coat. Tech., v54–55, n1-3, p287-96, 1992.

[6-4]. U. Beck, G. Reiners, I. Urban, K. Witt, "Evaluation of optical properties of decorative coatings by spectroscopic ellipsometry", Thin Solid Films, v220, n1-2, p234-40, 1992.

[6-5]. H. Joswig, W. Palmer, "Stoichiometry effects in TiN diffusion barriers", Thin Solid Films, v221, n1-2, p228-32, 1992.

[6-6]. J. E. Sundgren, "Structure and properties of TiN coatings", Thin Solid Films, v128, n1-2, p21-44, 1985.

[6-7]. R.C. Glass, L.M. Spellman, S. Tanaka, R. F. Davis, "Chemical and structural analyses of the titanium nitride/alpha (6H)-silicon carbide interface", J. Vac. Sci. Technol. A, v10, n4, p1625-30, 1992.

[6-8]. G. Gagnon, J.F. Currie, C. Beique, J.L. Brebner, S.G. Gujrathi, L. Onllet, "Characterization of reactively evaporated TiN layers for diffusion barrier applications", J. Appl. Phys., v75, n3, p1565-70, 1994.

[6-9]. E.O. Travis, R.W. Fiordalice, "Manufacturing aspects of low pressure chemical-vapor-deposited TiN barrier layers", Thin Solid Films, v236, n1-2, p325-9, 1993.